Role of adipose mTORC2 in mature adipocytes and whole-body energy homeostasis

Inauguraldissertation

zur
Erlangung der Würde eines Doktors der Philosophie
vorgelegt der Philosophisch-Naturwissenschaftlichen Fakultät
der Universität Basel

von

Irina Céline Frei

Basel, 2023

Genehmigt von der Philosophisch-Naturwissenschaftlichen Fakultät
auf Antrag von Prof. Dr. Michael N. Hall und Prof. Dr. Bernard Thorens

Basel, den 26.04.2022

Prof. Dr. Marcel Mayor

Dekan

Table of contents

I. Summary **5**

II. Abbreviations **7**

1. Introduction **11**

1.1 The mTORC2 signaling pathway **11**

1.1.1 mTOR signaling 11

1.1.2. mTORC2 composition and structure 11

1.1.3. Subcellular localization of mTORC2 12

1.1.4. Upstream regulation of mTORC2 13

1.1.5. Downstream signaling of mTORC2 13

1.2. mTORC2 and its role in whole-body energy homeostasis **15**

1.2.1 mTORC2 in obesity and type II diabetes 15

1.2.2 mTORC2 in the central nervous system 15

1.2.3 mTORC2 in muscle 16

1.2.4. mTORC2 in liver 17

1.2.5. mTORC2 in adipose tissue 22

1.3. Recent advances using imaging techniques applied to whole-adipose tissue **29**

2. Aims of the thesis **33**

3. Results **37**

3.1 Manuscript 1: Adipose mTORC2 is essential for arborization of sensory neurons in white adipose tissue **37**

3.1.1. Abstract 38

3.1.2. Introduction 38

3.1.3. Results 40

3.1.4. Discussion 44

3.1.5. Materials and Methods 46

3.1.6. Figures 55
3.1.7. Supplementary Figures 61
3.2 Manuscript 2: Adipose and hepatic mTORC2 promote energy storage and maintains glucose homeostasis 69
3.2.1. Abstract 70
3.2.2. Introduction 70
3.2.3. Results 71
3.2.4. Discussion 75
3.2.5. Materials and Methods 76
3.2.6. Figures 80
3.2.7. Supplementary Figures 86
3.3 Supplementary Data 88
4. Discussion 95
4.1 Role of mTORC2 in adipocytes 95
4.2 Role of adipose mTORC2 in whole-body energy homeostasis 96
4.3. Role of adipose mTORC2 in neuronal innervation 98
5. Acknowledgements 103
6. References 107
7. Appendix 120

I. Summary

Mammalian target of rapamycin complex 2 (mTORC2) is a protein kinase complex that optimizes anabolic and catabolic cellular processes in response to environmental cues to maintain energy homeostasis. mTORC2 is ubiquitously expressed, and its dysregulation is associated with metabolic disorders such as obesity and type II diabetes. In white adipose tissue (WAT), mTORC2 signaling promotes various insulin-dependent processes including glucose uptake and *de novo* lipogenesis (DNL). Loss of adipose mTORC2 not only impairs adipocyte metabolism, but also disrupts whole-body energy homeostasis.

In order to better understand the role of adipose mTORC2 in whole-body energy homeostasis, we generated tamoxifen-inducible adipose-specific RICTOR knockout (iAdRiKO) mice. We found that ablation of RICTOR, an essential component of mTORC2, in mature adipocytes causes hyperinsulinemia, systemic insulin resistance and aberrant liver AKT signaling. Since loss of adipose mTORC2 rapidly alters phosphorylation of proteins associated with the plasma membrane and involved in synapse formation, we hypothesized that adipose mTORC2 regulates inter-organ communication via the peripheral nervous system. We established a whole-adipose tissue clearing and imaging method to visualize the sensory and sympathetic neuronal network in WAT. We discovered that adipose mTORC2 is essential for arborization of sensory neurons, but not sympathetic neurons. Further investigation could not confirm a role for sensory neurons in the regulation of whole-body energy homeostasis, although a more suitable mouse model is required to definitely confirm these observations.

We also demonstrate that loss of adipose mTORC2 impairs the capacity of WAT to import and store excess energy. As a result, mice lacking adipose mTORC2 develop mild lipodystrophy and accumulate triglycerides (TGs) in the liver due to increased DNL. Blocking hepatic DNL and TG accumulation in the absence of adipose mTORC2 signaling has a detrimental effect on whole-body energy homeostasis, resulting in severe insulin resistance and glucose intolerance. We conclude that mTORC2 ablation in adipocytes impairs energy storage in WAT and the subsequent increase in hepatic DNL is a physiological response to compensate for impaired WAT function.

Although we cannot exclude that mTORC2 regulates whole-body energy homeostasis via an unknown adipokine or sensory activity, our data suggests that adipose mTORC2 contributes to whole-body energy homeostasis by promoting the core function of WAT, namely the storage of excess energy.

II. Abbreviations

2DG	2- deoxyglucose
2DGP	2-deoxyglucose-6-phosphate
ACC	acetyl-coenzyme A carboxylase
Acetyl-CoA	acetyl-coenzyme A
ACLY	ATP-Citrate Lyase
Adipo-AKT KO	adipose-specific AKT1 and AKT2 knockout
AKT	protein kinase B
ATGL	adipose tissue triglyceride lipase
BAT	brown adipose tissue
CGRP	calcitonin gene-related peptide
cAMP	cyclic adenosine monophosphate
ChREBP	carbohydrate response element binding protein
CNS	central nervous system
DNL	*de novo* lipogenesis
dRiKO	double *Rictor* knockout mice
ELISA	enzyme-linked immunosorbent assay
ER	endoplasmic reticulum
eWAT	epididymal white adipose tissue
FASN	fatty acid synthase
FFAs	free fatty acids
FOXO1	O-subfamily of the FOX protein 1
GAP43	growth-associated protein 43
GIIS	glucose-induced insulin secretion
GLUT2	glucose transporter 2
GLUT4	glucose transporter 4
GSK3	glycogen synthase kinase 3
GTT	glucose tolerance test
HDL	high density lipoprotein
HK2	hexokinase 2
HM	hydrophobic motif
HSL	hormone sensitive lipase
iAdRiKO	inducible adipose-specific RICTOR knockout

IGF-1	insulin-like growth factor 1
ITT	insulin tolerance test
iWAT	inguinal white adipose tissue
LDL	low density lipoprotein
LiRiKO	liver-specific rictor knockout
MAM	mitochondria-associated ER membrane
MAG	monoglyceride lipase
mLST8	mammalian lethal with sec-13 protein
mSIN1	mammalian stress-activated map kinase-interacting protein 1
mTOR	mammalian target of rapamycin
mTORC1	mammalian target of rapamycin complex 1
mTORC2	mammalian target of rapamycin complex 2
NAFLD	Non-alcoholic fatty liver disease
NE	norepinephrine
PCA	principal component analysis
PDK1	phosphoinositide-dependent kinase 1
PH	pleckstrin homology
PI3K	phosphatidylinositol 3-kinase
PI(3,4,5)P_3	phosphatidylinositol-3,4,5-triphosphate
PI(4,5)P_2	phosphatidylinositol-4,5-biphosphate
PKA	protein kinase A
PKC	protein kinase C
POMC	pro-opiomelanocortin
PRDM16	PRD1-BF-1-RIZ1 homologous domain-containing protein-16
RICTOR	rapamycin insensitive companion of mTOR
SGK1	serum- and glucocorticoid-induced protein kinase 1
SNS	sympathetic nervous system
SREBP 1c	sterol regulatory element-binding protein 1c
TCA	tricarboxylic acid
TGs	triglycerides
TH	tyrosine hydroxylase or tyrosine-3 monooxygenase
TM	turn motif
TOR	target of rapamycin
UCP1	uncoupling protein 1
VLDLs	very low-density lipoproteins
WAT	white adipose tissue

Chapter 1: Introduction

1. Introduction

1.1 The mTORC2 signaling pathway

1.1.1 mTOR signaling

Mammalian target of rapamycin (mTOR) signaling promotes cell growth and regulates metabolism in response to environmental cues. mTOR signaling is mediated by the mammalian ortholog of the conserved serine/threonine kinase target of rapamycin (TOR) which was first discovered in yeast as the target of the macrolide and immunosuppressant drug rapamycin (Heitman, Movva, & Hall, 1991; Kunz et al., 1993). Since then, orthologs of TOR have been found in all eukaryotes examined except for some parasites (van Dam, Zwartkruis, Bos, & Snel, 2011). In mammals, mTOR exists in two distinct complexes, mTOR complex 1 (mTORC1) and mTORC2. Both complexes are essential and integrate the cellular and environmental energy status to optimize anabolic and catabolic processes. TORC1 can be pharmacologically inhibited by rapamycin, however, TORC2 is rapamycin resistant. The lack of an TORC2-specific inhibitor is a major reason why the role and regulation of TORC2 is much less understood than TORC1 (Gaubitz, Prouteau, Kusmider, & Loewith, 2016). Nonetheless, it is well established that mTORC2 is regulated by growth factors including insulin and its activity is dysregulated in many metabolic disorders such as obesity and type II diabetes.

1.1.2. mTORC2 composition and structure

mTORC2 is a serine/threonine kinase multiprotein complex that is composed of four core components comprising the mTOR kinase, rapamycin-insensitive companion of mTOR (RICTOR), mammalian homolog of protein lethal with SEC13 protein 8 (mLST8) and mammalian stress-activated map kinase-interacting protein 1 (mSIN1) (Jacinto et al., 2004; Loewith et al., 2002; Sarbassov et al., 2004). All four core components are essential for mTORC2 assembly and activity (**Figure 1**). The active form of mTORC2 forms a rhomboid-shaped dimer with the two mTOR subunits at the core (Scaiola et al., 2020; Stuttfeld et al., 2018). The catalytic site of mTOR faces outward and is flanked on one side by mLST8 and on the other side by RICTOR. RICTOR also blocks the rapamycin binding site of mTOR thereby accounting for insensitivity of mTORC2 to rapamycin. mSIN1 stabilizes this conformation by

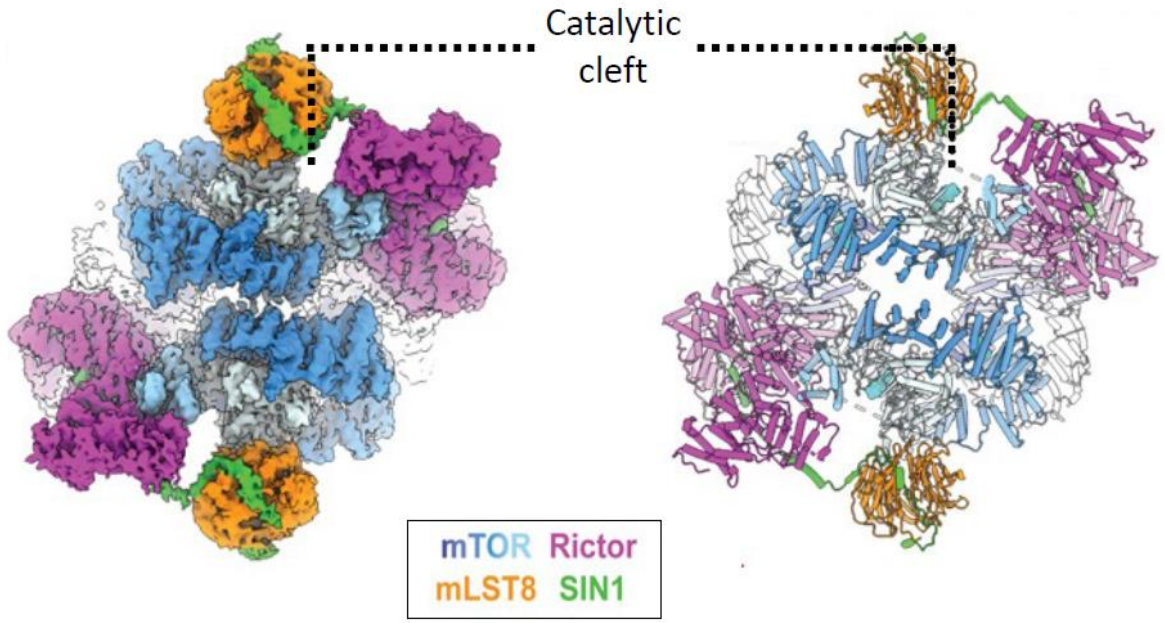

Figure 1. mTORC2 structure
Density of the overall cryo-EM reconstruction (left) and a cartoon representation (right). Complex subunits (mTOR, RICTOR, SIN1 and mLST8) are colored as indicated. Modified from (Scaiola et al., 2020).

connecting RICTOR to mLST8. In addition, mSIN1 is predicted to mediate substrate recruitment and its isoforms determine distinct forms of mTORC2 (Frias et al., 2006). At least two of five mSIN1 isoforms have a pleckstrin homology (PH) domain which binds phosphoinositides and potentially mediates plasma membrane localization of mTORC2.

1.1.3. Subcellular localization of mTORC2

mTORC2 has been found in several different subcellular compartments indicating the existence of distinct pools of mTORC2 (Betz & Hall, 2013). mTORC2 localizes to the cytoplasm, nucleus, endosomes, Golgi, ribosome, lysosome, endoplasmic reticulum (ER), mitochondria, mitochondria-associated ER membrane (MAM), and the plasma membrane. However, the function and physiological relevance of these different mTORC2 pools are not fully understood. Using a reporter construct, mTORC2 kinase activity was detected in the plasma membrane, mitochondria and a subpopulation of endosomal vesicles (Betz & Hall, 2013; Fu & Hall, 2020; Knudsen et al., 2020). These observations are in agreement with the localization of many, if not all, known downstream substrates of mTORC2 (Keenan & Kelleher, 1998; Manning & Toker, 2017). Whether mTORC2 translocates to these locations upon activation or whether the different mTORC2 pools remain separate and are regulated independently is unknown. However, localization of mTORC2 is also determined by the

incorporated mSIN1 isoform. Only mSIN1 isoforms bearing a PH domain can bind phosphoinositides in the plasma membrane. Interestingly, only the sub-type of mTORC2 containing a mSIN1 isoform competent in phosphoinositide-binding is activated by insulin, supporting the notion that different mTORC2 forms are differently localized and regulated (Ebner, Sinkovics, Szczygiel, Ribeiro, & Yudushkin, 2017; P. Liu et al., 2015).

1.1.4. Upstream regulation of mTORC2

It is well established that growth factors including insulin and insulin-like growth factor 1 (IGF-1) stimulate mTORC2 activity via the phosphoinositide 3-kinase (PI3K) pathway (**Figure 2**). Some aspects of the exact mechanism however remain controversial. For example, whether all mTORC2 pools are sensitive to insulin and, if so, how they are activated. PI3K is a lipid kinase that phosphorylates the phospholipid phosphatidylinositol-4,5-bisphosphate ($PI(4,5)P_2$) at the plasma membrane to produce phosphatidylinositol 3,4,5-triphosphate ($PI(3,4,5)P_3$). $PI(3,4,5)P_3$ recruits several kinases via their PH domain to the plasma membrane including the mTORC2 substrate protein kinase B (AKT) (Manning & Toker, 2017). It has been reported that $PI(3,4,5)P_3$ also directly activates and recruits mTORC2 via the PH domain of mSIN1 (P. Liu et al., 2015). An alternative model proposes that mTORC2 binds not only $PI(3,4,5)P_3$, but different species of phosphoinositides and thus is constantly localized to the plasma membrane (Knudsen et al., 2020; Schroder et al., 2007). In this model, mTORC2 activity is mediated by the $PI(3,4,5)P_3$-dependent recruitment of its substrate to the plasma membrane However, both models concern the membrane-bound pool of mTORC2. How other mTORC2 pools are regulated is poorly understood. Growth factors also appear to promote recruitment and activity of mTORC2 to MAM and ribosomes (Betz et al., 2013; Zinzalla, Stracka, Oppliger, & Hall, 2011). In addition, recent reports suggest the involvement of small GTPases and some metabolites such as acetyl-CoA in the activation of mTORC2 (Castellano & Downward, 2011; Kovalski et al., 2019; Saci, Cantley, & Carpenter, 2011).

1.1.5. Downstream signaling of mTORC2

Most of the known mTORC2 downstream targets belong to the AGC kinase family and include AKT, protein kinase C (PKC), and serum- and glucocorticoid-induced kinases 1 (SGK1) (**Figure 2**). The best characterized readout of mTORC2 is the phosphorylation site S473 in the hydrophobic motif (HM) of AKT. AKT is activated by two growth factor-

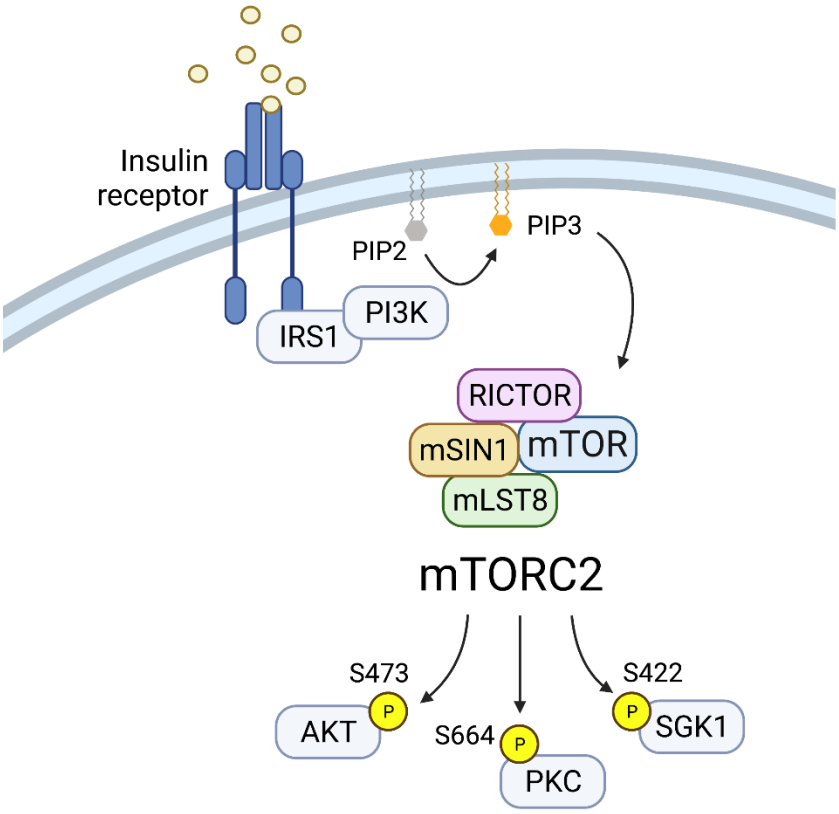

Figure 2. Insulin-stimulated mTORC2 signaling
Canonical mTORC2 signaling upon insulin stimulation. SGK1, AKT, and PKC phosphorylation sites are represented by the hydrophobic motif of isoforms SGK1, AKT1 and PKCδ.

dependent kinases, phosphoinositide-dependent kinase 1 (PDK1) and mTORC2. PDK1 phosphorylates AKT at the phosphorylation site T308 in the so-called T-loop (or activation loop) which is required for AKT activity. Additional phosphorylation at the mTORC2-dependent phosphorylation site S473 promotes full AKT activation which is required to phosphorylate some, if not all, AKT substrates (Sarbassov, Guertin, Ali, & Sabatini, 2005). Since not all AKT substrates require fully active AKT to become phosphorylated, not all AKT targets are mTORC2 dependent. As a consequence, downstream signaling pathways of AKT and mTORC2 do not fully overlap. However, in most tissues and cell types, mTORC2 promotes *de novo* lipogenesis, glucose uptake, and glycolysis in an AKT-dependent manner. In addition, mTORC2 co-translationally phosphorylates AKT at Ser450 in the turn motif (TM) (Facchinetti et al., 2008; Ikenoue, Inoki, Yang, Zhou, & Guan, 2008; Oh et al., 2010). This phosphorylation is constitutive and required for AKT stability. Similar to AKT, PKCs are also phosphorylated at their HM and TM by mTORC2 (Facchinetti et al., 2008; Ikenoue et al., 2008; Sarbassov et al., 2004). The PKC kinases are classified into different groups: the conventional c-PKCs (α, β and γ), the novel n-PKCs (δ, ε, η, θ, and μ), and the atypical a-PKCs (ι and ζ). To date, only PKCβII, PKCδ and PKCζ are experimentally verified as mTORC2 substrates while strong evidence for PKCα, PKCγ and PKCε as mTORC2

substrates exists (Baffi et al., 2021; Gan et al., 2012; Ikenoue et al., 2008). As with AKT, mTORC2-dependent TM phosphorylation is required for PKC stability. mTORC2-dependent phosphorylation of the HM increases PKC activity and thereby promotes cytoskeletal rearrangement. Another well-established substrate of mTORC2 is SGK1, a serine/threonine kinase involved in stress response and cell survival. mTORC2-dependent phosphorylation of Ser422 in the HM of SGK1 increases kinase activity (Garcia-Martinez & Alessi, 2008). However, the role of mTORC2 on SGK1-dependent substrates such as ion channels, carriers and transporters is not well established. Other non-AGC kinase mTORC2 substrates have been reported, however, more studies are required to characterize these substrates and their function (Battaglioni, Benjamin, Wälchli, Maier, & Hall, 2022).

1.2. mTORC2 and its role in whole-body energy homeostasis

1.2.1 mTORC2 in obesity and type II diabetes

mTORC2 signaling is involved in optimizing anabolic and catabolic cellular processes in response to the environmental energy status. Thus, loss of mTORC2 signaling has a profound effect on metabolism at both cellular and whole-body level. mTORC2 is expressed in all metabolic tissues and organs including the central nervous system, muscle, the liver and adipose tissue. Since all these tissues execute different functions and express different isoforms of core components and downstream substrates, the effect of reduced mTORC2 on both cellular and whole-body metabolism varies. A large body of evidence from genetically modified mouse models carrying tissue-specific deletions of *rictor* have confirmed mTORC2 as an important regulator of whole-body energy homeostasis. In addition, dysregulation of mTORC2 has been reported in patients with a variety of metabolic disorders including obesity and type II diabetes. For example, we have previously shown that the mTORC2-dependent substrate AKT-pS473 is reduced in white adipose tissue of obese and diabetic patients compared to healthy individuals (Shimobayashi et al., 2018).

1.2.2 mTORC2 in the central nervous system

The central nervous system (CNS) is crucial to maintain whole-body energy homeostasis. Peripheral signals such as hormones and neuronal stimuli from sensory neurons are integrated in specific brain regions to adapt energy expenditure and feeding behavior. A recent publication has reported that mTORC2 activity increases with age in specific brain regions

including the thalamus, cortex, and hypothalamus, a region that integrates peripheral signals to coordinate whole-body energy homeostasis (Chellappa et al., 2019). Neuronal mTORC2 is crucial for neurite outgrowth, presynaptic signaling and synaptic vesicle release (McCabe et al., 2020; Urbanska, Gozdz, Swiech, & Jaworski, 2012). Both neurite outgrowth and presynaptic signaling are regulated by the mTORC2 substrate PKC and its isoforms (Angliker & Ruegg, 2013; McCabe et al., 2020). An *in vivo* model of mice lacking RICTOR in neurons confirmed the importance of mTORC2 in neuronal physiology and activity (Thomanetz et al., 2013). Further *in vivo* studies investigated the role of mTORC2 in neuronal sub-populations of the hypothalamus. Mice lacking hypothalamic mTORC2 become more susceptible to diet-induced obesity (Chellappa et al., 2019). In agreement with this observation, mTORC2 activity in inhibitory pro-opiomelanocortin (POMC)-positive hypothalamic neurons is crucial to reduce food intake and prevent obesity and glucose intolerance (Kocalis et al., 2014).

1.2.3 mTORC2 in muscle

Skeletal muscle is the principal site of insulin-stimulated glucose uptake and thus crucial for whole-body energy homeostasis (DeFronzo, Ferrannini, Sato, Felig, & Wahren, 1981). Insulin-mediated glucose uptake is promoted by the AKT-dependent translocation of glucose transporter 4 (GLUT4) from internal vesicles to the plasma membrane. Translocation of GLUT4 and thus glucose uptake is also induced by exercise to account for the increased energy demand by a yet unknown pathway. Imported glucose is then either metabolized to produce energy or converted to glycogen, a multibranched polysaccharide of glucose, for further storage. Loss of mTORC2 in muscle cells impairs both insulin- and exercise-stimulated glucose uptake and GLUT4 translocation (Kleinert et al., 2017; Kumar et al., 2008). While it is well established that mTORC2-dependent AKT-pS473 phosphorylation mediates insulin-stimulated glucose uptake, the molecular pathway(s) involved in exercise-induced mTORC2 activity and its role in glucose uptake are less understood (Kleinert et al., 2017; Kumar et al., 2008). Loss of muscle mTORC2 also increases basal glycogen synthesis and the amount of triglycerides in muscle cells (Kleinert et al., 2016; Kumar et al., 2008). Taken together, these results indicate that mTORC2 promotes glucose utilization by increasing its rate limiting step while, at the same time, inhibiting energy deposition in muscle. As a consequence, mice lacking mTORC2 in the muscle become glucose intolerant probably due to reduced energy expenditure (Kumar et al., 2008). However, another study reported that mTORC2 has no impact on muscle function or metabolism (Bentzinger et al., 2008).

1.2.4. mTORC2 in liver

The liver is a central metabolic organ involved in maintaining glucose and lipid homeostasis as well as in compound detoxification. The liver adapts its function to the metabolic state of the body in response to hormones. Insulin promotes anabolic processes and energy storage in the form of carbohydrates and triglycerides while epinephrine and glucagon stimulate catabolic processes and the release of energy in the form of glucose.

Role of the liver in glucose homeostasis

Under fasting conditions, the liver provides glucose as fuel for other tissues, especially the brain. The liver generates glucose by breaking down stored glycogen in a process called glycogenolysis (Han, Kang, Kim, Choi, & Koo, 2016; Nordlie, Foster, & Lange, 1999). However, hepatic glycogen storage capacity is limited. To ensure a sustained flow of glucose to the body, the liver is able to synthesize glucose *de novo* in a process called gluconeogenesis (Han et al., 2016). Gluconeogenesis uses a variety of substrates including lactate and glycerol as the starting point to generate glucose (Pilkis & Claus, 1991; Pilkis, el-Maghrabi, & Claus, 1988). Despite the importance of gluconeogenesis during a period of prolonged starvation, excessive glucose production due to dysregulated gluconeogenesis even during the fed state is the main cause for hyperglycemia in diabetic patients (Magnusson, Rothman, Katz, Shulman, & Shulman, 1992). Thus, the regulation of hepatic gluconeogenesis has been extensively studied. Animal models and cell culture experiments have shown that glucagon and epinephrine promote gluconeogenesis while the insulin/AKT signaling pathway suppresses gluconeogenesis (Han et al., 2016; Hatting, Tavares, Sharabi, Rines, & Puigserver, 2018). Under nutrient rich conditions, the liver functions as an energy storage organ. The liver takes up excessive glucose via the insulin-independent low affinity glucose transporter 2 (GLUT2) thereby lowering blood glucose levels (Mueckler & Thorens, 2013). Imported glucose is used as a substrate for glycolysis and can be fully oxidized via the tricarboxylic acid (TCA) cycle and oxidative phosphorylation to generate energy. Excessive glucose that is not required for immediate energy supply is converted to glycogen by glycogenesis to replenish the glycogen stores. Glycogenesis is promoted by the insulin/AKT signaling pathway while glucagon and epinephrine counteract glycogen production by increasing cyclic adenosine monophosphate (cAMP) levels. In addition to glycogenesis, acetyl-coenzyme A (acetyl-CoA), a breakdown product of glucose, can be converted to free fatty acids (FFA) and stored in the form of triglycerides.

Role of the liver in lipid metabolism

The liver is not only crucial for glucose homeostasis, but also involved in lipid metabolism. The liver has the capacity to convert carbohydrates into lipids by synthesising FFA from acetyl-CoA by DNL (Sanders & Griffin, 2016). Briefly, DNL begins with citrate, an intermediate of the TCA cycle. Since the TCA cycle takes place in the mitochondria, citrate has to be first exported to the cytosol where it is converted by ATP-Citrate Lyase (ACLY) to cytosolic acetyl-CoA. In the cytosol, acetyl-CoA carboxylase (ACC) converts cytosolic acetyl-CoA to malonyl-CoA. The malonyl-CoA unit is then transferred to the acyl carrier protein domain of fatty acid synthase (FASN). FASN is a multienzyme protein that harbours domains with different catalytic activities including malonyl/acetyl transferase, ketoreductase, dehydratase and enoyl reductase. Sequential activity of these enzymatic subunits generates a saturated acyl chain elongation by two carbon groups through the condensation of acetyl-CoA and malonyl-CoA (**Figure 3**). Through repeated condensation steps, FASN elongates the acyl chain until the 16-carbon stage and releases palmitate (16-carbon saturated fatty acid) via the activity of its thioesterase domain. Palmitate is the major product of DNL and can be converted and/or further elongated to a variety of FFA species (D. W. Foster & Bloom, 1963; Hellerstein et al., 1991; E. J. Murphy, 2006). Once synthesized, the various FFA can be further converted into different classes of lipids including TGs, phospholipids and sphingolipids which are essential for the physiology of the cell. Another important fate of FFA produced by hepatic DNL is its incorporation in very low-density lipoproteins (VLDLs) in the form of various lipids. VLDLs are secreted and transported to distal tissues such as adipose tissue where the lipids are hydrolysed to FFA and then imported for further use.

Increased hepatic DNL is common in patients with non-alcoholic fatty liver disease (NAFLD), hepatic insulin resistance and type II diabetes (Ameer, Scandiuzzi, Hasnain, Kalbacher, & Zaidi, 2014; Donnelly et al., 2005). Thus, the regulation of DNL has been extensively studied. DNL depends on allosteric regulation of ACC and on the transcriptional regulation of two transcription factors, the sterol regulatory element binding protein 1c (SREBP1c) and the carbohydrate response element binding protein (ChREBP) (Sanders & Griffin, 2016). SREBP1c is regulated by insulin and the subsequent activation of both the PI3K and AKT pathways. Insulin/AKT signaling promotes nascent SREBP1c phosphorylation and thereby accumulation of the mature active form of SREBP1c in the nucleus (Hegarty et al., 2005). Nuclear SREBP1c then promotes the transcription of several

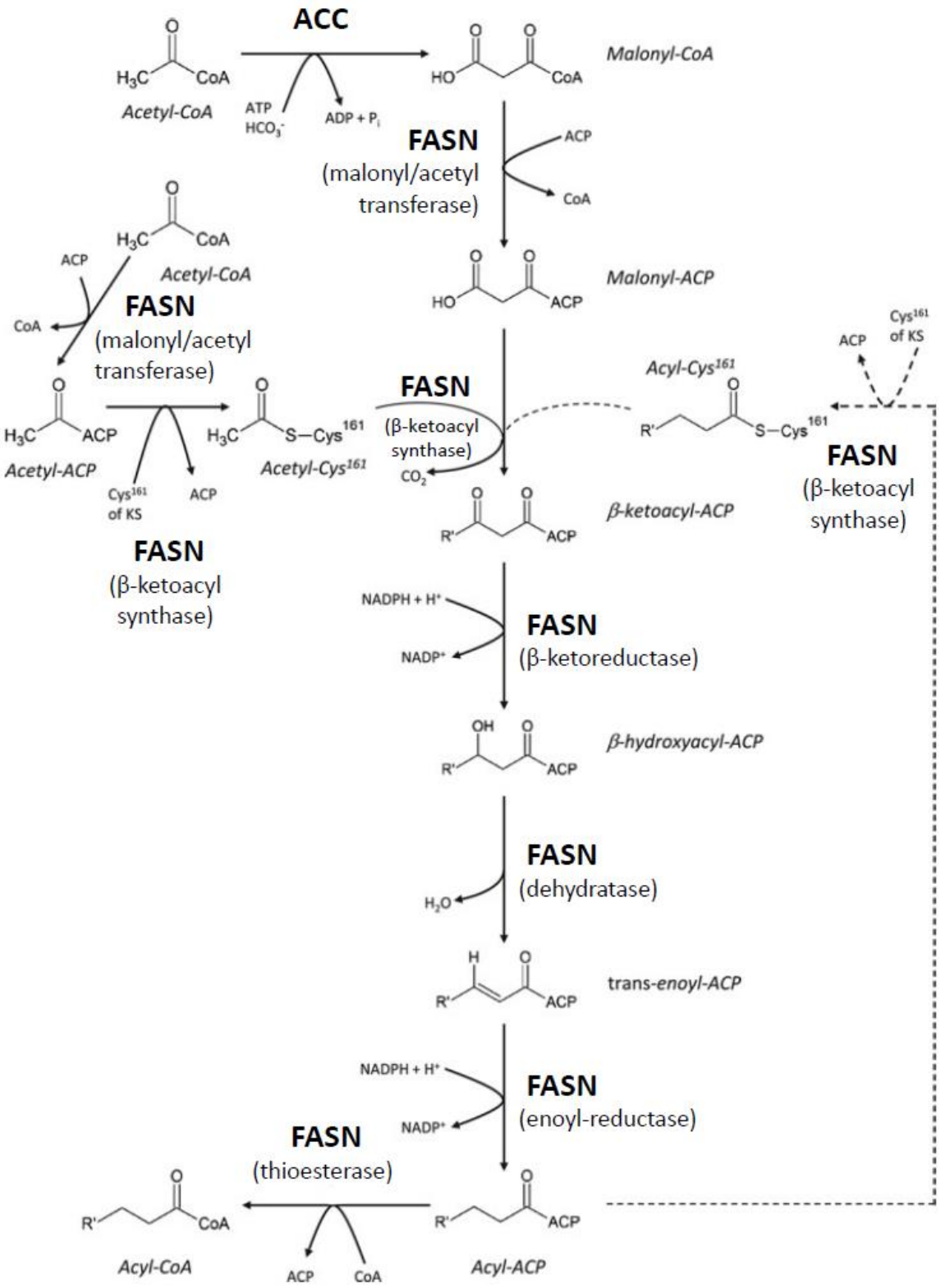

Figure 3. De novo lipogenesis

De novo lipogenic pathway showing the various steps catalyzed by ACC and FASN. Modified from (Sanders & Griffin, 2016).

genes involved in DNL including ACLY, ACC and FASN. In contrast to SREBP1c, ChREBP is activated by an increased glucose flux into hepatocytes. Several metabolites generated by glycolysis are believed to regulate ChREBP activity, although the exact mechanism is unknown. ChREBP translocation to the nucleus promotes the transcription of lipogenic genes including ACC and FASN.

Hepatocytes not only newly synthesize FFA via DNL, but also import excess circulating FFAs via the FFA translocase CD36 (Hajri & Abumrad, 2002; Rada, Gonzalez-Rodriguez, Garcia-Monzon, & Valverde, 2020). CD36 is a multifunctional glycoprotein with several known ligands such as long chain FFA and multiple lipoproteins including high density lipoprotein (HDL), low density lipoprotein (LDL), and VLDL (Pepino, Kuda, Samovski, & Abumrad, 2014). Under physiological conditions, the expression of CD36 in hepatocytes is low. However, high lipid and FFA content in the blood promotes hepatic CD36 expression indicating that the liver acts as a sink for excess lipids and FFA. Imported FFA are esterified to TGs and stored in hepatocytes leading to an accumulation of hepatic TG. Indeed, around 60% of TGs stored in the liver originate from FFA import while hepatic DNL contributes 26% and dietary FFAs and TGs account for 15% of the stored TGs (Donnelly et al., 2005). Since hepatocytes are not specialized to store an excessive amount of TGs, hepatic TG accumulation leads to NAFLD. The global prevalence of NAFLD is increasing and is currently estimated at around 25% (Younossi et al., 2016). Thus, distorted lipid homeostasis and hepatic lipid metabolism are a major health concern.

Role of hepatic mTORC2

As mTORC2 is an integral part of the insulin/AKT signaling pathway, loss of mTORC2 in the liver has major consequences for hepatic glucose and lipid metabolism (**Figure 4**). Liver-specific *rictor* knockout (LiRiKO) mice display impaired hepatic AKT signaling indicated by a reduction in mTORC2-dependent AKT-pS473 phosphorylation (Hagiwara et al., 2012). In addition, loss of mTORC2 activity in the liver causes partial hepatic insulin resistance. In the absence of mTORC2, insulin fails to phosphorylate AKT-dependent substrates including Forkhead Box O1 (FOXO1)-pT24 and glycogen synthase kinase 3 (GSK3)α/β-pS9/21, while AKT-pT308 phosphorylation and mTORC1 activation remain intact. FOXO1 is a transcription factor that induces the expression of gluconeogenic genes. Insulin-stimulated FOXO1-pT24 prevents FOXO1 localization to the nucleus and thus FOXO-dependent

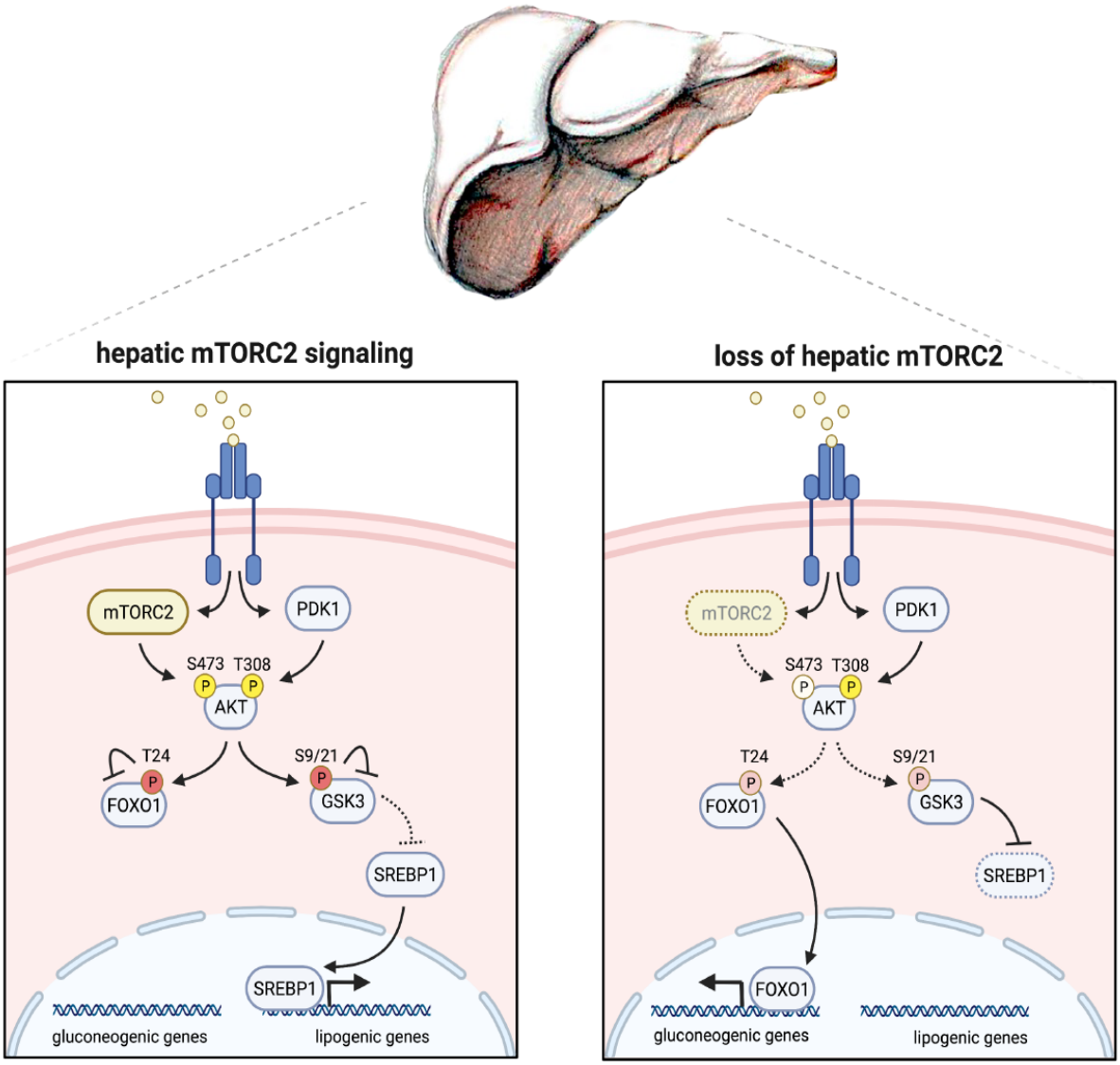

Figure 4. mTORC2 signaling in liver
Canonical insulin-stimulated mTORC2 signaling in the liver. Intact (left) and upon hepatic mTORC2 ablation (right).

transcription of gluconeogenic genes (Biggs, Meisenhelder, Hunter, Cavenee, & Arden, 1999). In mice lacking hepatic mTORC2, insulin fails to suppress FOXO1 activity and thus gluconeogenesis via the reduction of FOXO1-pT24 phosphorylation (Hagiwara et al., 2012). In addition to the reduction of FOXO1-pT24, loss of hepatic mTORC2 also reduces GSK3α/β-pS9/21 phosphorylation (Hagiwara et al., 2012). GSK3α/β-pS9/21 phosphorylation inhibits GSK3 activity thereby preventing proteasomal degradation of SREBP1c (Dong et al., 2015). Proteasomal degradation of SREBP1c prevents the transcription of lipogenic genes such as ACLY, ACC and FASN. Thus, insulin/AKT signaling suppresses the inhibitory effect

of GSK3 on SREBP1c and thereby promotes SREBP1c-induced expression of lipogenic enzymes. Loss of hepatic mTORC2 disrupts the insulin-induced expression of lipogenic enzymes including ACC and FASN (Hagiwara et al., 2012). This observation is in agreement with another study where *rictor* is deleted in mice with hyperactive mTOR signaling in the liver (Guri et al., 2017). Both studies demonstrate the importance of hepatic mTORC2 in the expression of ACC and FASN and thereby DNL. In summary, hepatic mTORC2 suppresses gluconeogenesis and promotes DNL downstream of the insulin signaling pathway. As consequence, mice lacking hepatic mTORC2 develop glucose intolerance, hyperinsulinemia and mild insulin resistance (Hagiwara et al., 2012).

1.2.5. mTORC2 in adipose tissue

Adipose tissue is a heterogeneous tissue composed of adipocytes, fibroblasts, endothelial cells, and immune cells (Corvera, 2021). The composition and function of adipose tissue varies in different fat depots (**Figure 5**). However, there are two main types that significantly differ in their origin and role in whole body energy homeostasis: WAT and brown adipose tissue (BAT).

Role of WAT

The main function of WAT is to store energy in the form of TG (Rosen & Spiegelman, 2006). WAT imports different energy carriers from the bloodstream, most notably FFAs and glucose. Similar to hepatocytes, adipocytes express the fatty acid translocase CD36 that imports FFAs. Imported FFAs are esterified to TGs and then stored in a single large lipid droplet that accounts for up to 90% of the adipocyte cell volume (Haugen & Drevon, 2007). Most storable TGs derive from imported FFA, although a small fraction is generated from imported glucose. Similar to skeletal muscle, insulin-stimulated glucose uptake in adipose tissue is mediated by both AKT and atypical PKC's such as PKCλ and PKCζ (Bandyopadhyay et al., 2002; Nakanishi, Brewer, & Exton, 1993). Imported glucose is then either oxidized for energy production or converted to FFA by DNL. Similar to hepatic DNL, adipose DNL synthesizes FFA from cytosolic acetyl-CoA, a breakdown product of glucose oxidation. However, transcriptional regulation differs in both tissues. In adipocytes, ChREBP is the major driver for DNL while SREBP1c has no effect on the transcription of lipogenic genes (Sekiya et al., 2007; Witte et al., 2015). ChREBP exists in two isoforms in adipose tissue, ChREBPα and ChREBPβ. Glucose influx stimulate ChREBPα activity which promotes ChREBPβ

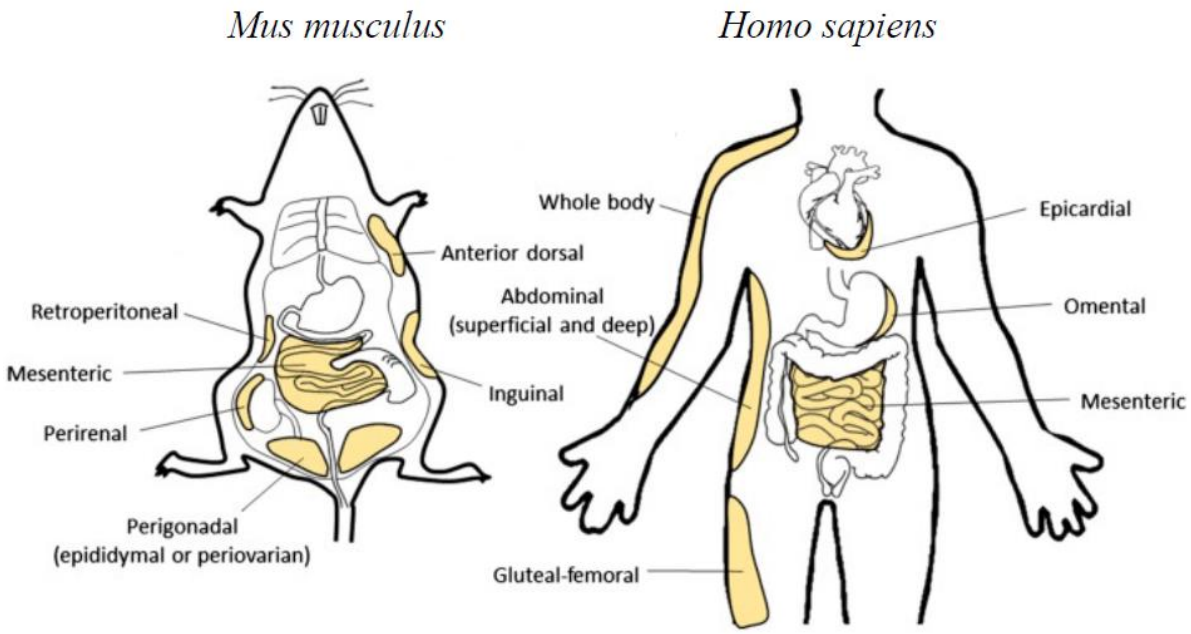

Figure 5. Fat depots human and mouse
Anatomical locations of major white adipose tissue depots in both mice (*Mus musculus*) and humans (*Homo sapiens*). Modified from (Kwok, Lam, & Xu, 2016)**.**

expression (Herman et al., 2012). ChREBPβ then promotes the transcription of lipogenic genes including ACC and FASN. Upon energy shortage, stored TGs are mobilized from lipid droplets in a process called lipolysis. In this process, adipose tissue triglyceride lipase (ATGL), hormone-sensitive lipase (HSL) and monoglyceride lipase (MAG) sequentially hydrolyze TG resulting in the release of FFAs to provide energy for the organism (Duncan, Ahmadian, Jaworski, Sarkadi-Nagy, & Sul, 2007; Grabner, Xie, Schweiger, & Zechner, 2021). Lipolysis is induced by (nor)epinephrine-stimulated β-adrenergic signaling in response to increased energy demand. Briefly, (nor)epinephrine binds to β-adrenergic receptors expressed by adipocytes and stimulate the production of the second messenger cAMP (Collins, 2011). cAMP activates the cAMP-dependent protein kinase A (PKA) which promotes lipolysis by phosphorylating HSL at Ser563 and Ser660.

In healthy humans, WAT accounts for around 20-25% of body mass. However, substantial divergence from optimal fat mass causes metabolic disorders. Metabolic disorders such as lipodystrophy and cachexia are characterized by low fat mass and reduced capacity of adipocytes to store excessive energy. Patients with lipodystrophy or cachexia suffer from severe systemic insulin resistance and glucose intolerance (Vegiopoulos, Rohm, & Herzig,

2017). In contrast, chronic overnutrition and reduced energy expenditure, common in modern lifestyles, increase the accumulation of fat mass. Excessive storage of TGs in adipocytes impairs adipose tissue function with detrimental consequences for whole body energy homeostasis including hyperinsulinemia, insulin resistance and glucose intolerance (Tan & Vidal-Puig, 2008).

Role of BAT

In contrast to white adipocytes, brown adipocytes possess numerous small multilocular lipid droplets and a large number of mitochondria. Brown adipocytes produce heat by promoting non-shivering thermogenesis (Cohen & Kajimura, 2021; Shinde, Song, & Wang, 2021). The best understood mechanism for non-shivering thermogenesis is the decoupling of mitochondrial respiration from ATP production via the uncoupling protein 1 (UCP1). Mitochondrial respiration involves the generation of a proton gradient across the inner mitochondrial membrane via the mitochondrial electron transport chain. Normally, the exported protons flow back into the mitochondrial matrix through the ATP synthase, a process that powers the production of ATP. During non-shivering thermogenesis, UCP1 dissipates the proton gradient across the inner mitochondrial membrane, releasing heat instead of ATP. BAT is a highly vascularized tissue and the generated heat is distributed via the circulation to increase body temperature. It is well established that cold induces non-shivering thermogenesis. Briefly, BAT is innervated by the sympathetic nervous system (SNS) that releases the neurotransmitter norepinephrine (NE) upon cold exposure. NE increases intracellular cAMP levels via β-adrenergic signaling, thereby promoting non-shivering thermogenesis. β-adrenergic signaling in BAT not only increases UCP1 expression, but also promotes lipolysis and glucose uptake to fuel thermogenesis. Due to its high energy demand, thermogenic BAT increases energy expenditure and thus impacts whole-body energy homeostasis (Cohen & Kajimura, 2021).

Brown adipocytes are not the only cell type capable of non-shivering thermogenesis. Beige adipocytes, a cell type present in WAT, also has the capacity for cold-induced non-shivering thermogenesis. Beige adipocytes differ from white adipocytes in their origin and metabolic capacity. In thermoneutral conditions, beige adipocytes are dormant and store TGs similar to white adipocytes. However, cold-induced β-adrenergic signaling induces more UCP1 expression, thermogenesis and adipogenesis in beige adipocytes than in white adipocytes (Cohen & Kajimura, 2021). Not all WAT depots possess equal amounts of beige

adipocytes. While visceral WAT sporadically contains beige adipocytes, a considerable amount of the adipocytes present in subcutaneous WAT are considered beige (Walden, Hansen, Timmons, Cannon, & Nedergaard, 2012).

Adipose tissue in interorgan communication

Whole body energy homeostasis requires tight communication between metabolic organs. To communicate their metabolic state and requirements, BAT, and particularly WAT, secrete so-called adipokines. Adipokines include metabolites, lipids, and bioactive peptides which exert specific effects on a variety of biological processes including inflammation, energy expenditure, hepatic gluconeogenesis, insulin secretion, and insulin sensitivity (Fasshauer & Bluher, 2015; Funcke & Scherer, 2019; Shinde et al., 2021). The best described adipokines are leptin and adiponectin. Both are secreted by mature white adipocytes and regulate metabolic processes in a variety of target tissues. Leptin was discovered in 1994 and subsequent studies have revealed its role in the regulation of satiety, energy expenditure and insulin sensitivity (Bluher & Mantzoros, 2015; Friedman, 2019; Zhang et al., 1994). Circulating leptin is directly proportional to fat mass and exerts its regulatory role by binding the leptin receptor expressed by target cells. Elevated leptin level reduces appetite and food intake via its regulatory function on the hypothalamus. However, chronic elevation of circulating leptin leads to leptin resistance in the central nervous system, thus suppressing satiety-induced reduction of food intake (Savage & O'Rahilly, 2002). Thus, a chronic increase of leptin and the resulting leptin resistance promote nutrition overconsumption, a condition often found in obese and diabetic patients (Farr, Gavrieli, & Mantzoros, 2015). Another adipokine with a well-characterized role in whole-body energy homeostasis is adiponectin. Adiponectin was discovered in 1995 and is exclusively expressed and secreted by adipocytes (Scherer, Williams, Fogliano, Baldini, & Lodish, 1995; Ye & Scherer, 2013). Circulating adiponectin levels inversely correlate with obesity, omental fat distribution and type II diabetes. In contrast, metabolically healthy individuals benefit from the insulin sensitizing and anti-inflammatory effect of adiponectin (Fasshauer & Bluher, 2015; Nedvidkova, Smitka, Kopsky, & Hainer, 2005; Yamamoto et al., 2005).

In addition to adipokines, the adipose tissue also communicates via the peripheral nervous system as both WAT and BAT are innervated by sympathetic and sensory neurons (**Figure 6**). While almost nothing is known about the role of sensory neurons in adipose physiology, the role of SNS is well established (Bartness, Liu, Shrestha, & Ryu, 2014; Blaszkiewicz, Willows, Johnson, & Townsend, 2019).

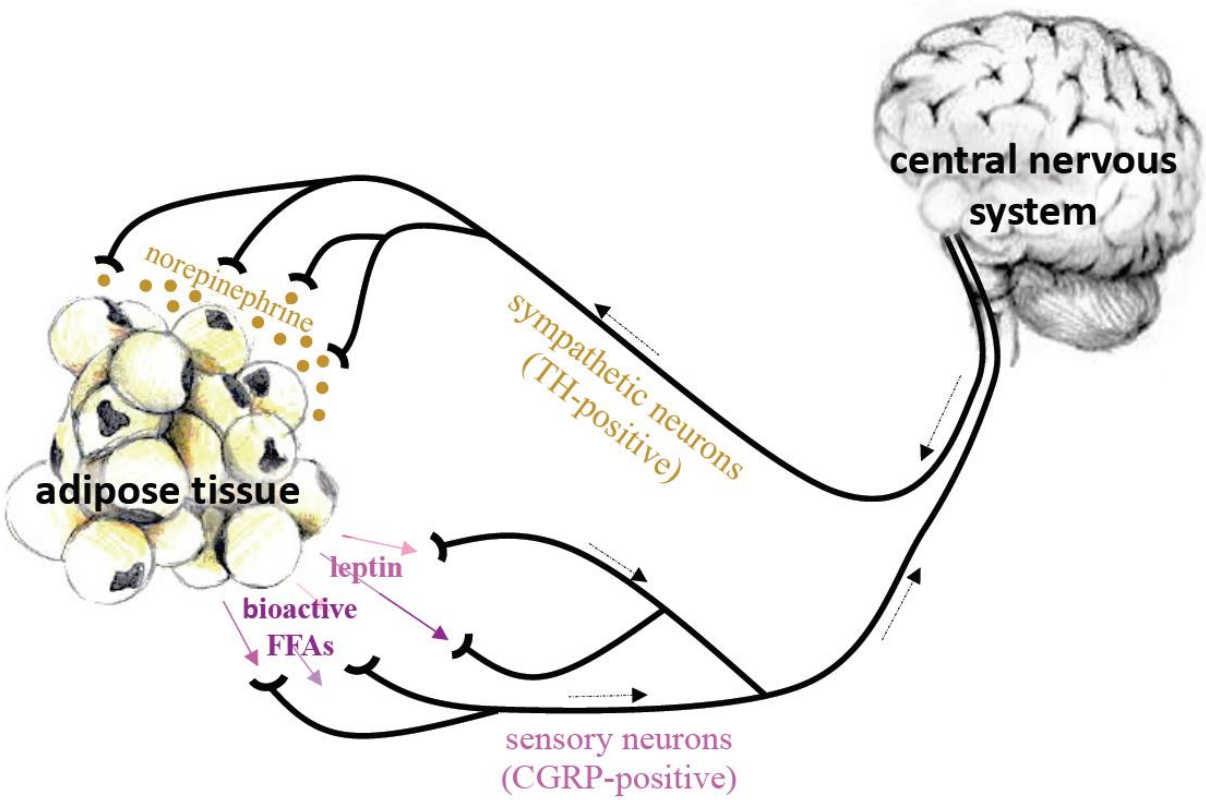

Figure 6. Neuronal innervation
Scheme of sympathetic and sensory innervation in adipose tissue.

The SNS transmits signals from the CNS to WAT via neurons that secrete NE. The CNS is able to register a systemic drop in temperature or energy level and responds by triggering sympathetic neurons to release NE in adipose tissue (Youngstrom & Bartness, 1998). NE then stimulates β-adrenergic signaling and promotes lipolysis and non-shivering thermogenesis as described previously (see Role of BAT section). However, studies using tyrosine hydroxylase (TH, also known as tyrosine-3 monooxygenase), an enzyme catalyzing the rate limiting step of NE synthesis, as a marker for sympathetic neurons have shown that not all fat depots are equally innervated. While epididymal WAT is sparsely innervated, BAT and inguinal WAT contain a dense network of sympathetic neurons (Chi, Wu, et al., 2018). These sympathetic neuronal networks are dynamic and become denser under prolonged cold exposure (Cao, Wang, & Zeng, 2018; Jiang, Ding, Cao, Wang, & Zeng, 2017). In addition, recent studies have shown that the density of the sympathetic neuronal network in WAT correlates with the presence of beige adipocytes. Whether tissue composition impacts the density of the sympathetic neuronal network or sympathetic innervation is regulated by the CNS is still debated (Chi, Wu, et al., 2018; P. Wang et al., 2020).

Compared to the sympathetic nervous system, sensory neurons in adipose tissue are less well characterized. Several studies have detected sensory neuron markers such as calcitonin gene-related peptide (CGRP), substance P and advillin in different fat pads of rodents (Bartness, Shrestha, Vaughan, Schwartz, & Song, 2010; M. T. Foster & Bartness, 2006; Giordano, Morroni, Santone, Marchesi, & Cinti, 1996). Further investigations using electron microscopy confirmed the presence of CGRP- and substance P-positive neurons around the vasculature while only CGRP-positive neurons were present in the parenchyma of adipose tissue (Giordano et al., 1996). The transmission of sensory information from WAT to the CNS has been confirmed in siberian hamsters by an anterograde tracing study using herpes simplex virus H129 (Song, Schwartz, & Bartness, 2009). Adipose-innervating sensory neurons originate from dorsal root ganglia and transmit sensory signals to the same CNS region that controls SNS activity (K. T. Murphy et al., 2013). Thus, a SNS-sensory feedback circuit has been proposed (K. T. Murphy et al., 2013; Song et al., 2009). In agreement with this hypothesis, administration of leptin and free fatty acids stimulates sensory neurons and alters SNS activity in distal fat pads (Garretson et al., 2016; K. T. Murphy et al., 2013; Niijima, 1998). However, the full range of sensory stimuli and its physiological impact on whole body energy homeostasis is unknown. Taken together, previous findings suggest that sensory neurons monitor the metabolic state of adipose tissue and transmit information to the CNS where the sensory inputs are processed to regulate SNS activity accordingly. Nevertheless, the morphology, role and regulation of the sensory nervous system in adipose tissue is still poorly understood.

Role of adipose mTORC2

In WAT, mTORC2 promotes several insulin-regulated processes including glucose uptake, lipid uptake, DNL and TG synthesis (Cybulski, Polak, Auwerx, Ruegg, & Hall, 2009; Hsiao et al., 2020; Tang et al., 2016) (**Figure 7**). Mechanistically, *rictor* deletion in adipocytes abolishes AKT-pS473 phosphorylation and reduces PKC protein levels while the rest of the insulin signaling cascade remains intact (Albert et al., 2016; Cybulski et al., 2009; Hsiao et al., 2020; Kumar et al., 2010; Tang et al., 2016; Yu et al., 2019). Since full AKT activation and PKC expression are required for insulin-stimulated GLUT4 translocation to the plasma membrane, loss of adipose mTORC2 impairs insulin-stimulated glucose uptake. In addition,

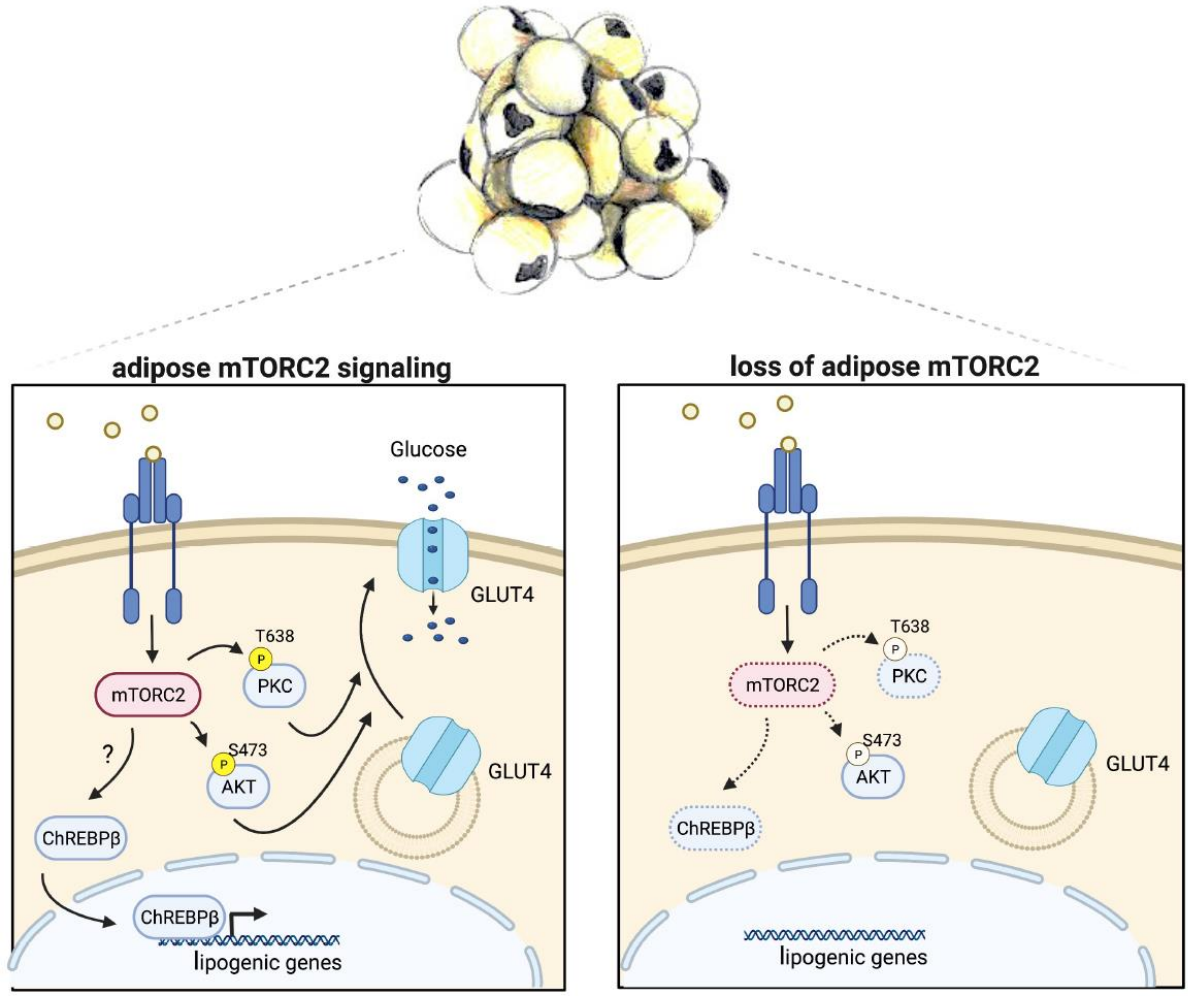

Figure 7. mTORC2 signaling in adipose tissue
Canonical mTORC2 signaling in adipose tissue. Intact (left) and upon adipose mTORC2 ablation (right).

mTORC2 ablation impairs DNL by downregulating the expression of ChREBPβ and the lipogenic enzymes ACC and FASN (Tang et al., 2016)

While the role of mTORC2 in WAT is well established, the role of mTORC2 in BAT is controversial. Albert *et al.* have shown that mTORC2 mediates β-adrenergic-stimulated glucose uptake in BAT to promote non-shivering thermogenesis (Albert et al., 2016). In contrast, a recent study claims that adipose mTORC2 promotes thermogenesis via a glucose-independent mechanism (Castro et al., 2021). However, both studies used a mouse model where mTORC2 was simultaneously abolished in WAT and BAT. Since WAT is important to fuel non-shivering thermogenesis (Shin et al., 2017), lack of mTORC2 in WAT may also impact cold adaption in mice. In agreement with this, mice lacking mTORC2 specifically in BAT ($RICTOR^{UCP1\text{-}Cre}$) display increased non-shivering thermogenesis due to enhanced lipolysis and lipid uptake (Jung et al., 2019).

In addition to the profound effects on adipocyte metabolism, loss of adipose mTORC2 impairs whole-body energy homeostasis. Mice lacking adipose mTORC2 develop hyperinsulinemia, insulin resistance and aberrant liver signaling indicating a still uncharacterized role of adipose mTORC2 in interorgan communication (Cybulski et al., 2009; Hsiao et al., 2020; Kumar et al., 2010; Tang et al., 2016; Yu et al., 2019).

1.3. Recent advances using imaging techniques applied to whole-adipose tissue

Adipocytes are in constant contact and communication with the rest of the body via the vasculature and peripheral neurons. Since conventional methods such as 2D paraffin- or cryosections provide only limited spatial information, it is difficult to visualize and study delicate structures such as neurons or capillaries in WAT sections. The development of whole-adipose tissue imaging has enabled for the first time characterization of the morphology of vascular and neuronal networks present in WAT. The first study visualizing blood vessels and neurons in WAT using whole-adipose tissue imaging appeared in 2015 (Zeng et al., 2015). In this study, the authors visualized the sympathetic nervous system and confirmed the presence of sympathetic neurons in large nerve bundles. Furthermore, the study provided evidence of a regulatory role for WAT-innervating sympathetic neurons in leptin-driven lipolysis. This was followed two years later by another study which revealed the presence of a dense network of sympathetic neurons in the WAT parenchyma that is essential for cold-induced beiging (Jiang et al., 2017). This dense network provides close contact between around 91.3% of adipocytes and the SNS. Further investigation revealed the dynamic nature of this sympathetic neuronal network in mice subjected to cold exposure. Cold exposure promoted arborization of TH-positive sympathetic neurons in inguinal WAT depots which was reversible upon return to thermoneutrality (Cao, Wang, & Zeng, 2018). The density of the sympathetic neuronal network is not only dependent on external conditions, but also varies between the different fat depots. Yet another study reported significant intra-adipose variation of sympathetic nerve fibres and a unique architecture in different fat pads (Chi, Wu, et al., 2018). The authors of this study also found evidence that the density of sympathetic projections is dependent on PRD1-BF1-RIZ1 homologous domain-containing protein-16 (PRDM16), a transcription coregulator present in brown and beige adipocytes. This observation is in contrast to another study which argues that sympathetic innervation is

regulated by the CNS (P. Wang et al., 2020). Thus, the regulation of sympathetic innervation and architecture is still debated.

In contrast to the sympathetic nervous system, the sensory nervous system has not yet been fully visualized. Whole-adipose tissue imaging was used to confirm the presence of CGRP-positive neurons in the large nerve bundles and close to the blood vessels, but the study failed to visualize CGRP-positive neurons in the parenchyma (Makwana et al., 2021).

In addition to the neuronal networks, whole-adipose tissue imaging is also used to uncover the morphology of the intra-adipose vasculature. One study revealed a dense network of capillaries in the parenchyma of WAT by staining for isolectin 4 (Cao, Wang, Wang, Han, & Zeng, 2018). Surprisingly, the authors showed that cold exposure not only stimulated arborization of sympathetic neurons but also promoted vascularization.

New techniques are constantly being introduced that provide higher magnification and better resolution of vascular and neural structures in adipose tissue (Willows et al., 2021). These recent technical advances will in time provide novel insights into the morphology of vascular and neuronal networks and allow the visualization of interactions between capillaries, neurons and adipocytes.

Chapter 2: Aims of the thesis

2. Aims of the thesis

Dysregulation of mTORC2 signaling in adipose tissue is associated with metabolic disorders such as obesity and type II diabetes. The physiological role of adipose mTORC2 signaling has been extensively investigated in transgenic mice lacking the essential mTORC2 core component RICTOR in adipocytes. These studies have highlighted the importance of mTORC2 signaling in glucose uptake and DNL. In addition to a direct impact on adipocyte metabolism, loss of adipose mTORC2 disrupts whole-body energy homeostasis. Mice lacking adipose mTORC2 display hyperinsulinemia, systemic insulin resistance and aberrant hepatic insulin signaling, indicating distal perturbations in the pancreas and liver. As adipose tissue is an endocrine organ, we hypothesized that adipose mTORC2 may play a role in interorgan communication and promotes pancreas and liver function. Since previous studies used mice lacking adipose mTORC2 from birth, phenotypes may derive from defective adipocyte development or maturation. We therefore generated a tamoxifen-inducible adipose-specific RICTOR knockout (iAdRiKO) mouse line to study the consequences of acute loss of mTORC2 signaling in mature adipocytes. By performing a longitudinal study in these iAdRiKO mice, we sought to address the following questions:

1. How fast does the disruption of whole-body energy homeostasis occur after loss of mTORC2 signaling?
2. Which pathways change upon acute loss of adipose mTORC2 signaling?
3. Which, if any, of these pathways are responsible for the disruption of whole-body energy homeostasis upon loss of adipose mTORC2?

As previous publications have highlighted the importance of WAT in energy storage, we next hypothesized that loss of adipose mTORC2 may disrupt whole-body energy homeostasis by preventing energy storage. To address this hypothesis, we posed the following questions:

1. Does loss of adipose mTORC2 in mature adipocytes reduce the capacity of WAT to store energy?
2. What are the consequences of reduced storage capacity in WAT lacking mTORC2?
3. How important is mTORC2 in the coordination of energy storage for whole-body energy homeostasis?

By addressing these questions, we aim to increase our understanding on the role of mTORC2 in mature adipocytes and its role in whole-body energy homeostasis, thereby providing new insights in the development of major metabolic disorders.

Chapter 3: Results

3. Results

3.1 Manuscript 1:
Adipose mTORC2 is essential for arborization of sensory neurons in white adipose tissue

Irina C Frei[1], Diana Weissenberger[1], Danilo Ritz[1], Wolf Heusermann[1], Marco Colombi[1], Mitsugu Shimobayashi[1#]*, Michael N Hall[1]*

[1] Biozentrum
University of Basel
Basel 4056, Switzerland

[#] Current address: Laboratory of Clinical and Experimental Endocrinology, Department of Chronic Diseases and Metabolism, KU Leuven, Leuven 3000, Belgium

[*] Corresponding authors:
e-mail: mitsugu.shimobayashi@kuleuven.be (MS) or m.hall@unibas.ch (MNH)

3.1.1. Abstract

Adipose tissue, via sympathetic and sensory neurons, communicates with the CNS to mediate energy homeostasis. In contrast to the sympathetic nervous system, the morphology, role and regulation of the sensory nervous system in adipose tissue is poorly characterized. Taking advantage of recent progress in whole-mount three-dimensional imaging of adipose tissue, we identified a neuronal network of CGRP-positive sensory neurons in WAT. Furthermore, we show that adipose mTORC2, a major component of the insulin signaling pathway, mediates sensory innervation in WAT. Based on visualization of neuronal networks, mTORC2-deficient WAT displayed reduced arborization of CGRP-positive sensory neurons, while sympathetic neurons were unaffected. This selective loss of sensory innervation followed reduced expression of growth-associated protein 43 (GAP43) in CGRP-positive sensory neurons. Finally, we found that loss of sensory innervation in WAT correlated with systemic insulin resistance. Our findings suggest that adipose mTORC2 is necessary for sensory innervation in WAT which likely contributes to WAT-to-CNS communication.

Keywords

adipose tissue, whole-body energy homeostasis, mTORC2, sensory nervous system, diabetes, CGRP, neuropathy

3.1.2. Introduction

WAT stores or releases energy and thereby contributes to whole-body energy homeostasis (Rosen & Spiegelman, 2006). Impaired WAT function, often the result of obesity, causes systemic effects such as hyperinsulinemia and insulin resistance (Longo et al., 2019; Tan & Vidal-Puig, 2008), indicating that the metabolic state of WAT impacts other tissues. With the increasing prevalence of obesity and type II diabetes, it is important to understand how WAT communicates with distal tissues to control whole-body energy homeostasis.

It is well established that WAT communicates with other tissues, including the brain, by secreting adipokines such as leptin and adiponectin (Fasshauer & Bluher, 2015; Funcke & Scherer, 2019). WAT also interacts with the CNS via sympathetic and sensory neurons (Bartness et al., 2014; Blaszkiewicz, Willows, Johnson, et al., 2019; Guilherme, Henriques, Bedard, & Czech, 2019). The sympathetic nervous system transmits signals from CNS to WAT. For example, fasting triggers sympathetic neurons to release the neurotransmitter NE in WAT. NE then stimulates adipocytes to release free fatty acids that provide energy for

other tissues (Youngstrom & Bartness, 1998). Compared to the sympathetic nervous system, sensory neurons in WAT are less well studied. Detection of the sensory neuron markers CGRP, substance P and advillin first suggested the presence of sensory neurons in WAT (Bartness et al., 2010; M. T. Foster & Bartness, 2006; Giordano et al., 1996; Willows et al., 2021). Anterograde tracing using herpes simplex virus subsequently confirmed the transmission of sensory information from WAT to CNS (Song et al., 2009). Further studies identified the adipokine leptin and bioactive free fatty acids as potential sensory stimuli in WAT (Garretson et al., 2016; Niijima, 1998). Nevertheless, the morphology, role and regulation of the sensory nervous system in WAT remain poorly understood.

mTORC2 is a multiprotein serine/threonine kinase. It is composed of four core components including the kinase subunit mTOR and the mTORC2-specific subunit rapamycin-insensitive companion of mTOR (RICTOR) (Jacinto et al., 2004; Loewith et al., 2002; Sarbassov et al., 2004). Studies of adipose-specific *Rictor* knockout mice revealed that loss of adipose mTORC2 causes reduced glucose uptake and impaired lipid handling in adipocytes (Albert et al., 2016; Cybulski et al., 2009; Hsiao et al., 2020; Kumar et al., 2010; Tang et al., 2016; Yu et al., 2019). Furthermore, loss of adipose mTORC2 non-cell-autonomously causes hyperinsulinemia and systemic insulin resistance (Cybulski et al., 2009; Kumar et al., 2010; Tang et al., 2016). These data suggest that adipose mTORC2 is a critical regulator of systemic energy homeostasis. However, the mechanisms by which adipose mTORC2 mediates communication with other tissues are poorly understood.

We used iAdRiKO mice to study how adipose mTORC2 mediates WAT communication with other tissues. Phosphoproteomic analysis of inguinal WAT (iWAT) from iAdRiKO mice revealed acute changes in phosphorylation of proteins associated with neurons. To study the effect of adipose mTORC2 on neurons, we visualized sympathetic and sensory neuronal networks in iWAT by performing whole-mount imaging. We discovered that arborization of CGRP-positive sensory neurons, but not TH-positive sympathetic neurons, was selectively diminished in WAT upon loss of adipose mTORC2. Furthermore, expression of growth-associated protein 43 (GAP43) in CGRP-positive sensory neurons was reduced prior to loss of arborization. We conclude that adipose mTORC2 is required for arborization of sensory neurons in WAT, thereby mediating adipocyte-to-CNS communication.

3.1.3. Results

Loss of adipose mTORC2 acutely impairs whole-body energy metabolism. Mice lacking adipose mTORC2 from birth display a defect in whole-body energy homeostasis characterized by hyperinsulinemia and systemic insulin resistance (Cybulski et al., 2009; Kumar et al., 2010; Tang et al., 2016). Since adipose tissue is not fully developed until six weeks of age, this could be due to a developmental defect. To determine whether and, if so, how soon loss of mTORC2 in mature adipocytes causes systemic effects, we performed a longitudinal study with a tamoxifen-inducible *Rictor* knockout (*Rictor*$^{fl/fl}$, *Adipoq promoter*-CreER^{T2}) mouse (**Figure 1A**). Six week old mice were treated with tamoxifen daily for five days and analyzed three days, two weeks, and four weeks after the last tamoxifen treatment (**Figure 1A**). *Cre*-negative mice treated with tamoxifen served as controls. As expected, expression of RICTOR and phosphorylation of the mTORC2 target AKT (AKT-pS473) were downregulated in WAT of iAdRiKO mice at all three post-tamoxifen timepoints (**Figure S1A**). In liver and muscle, RICTOR expression and AKT phosphorylation were not affected (**Figure S1B**). Loss of mTORC2 in mature adipocytes reduced WAT mass approximately 30% compared to control mice (**Figures 1B and S1C**), while BAT mass was unchanged (**Figure S1D**).

Next, we characterized the metabolic state of iAdRiKO and control mice. Fasting insulin levels were acutely increased in iAdRiKO mice and remained significantly elevated while blood glucose levels remained normal (**Figure 1C**). These results suggest that elevated insulin compensates for reduced insulin sensitivity upon loss of mTORC2, as observed previously in mice lacking adipose mTORC2 at birth (Cybulski et al., 2009; Tang et al., 2016). In agreement with this suggestion, loss of mTORC2 reduced glucose uptake in WAT (**Figures S1E-F**). Furthermore, iAdRiKO mice become insulin resistant, as determined by an insulin tolerance test (**Figures 1D-F**). Severe insulin resistance was detected in iAdRiKO mice at two and four weeks (**Figures 1E-F and S1G**). Further investigation revealed mild insulin resistance in iAdRiKO mice at five days after tamoxifen treatment (**Figures S1H-I**), indicating a gradual development of insulin resistance within two weeks after loss of adipose mTORC2 (**Figures 1F and S1I**). Taken together, these longitudinal studies revealed rapid development of hyperinsulinemia followed by insulin resistance upon loss of adipose mTORC2. These results highlight the importance of adipose mTORC2 for whole-body energy homeostasis.

Loss of mTORC2 alters proteins associated with synapse formation in WAT. To gain better understanding of the role of adipose mTORC2 in whole-body energy homeostasis, we performed proteomic and phosphoproteomic analyses on iWAT obtained from iAdRiKO and control mice three days after tamoxifen treatment. This time point allowed us to study the acute effects of reduced mTORC2 activity (**Figure S1A**), before development of systemic insulin resistance (**Figures 1D-F**). The proteomic analysis identified and compared 6'082 proteins in iWAT of iAdRiKO and control mice. Only one protein was significantly altered in AdRiKO mice three days after tamoxifen treatment (40S ribosomal protein S24; $p < 0.01$; $|\log_2(\text{iAdRiKO/control})| > 0.6$) (**Figure 2A**). In contrast, the phosphoproteomic analysis detected and quantified 10'443 phosphorylated sites of which 319 and 249 were significantly up- and down-regulated ($p<0.01$), respectively, upon loss of adipose mTORC2 (**Figure 2B**). As expected, mTORC2 downstream readouts AKT1-pS473, ACLY-pS455 (Martinez Calejman et al., 2020), NDRG1-pS330 (Murray et al., 2004) and MARCKS-pS152/156 (Aderem, 1992) were downregulated in iWAT of iAdRiKO mice compared to control iWAT (**Figure 2C**). Next, we examined whether loss of mTORC2 in adipocytes elicits a molecular signature. Indeed, unsupervised hierarchical clustering analysis (**Figure 2D**) and principal component analysis (PCA) (**Figure 2E**) of the phosphoproteomic data identified two distinct clusters corresponding to iAdRiKO mice and control mice.

To identify molecular processes associated with loss of mTORC2 signaling, we performed pathway enrichment analysis. Proteins whose phosphorylation was significantly altered were associated with the plasma membrane and cell-cell adhesion (**Figure 2F**). This observation is in agreement with previous studies showing that many mTORC2 substrates are localized to the plasma membrane (Keenan & Kelleher, 1998; Manning & Toker, 2017). Unexpectedly, the pathway enrichment analysis also revealed changes in proteins associated with the nervous system, in particular synapse-associated proteins (**Figure 2F**). To investigate the possibility of ectopic Adipoq promoter-CreER^{T2} expression and thus mTORC2 ablation in neurons, we examined adiponectin expression in neurons in iWAT. We found no evidence for adiponectin expression in nerve bundles innervating iWAT (**Figure S2**). This finding is supported by large-scale single-cell RNA sequence data performed in dorsal root ganglion of mice (Usoskin et al., 2015), where iWAT-innervating sensory neurons originate. Thus, changes in phosphorylation of synapse-associated proteins are unlikely due to ectopic ablation of mTORC2 in neurons. Based on these findings, we hypothesize that loss of adipose mTORC2 impacts the neuronal network in iWAT. Furthermore, our findings suggest that the

acute effects of mTORC2 loss are due to changes in protein phosphorylation rather than expression, as expected for loss of a kinase.

Loss of adipose mTORC2 reduces arborization of sensory neuron. To investigate the consequences of altered phosphorylation of synaptic proteins, as observed upon acute loss of adipose mTORC2, we examined neuronal innervation in iWAT four weeks after tamoxifen treatment. We first examined the sympathetic nervous system by visualizing TH-positive neurons in iWAT, using a modified whole-mount volumetric imaging protocol (Chi, Crane, Wu, & Cohen, 2018; Jiang et al., 2017). We combined the tissue preparation protocol described by Chi et *al*. (2018a) with a water-based clearing method (Tainaka et al., 2018) to enhance structure preservation and antibody combability. As previously described (Chi, Wu, et al., 2018; Jiang et al., 2017), we detected a dense network of TH-positive sympathetic neurons in nerve bundles that branched into smaller fibers running along blood vessels and into the parenchyma (**Figure S3A**). However, we found no change in abundance or morphology of TH-positive sympathetic neurons in iWAT of iAdRiKO mice, compared to controls (**Figure 3A**). In agreement with this result, immunoblot analyses showed no change in TH expression in iWAT of iAdRiKO mice (**Figure 3B**). Next, we analyzed the activity of sympathetic neurons in iWAT. TH-positive neurons release NE to stimulate β-adrenergic signaling in adipocytes, which promotes phosphorylation of HSL at S563 and S660 (Anthonsen, Ronnstrand, Wernstedt, Degerman, & Holm, 1998; Zeng et al., 2015). Immunoblot analyses revealed no difference in phosphorylation of S563 or S660 (**Figure 3B**), indicating similar sympathetic activity in iAdRiKO and control mice. Taken together, these findings suggest that the morphology and activity of the sympathetic nervous system are normal in iWAT of iAdRiKO mice.

We next examined the sensory nervous system in iWAT. Since the three-dimensional sensory neuronal network in iWAT was not previously described, we first examined CGRP-positive sensory neurons in control mice. Similar to TH-positive neurons, CGRP-positive sensory neurons innervated iWAT via large nerve bundles (**Figure 3C**). From the large nerve bundles, smaller nerve bundles branched off and ran along blood vessels into the tissue (**Figure 3C**). Using high magnification imaging, we detected single nerve fibers branching out into the parenchyma where sensory neurons were in close contact with adipocytes (**Figure 3C**).

Next, we analyzed the sensory neuronal network in iWAT of iAdRiKO mice. CGRP-positive sensory neurons were present in large and small nerve bundles similar to control mice

(**Figures 3C and S3B).** Importantly, unlike control mice, we did not detect CGRP-positive neurons in the parenchyma, indicating loss of arborization of sensory neurons in iWAT of iAdRiKO mice (**Figures 3C and S3B**). Loss of CGRP in iWAT lacking mTORC2 was also observed by an enzyme-linked immunosorbent assay (ELISA) (**Figure S3C**). To further investigate the loss of CGRP-positive sensory neurons in iWAT, we co-stained and visualized TH- and CGRP-positive neurons in whole iWAT depots collected from iAdRiKO and control mice. We discovered that TH- and CGRP- positive neurons were present in the same larger and smaller nerve bundles and ran alongside each other into the tissue (**Figures 4A and S4A-B**). However, the TH-positive sympathetic neuronal network was much denser compared to the sensory neuronal network, particularly in the parenchyma. Confirming the above observations, sensory neurons were not detected in the parenchyma of iAdRiKO iWAT, while sympathetic neurons were detected (**Figures 4B-C and S5**). Taken together, these findings suggest that adipose mTORC2 is required for arborization of CGRP-positive sensory neurons, but not of sympathetic neurons, in iWAT.

We noted that the intensity of CGRP staining was slightly reduced in the main nerve bundles of iAdRiKO iWAT (**Figures 3C and 4A**). To confirm this observation, we performed co-staining of TH and CGRP in paraffin sectioned iWAT (**Figure S6A**). The number of CGRP-positive single fibers was similar in nerve bundles of iAdRiKO and control mice. However, the intensity of CGRP per fiber was reduced 40% in iAdRiKO iWAT (**Figures S6A-B**). Consistent with the whole-mount imaging (**Figure 3A**), we detected no change in TH intensity in iWAT of iAdRiKO mice (**Figures S6A and S6C)**. The reduction of CGRP in single nerve fibers, in addition to loss of arborization, may indicate a loss in sensory activity.

GAP43 expression is downregulated in CGRP-positive neurons upon loss of adipose mTORC2. We next investigated how loss of adipose mTORC2 reduces arborization of CGRP-positive neurons in iWAT. We examined neuronal GAP43, a protein that promotes neuronal growth and plasticity in the CNS (Snipes et al., 1987). GAP43 was previously shown to be downregulated in iWAT of *ob/ob* mice, a mouse model for type II diabetes (Blaszkiewicz, Willows, Dubois, et al., 2019). Immunoblot analysis of total and phosphorylated (pS41) GAP43 showed a strong decrease in GAP43 expression in iWAT lacking mTORC2, at two and four weeks after tamoxifen treatment (**Figures 5A-B**). Since WAT is a heterogenous tissue, we next examined whether GAP43 is expressed only in neurons. We determined GAP43 expression in surgically denervated iWAT, observing that GAP43 expression was indeed lost upon denervation (**Figure**

5C). These data suggest that GAP43 is expressed only in neurons and thus the loss of GAP43 observed in iWAT of iAdRiKO is due to loss in the nervous system.

Previous reports showed that GAP43 can be expressed in both sensory and sympathetic neurons (Fantini & Johansson, 1992; Schmidt, Spencer, Coleman, & Roth, 1991). To address which class of neurons express GAP43 in iWAT, we visualized GAP43 in TH- or CGRP-positive neurons in large nerve bundles in sectioned iWAT. We note that we visualized GAP43 with antibody against phosphorylated GAP43 because antibody against total GAP43 did not serve as an immunostaining reagent. We found that the GAP43-pS41 signal correlated with CGRP-positive fibers, but not with TH-positive fibers, indicating that GAP43 is expressed specifically in sensory neurons in iWAT (**Figures 5D-E**). Considering the established role of GAP43 in neuronal growth (Snipes et al., 1987), our data suggest that loss of adipose mTORC2 reduces arborization of CGRP-positive neurons possibly due to loss of neuronal GAP43 expression.

3.1.4. Discussion

In this study, we provide insight on the morphology, role and regulation of the sensory nervous system in WAT. Taking advantage of recent progress in whole-mount three-dimensional imaging, we show that sensory neurons are present in central nerve bundles, along blood vessels and in the parenchyma of WAT. Furthermore, we discovered that loss of mTORC2 signaling in adipocytes decreases arborization of sensory neurons without affecting sympathetic innervation or activity. Our findings suggest that adipose mTORC2 promotes growth (arborization) of CGRP-positive sensory neurons in WAT, thereby supporting adipocyte-to-CNS communication.

The morphology of the sensory nervous system in WAT has not been described previously. We show that CGRP-positive sensory neurons, like TH-positive sympathetic neurons, innervate the parenchyma of WAT. We note that the sensory nervous system forms a less dense network compared to the sympathetic nervous system. Nevertheless, sensory neurons appear to contact adipocytes (**Figure 4C**). The nature of these connections is still unknown, since sensory neurons may form stable synapses with adipocytes or terminate as free nerve endings. However, the close proximity of adipocytes and sensory neurons provides morphological evidence for adipocyte-to-CNS communication via the sensory nervous system.

The role of sensory neurons in WAT is poorly understood. It has been proposed that sensory neurons may directly communicate the metabolic state of WAT to CNS (Garretson et

al., 2016; Niijima, 1998; Song et al., 2009). Indeed, leptin and species of free fatty acids have been identified as potential sensory stimuli acting in WAT (Garretson et al., 2016; Niijima, 1998). Our data provide additional evidence for this hypothesis since arborization of sensory neurons is lost upon ablation of adipose mTORC2, a critical regulator of energy uptake and storage in WAT (Hsiao et al., 2020; Tang et al., 2016). In addition, the observed reduction of sensory innervation in WAT lacking mTORC2 coincides with hyperinsulinemia and insulin resistance. Accordingly, CGRP-positive neurons in iWAT may impact whole body energy homeostasis via the CNS, although ablation of CGRP-positive neurons specifically in BAT had no impact on whole-body energy homeostasis (Makwana et al., 2021). Further studies are needed to elucidate the potential role of WAT-derived sensory neurons in controlling energy homeostasis.

How does adipose mTORC2 regulate growth of CGRP-positive sensory neurons in WAT? We observed that loss of mTORC2 correlates with loss of the neuronal growth promoting protein GAP43. An intriguing possibility is that adipose mTORC2 promotes GAP43 expression in sensory neurons. Since GAP43 is expressed only in sensory neurons (**Figures 5D-E**), this hypothesis explains why CGRP-positive neurons, but not TH-positive neurons, are affected in iWAT of iAdRiKO mice. GAP43 is found at the presynaptic membrane and at neuronal growth cones (Snipes et al., 1987). Our phosphoproteomic analysis revealed that phosphorylation of both membrane-associated proteins and cell-cell adhesion proteins was altered upon loss of adipose mTORC2 (**Figure 2F**). Thus, loss of mTORC2 in adipocytes may disrupt the postsynaptic membrane, thereby destabilizing synapses and affecting pre-synaptic GAP43 expression. Alternatively, CGRP-positive sensory neurons may require a secreted stimulus from adipocytes to undergo arborization. It has been suggested that sensory neurons respond to secreted free fatty acids produced by lipolysis or *de novo* lipogenesis in adipocytes (Garretson et al., 2016; Guilherme et al., 2018). Since mTORC2 promotes *de novo* lipogenesis (Hagiwara et al., 2012; Tang et al., 2016), loss of mTORC2 may decrease production and thus release of free fatty acids by adipocytes which may in turn decrease arborization of sensory neurons. Further studies are required to uncover the molecular mechanism underlying adipose mTORC2-mediated regulation of CGRP-positive sensory neurons in iWAT.

Loss of sensory neurons has been observed in diabetic patients, a condition known as diabetic-induced neuropathy (Kobayashi & Zochodne, 2018). However, the underlying mechanism(s) is poorly understood. Blaszkiewicz et al. have reported that GAP43-positive neurons are lost in iWAT in genetically obese (*ob/ob*) mice (Blaszkiewicz, Willows, Dubois,

et al., 2019). Since a decrease in mTORC2 has previously been shown in omental WAT of obese patients (Shimobayashi et al., 2018), it will also be of interest to investigate a possible correlation between loss of CGRP-positive neurons and reduced mTORC2 activity in WAT as a potential mechanism of diabetes-induced neuropathy.

3.1.5. Materials and Methods

Mice. As described before, the iAdRiKO mouse line was generated by breeding *Rictor*$^{fl/fl}$ mice with *adipoq-CreER*^{T2} mice, provided by Stefan Offermanns (Max Planck Institute for Heart and Lung Research [MPI-HLR], Bad Nauheim, Germany) (Sassmann, Offermanns, & Wettschureck, 2010; Shimobayashi et al., 2018). For experiments, *Rictor*$^{fl/fl}$ *adipoq-CreER*^{T2} mice were bred with *Rictor*$^{fl/fl}$ mice to generate iAdRiKO and control littermates. *Rictor* knockout was induced at 6 weeks of age. For that, iAdRiKO and control littermates were treated with i.p. injection daily with 1 mg/mouse tamoxifen (Sigma-Aldrich) resuspended in corn oil for consecutive 5 days. Mice were housed at 22 °C in a regulation compliant facility under a 12-hour light/12-hour dark cycle with unlimited access to water and normal diet (unless stated otherwise). Mice were sacrificed early in the morning and tissues were collected and weighed. All mouse experiments were performed according to federal guidelines for animal experimentation and were approved by the Kantonales Veterinäramt of the Kanton Basel-Stadt under the cantonal license 2602 and 2975.

2-Deoxyglucose uptake assay. Mice were fasted for five hours, then injected i.p. with Humalog insulin (Lilly; 0.75 U/kg body weight), followed 10 minutes later with an injection of 2-deoxyglucose (Sigma- Aldrich; 32.8 µg/g body weight). Tissues were collected 20 minutes after administration of 2-deoxyglucose. Tissues were lysed in 10 mM Tris-HCL, pH 8.0, by boiling for 15 minutes. 2-Deoxyglucose-6-phosphate (2DGP) was measured using a Glucose Uptake-Glo Assay Kit (Promega) following the manufacturer's instructions.
Insulin tolerance test. Mice were fasted for 5 hours and blood samples were collected to determine blood glucose levels. Humalog insulin was given i.p. (Lilly; 0.75 U/kg body weight), and blood glucose levels were monitored by an Accu-Chek blood glucose meter for 90 minutes.
Immunoblots. Tissue were homogenized in lysis buffer containing 100 mM Tris-HCl pH 7.5, 2 mM EDTA, 2 mM EGTA, 150 mM NaCl, 1% Triton X-100, cOmplete inhibitor cocktail (Roche) and PhosSTOP (Roche). Protein concentration was determined by Bradford assay.

Equal amounts of protein were separated by SDS-PAGE and transferred onto nitrocellulose membranes (GE Healthcare). The nitrocellulose membranes were blocked with 5% BSA in TBST (TBS containing 0.1% Tween20) and incubated overnight in primary antibody diluted in TBST containing 5% BSA. Primary antibodies used were RICTOR (1:1000; Cell signaling; Cat#2140), AKT (1:1000; Cell signaling, Cat#4685), AKT-pS473 (1:1000; Cell signaling, Cat#9271), CALNEXIN (1:1000, Enzo, Cat#ADI-SPA-860-F), GAP43 (1:1000, Cell signaling, Cat#8945), GAP43-pS41 (1:1000, R&D Systems, Cat#PPS006), Tyrosine hydroxylase (1:500, Millipore, Cat#AB1542), HSL (1:2000, Cell signaling, Cat#4107), HSL-pS660 (1:1000, Cell signaling, Cat#4126), HSL-pS563 (1:1000, Cell signaling, Cat#4139). The primary antibody was washed several times with TBST and then incubated in secondary antibody in TBST containing 5% milk powder (w/v). Secondary antibodies used were mouse anti-rabbit (1:10'000, Jackson, 211-032-171) and rabbit anti-sheep (1:10'000, Invitrogen, 81-8620).

Sample preparation for proteomics and phosphoproteomics. Tissues were pulverized and homogenized in lysis buffer containing 100 mM Tris-HCl pH7.5, 2 mM EDTA, 2 mM EGTA, 150 mM NaCl, 1% Triton X-100, cOmplete inhibitor cocktail (Roche) and PhosSTOP (Roche). Samples were lysed by polytron followed by ultrasonication. Lysates was further cleared from debris and excessive amount of lipids by centrifugation (2x14'000g, 10min). Proteins were precipitated by trichloroacetic acid (Sigma), washed with cold acetone and resuspended in buffer containing 1.6 M urea, 0.1 M ammonium bicarbonate and 5 mM TCEP. Proteins were alkylated with 10 mM chloroacetamide and digested with sequencing-grade modified trypsin (enzyme/protein ratio 1:50) overnight. After acidification with 5% TFA, peptides were desalted using C18 reverse-phase spin columns (Macrospin, Harvard Apparatus) according to the manufacturer's instructions, dried under vacuum and stored at -20 °C until further use.

For TMT-labelling, 25 µg of peptides per sample were labeled with isobaric tandem mass tags (TMT10plex, Thermo Fisher Scientific) as described previously (Ahrne et al., 2016). In brief, peptides were resuspended in 20 µl labeling buffer (2 M urea, 0.2 M HEPES, pH 8.3) and a peptide calibration mixture consisting of six digested standard proteins mixed in different amounts was spiked into each sample before TMT reagents were added, followed by a 1 h incubation at 25 °C shaking at 500 rpm. To quench the labelling reaction, aqueous 1.5 M hydroxylamine solution was added and samples were incubated for another 5 min at 25 °C shaking at 500 rpm followed by pooling of all samples. The pH of the sample pool was

increased to 11.9 by adding 1 M phosphate buffer (pH 12) and incubated for 20 min at 25 °C shaking at 500 rpm to remove TMT labels linked to peptide hydroxyl groups. Subsequently, the reaction was stopped by adding 2 M hydrochloric acid until a pH < 2 was reached. Finally, peptide samples were further acidified using 5% TFA, desalted using Sep-Pak Vac 1cc (50 mg) C18 cartridges (Waters) according to the manufacturer's instructions and dried under vacuum.

Proteomics. TMT-labeled peptides were fractionated by high-pH reversed phase separation using a XBridge Peptide BEH C18 column (3,5 µm, 130 Å, 1 mm x 150 mm, Waters) on an Agilent 1260 Infinity HPLC system. Peptides were loaded on column in buffer A (20 mM ammonium formate in water, pH 10) and eluted using a two-step linear gradient from 2% to 10% in 5 minutes and then to 50% buffer B (20 mM ammonium formate in 90% acetonitrile, pH 10) over 55 minutes at a flow rate of 42 µl/min. Elution of peptides was monitored with a UV detector (215 nm, 254 nm) and a total of 36 fractions were collected, pooled into 12 fractions using a post-concatenation strategy as previously described (Y. Wang et al., 2011) and dried under vacuum. Dried peptides were resuspended in 0.1% aqueous formic acid and subjected to LC–MS/MS analysis using a Q Exactive HF Mass Spectrometer fitted with an EASY-nLC (both Thermo Fisher Scientific) and a custom-made column heater set to 60 °C. Peptides were resolved using a RP-HPLC column (75 µm × 30 cm) packed in-house with C18 resin (ReproSil-Pur C18–AQ, 1.9 µm resin; Dr. Maisch GmbH) at a flow rate of 0.2 µl/min. The following gradient was used for peptide separation: from 5% B to 15% B over 19 min to 30% B over 80 min to 45% B over 21 min to 95% B over 2 min followed by 18 min at 95% B. Buffer A was 0.1% formic acid in water and buffer B was 80% acetonitrile, 0.1% formic acid in water. The Q Exactive HF mass spectrometer was operated in DDA mode with a total cycle time of approximately 1 second. Each MS1 scan was followed by high-collision-dissociation (HCD) of the 10 most abundant precursor ions with dynamic exclusion set to 30 seconds. For MS1, 3e6 ions were accumulated in the Orbitrap over a maximum time of 100 ms and scanned at a resolution of 120,000 FWHM (at 200 m/z). MS2 scans were acquired at a target setting of 1e5 ions, maximum accumulation time of 100 ms and a resolution of 30,000 FWHM (at 200 m/z). Singly charged ions and ions with unassigned charge state were excluded from triggering MS2 events. The normalized collision energy was set to 35%, the mass isolation window was set to 1.1 m/z and one microscan was acquired for each spectrum. The acquired raw-files were converted to the mascot generic file (mgf) format using the msconvert tool (part of ProteoWizard, version 3.0.4624 (2013-6-3)) and searched using

MASCOT against a murine database (consisting of 34026 forward and reverse protein sequences downloaded from Uniprot on 20190129), the six calibration mix proteins (Ahrne et al., 2016) and 392 commonly observed contaminants. The precursor ion tolerance was set to 10 ppm and fragment ion tolerance was set to 0.02 Da. The search criteria were set as follows: full tryptic specificity was required (cleavage after lysine or arginine residues unless followed by proline), 3 missed cleavages were allowed, carbamidomethylation (C) and TMT6plex (K and peptide N-terminus) were set as fixed modification and oxidation (M) as a variable modification. Next, the database search results were imported into the Scaffold Q+ software (version 4.3.2, Proteome Software Inc., Portland, OR) and the protein false identification rate was set to 1% based on the number of decoy hits. Proteins that contained similar peptides and could not be differentiated based on MS/MS analysis alone were grouped parsimoniously. Proteins sharing significant peptide evidence were grouped into clusters. Acquired reporter ion intensities in the experiments were employed for automated quantification and statistical analysis using a modified version of our in-house developed SafeQuant R script(Ahrne et al., 2016). This analysis included adjustment of reporter ion intensities, global data normalization by equalizing the total reporter ion intensity across all channels, summation of reporter ion intensities per protein and channel, calculation of protein abundance ratios and testing for differential abundance using empirical Bayes moderated t-statistics. To meet additional assumptions (normality and homoscedasticity) underlying the use of linear regression models and t-Tests, MS-intensity signals were transformed from the linear to the log-scale. All proteins detected are presented in supplementary table 2. Finally, significantly deregulated proteins were defined as log2 (fold change) > 0.5 or log2(fold change) < -0.5, p-value < 0.01.

Phosphoproteomics. Peptide samples were enriched for phosphorylated peptides using Fe(III)-IMAC cartridges on an AssayMAP Bravo platform as described (Post et al., 2017). Unmodified peptides (“flowthrough”) were subsequently used for TMT analysis. Phospho-enriched peptides were resuspended in 0.1% aqueous formic acid and subjected to LC–MS/MS analysis using an Orbitrap Fusion Lumos Mass Spectrometer fitted with an EASY-nLC 1200 (both Thermo Fisher Scientific) and a custom-made column heater set to 60 °C. Peptides were resolved using a RP-HPLC column (75 µm × 37 cm) packed in-house with C18 resin (ReproSil-Pur C18–AQ, 1.9 µm resin; Dr. Maisch GmbH) at a flow rate of 0.2 µl/min. The following gradient was used for peptide separation: from 5% B to 8% B over 5 min to 20% B over 45 min to 25% B over 15 min to 30% B over 10 min to 35% B over 7 min to 42% B over 5 min to 50% B over 3min to 95% B over 2 min followed by 18 min at 95% B. Buffer

A was 0.1% formic acid in water and buffer B was 80% acetonitrile, 0.1% formic acid in water. The Orbitrap Fusion Lumos mass spectrometer was operated in DDA mode with a cycle time of 3 seconds between master scans. Each master scan was acquired in the Orbitrap at a resolution of 120,000 FWHM (at 200 m/z) and a scan range from 375 to 1600 m/z followed by MS2 scans of the most intense precursors in the Orbitrap at a resolution of 30,000 FWHM (at 200 m/z) with isolation width of the quadrupole set to 1.4 m/z. Maximum ion injection time was set to 50 ms (MS1) and 54 ms (MS2) with an AGC target set to 1e6 and 5e4, respectively. Only peptides with charge state 2 – 5 were included in the analysis. Monoisotopic precursor selection (MIPS) was set to Peptide, and the Intensity Threshold was set to 2.5e4. Peptides were fragmented by HCD (Higher-energy collisional dissociation) with collision energy set to 30%, and one microscan was acquired for each spectrum. The dynamic exclusion duration was set to 30 seconds. The acquired raw-files were imported into the Progenesis QI software (v2.0, Nonlinear Dynamics Limited), which was used to extract peptide precursor ion intensities across all samples applying the default parameters. The generated mgf-file was searched using MASCOT against a murine database (consisting of 34026 forward and reverse protein sequences downloaded from Uniprot on 2019-01-29) and 392 commonly observed contaminants using the following search criteria: full tryptic specificity was required (cleavage after lysine or arginine residues, unless followed by proline); 3 missed cleavages were allowed; carbamidomethylation (C) was set as fixed modification; oxidation (M) and phosphorylation (STY) were applied as variable modifications; mass tolerance of 10 ppm (precursor) and 0.02 Da (fragments). The database search results were filtered using the ion score to set the false discovery rate (FDR) to 1% on the peptide and protein level, respectively, based on the number of reverse protein sequence hits in the datasets. Exported peptide intensities were normalized based on the protein regulations observed in the corresponding TMT experiment in order to account for changes in protein abundance. Only peptides corresponding to proteins, which were regulated significantly with a p value ≤ 1% in the TMT analysis were normalized. Quantitative analysis results from label-free quantification were processed using the SafeQuant R package v.2.3.2 (Ahrne et al., 2016) (https://github.com/eahrne/SafeQuant/) to obtain peptide relative abundances. This analysis included global data normalization by equalizing the total peak/reporter areas across all LC-MS runs, data imputation using the knn algorithm, summation of peak areas per peptide and LC-MS/MS run, followed by calculation of peptide abundance ratios. Only isoform specific peptide ion signals were considered for quantification. The summarized peptide expression values were used for statistical testing of

between condition differentially abundant peptides. Here, empirical Bayes moderated t-Tests were applied, as implemented in the R/Bioconductor limma package were used. All LC-MS analysis runs were acquired from independent biological samples. To meet additional assumptions (normality and homoscedasticity) underlying the use of linear regression models and t-Tests, MS-intensity signals were transformed from the linear to the log-scale. All proteins detected are presented in supplementary table 2. Finally, significantly deregulated were selected by a calculated p-value < 0.01.

Statistical analysis for phosphoprotemics. Using the software Perseus (Tyanova et al., 2016), we performed PCA after Lg2 transformation and subsequent normalization by median subtraction. For the volcano-plot, we used the double sided t-test with 250 randomizations. We set the false discovery rate (FDR) to 0.05 and the S0 value to 0.1 as threshold. To generate hierarchical clustering with z-scored data, we used Spearman correlation for the distance of both trees, leaving the other parameters as default.

Pathway enrichment analysis. Pathway enrichment analysis for proteins with altered phosphorylation sites (p-value < 0.01) between iAdRiKO and control mice was performed by the Database for Annotation, Visualization and Integrated discovery (DAVID) v6.8 (Huang da, Sherman, & Lempicki, 2009) (https://david.ncifcrf.gov/). Settings for DAVID were default. The background list consisted of all proteins detected in the phosphoproteome data set (supplementary table 2). The full analysis can be found in supplementary table 3.

Immunofluorescence staining of WAT sections. Inguinal WATs were fixed overnight in 4% formalin at room temperature, dehydrated, embedded in paraffin, and cut into 5µm thick sections. For immunofluorescence staining, sections were rehydrated and antigen retrieved by boiling sections in target retrieval Solution (Dako) for 20 min in a KOS Microwave HistoSTATION (Milestone Medical). Sections were blocked using Protein block serum-free ready-to-use (Dako) and then incubated in primary antibody diluted in antibody diluent with background reducing component (Dako) overnight at 4°C. Primary antibodies against tyrosine hydroxylase (1:500, Millipore, Cat#AB1542), CGRP (1:200, Enzo, BML-CA1137-0100), GAP43-pS41 (1:200, R&D system, PPS006), Neurofilament heavy polypeptide (1:1000, Abcam, ab8135), Synaptophysin (1:200, Abcam, ab32127) and Adiponectin (1:500, Invitrogen, PA1-054) were used. After washing, sections were incubated in secondary antibody (1:500) in antibody diluent with background reducing component (Dako) for 1 hour

at room temperature. Secondary antibodies against rabbit (Invitrogen, A21070 or A21443), sheep (Invitrogen, A21436) and mouse (Invitrogen, A11004) were used. Finally, sections were stained with NucBlue Live Cell Staining ReadyProbes reagent (Invitrogen, R37605) for 2 min and mounted with VECTASHIELD (Vector, H-1000). Images were obtained using Applied Precision Deltavision CORE system (Leica) and analyzed with OMERO (Allan et al., 2012). For quantification, maximal intensity levels were used.

Whole mount imaging using inguinal WAT depots. Tissues were harvested from mice after intracardiac perfusion with 4% Paraformaldehyde (PFA) and further fixed in 4% PFA overnight at 4 °C. For immunolabeling, tissue clearing and high-resolution volumetric imaging, we developed a modified protocol with the focus on tissue structure and fluorescence preservation. First steps are described by Jingyi Chi et al. 2018 (Chi, Crane, et al., 2018). In short, tissues were washed with PBS, dehydrated using a methanol/B1n buffer (0.3 M Glycine, 0.1% (v/v) Triton-X, pH 7), delipidated using dichloromethane, bleached overnight with 5% H2O2 at 4°C and rehydrated in a reversed methanol/B1n buffer series. For the subsequent immunolabeling tissues were incubated with primary antibodies against TH (1:500, Millipore, Cat#AB1542) and CGRP (1:750, ImmunoSTAR, Cat#24112) diluted in PTxwH buffer (PBS, 0.1% Triton-X (v/v), 0.05% Tween20 (v/v), 2 µg/ml Heparin) and secondary antibodies against sheep (1:500, Invitrogen, A21436 or A21448) and/or rabbit (1:500, Invitrogen, A21070 or A21443). Further tissue clearing was performed using the water-based clearing method Cubic L (Tainaka et al., 2018). Briefly, samples cleared by CUBIC L solution (10% N-butyldiethanolamine (v/v), 10% Triton X-100 (v/v) in ddH_20) followed by 2% agarose embedding and refractive index (RI) matched in CUBIC RA solution (45% antipyrine, 30% N-methylnicotinamide) before imaging. After RI matching Tissue was imaged with the Zen black software (ZEISS) in Cubic RA solution with the RI of 1.51 on a Carl ZEISS lightsheet 7 microscope equipped with the Clr Plan-Neofluar 20x/1.0 detection objective and dual side illuminated with 10x/0.2 objectives. Acquired tiles were loaded in ArivisVision4D (Arivis) for stitching, visualization, and analysis.

CGRP ELISA. Tissues were lysed in PBS using lysis matrix D tubes (MP Biomedicals). CGRP levels in lysates were determined using mouse CGRP ELISA kit (CSB-EQ027706MO, Cusabio) according to manufacturer's instructions.

Denervation surgery. Inguinal fad depots were denervated as described previously (Vaughan, Zarebidaki, Ehlen, & Bartness, 2014) in eight-week-old mice. For surgical denervation, mice were anaesthetized and incisions were made dorsally on the flank. Nerves innervating inguinal WAT were identified using a dissection microscope, cut several times and removed. For sham operation, mice were anaesthetized and incisions were made dorsally on the flank. Mice were allowed to recover after surgery and were sacrificed four weeks after surgery.

Statistics. Sample size was chosen according to our previous studies and published reports in which similar experimental procedures were described. The investigators were not blinded to the treatment groups. All data are shown as the mean ± SD. Sample numbers are indicated in each figure legend. For mouse experiments, *n* represents the number of animals, and for imaging, *N* indicates the number of images acquired per experiment. To determine the statistical significance between two groups, an unpaired two-tailed Student's t-test was performed. For ITT, two-way ANOVA was performed. All statistical analyses were performed using GraphPad Prism 9 (GraphPad Software, San Diego, California). A p value of less than 0.05 was considered statistically significant.

Acknowledgements

We thank Sara Merino and Kai Schleicher (Imaging Core Facility, Biozentrum, Basel) for technical support, and Stefan Offermanns for providing *Adipoq promoter*-CreER^{T2} mice. We also thank Christoph Handschin, Bernhard Thorens, Markus Rüegg and Frédéric Preitner for helpful discussions. We acknowledge support from the Swiss National Science Foundation (project 179569 to MNH and 161510 to MS), The Louis Jeantet Foundation (MNH), and the Canton of Basel (MNH).

Author contributions

ICF, MS, and MNH designed the project and the experiments. ICF, DW and MS conducted the experiments with contributions from DR (proteomics), MC (proteomic analysis) and WH (clearing method). ICF, MS and MNH wrote the manuscript.

3.1.6. Figures

Figure 1

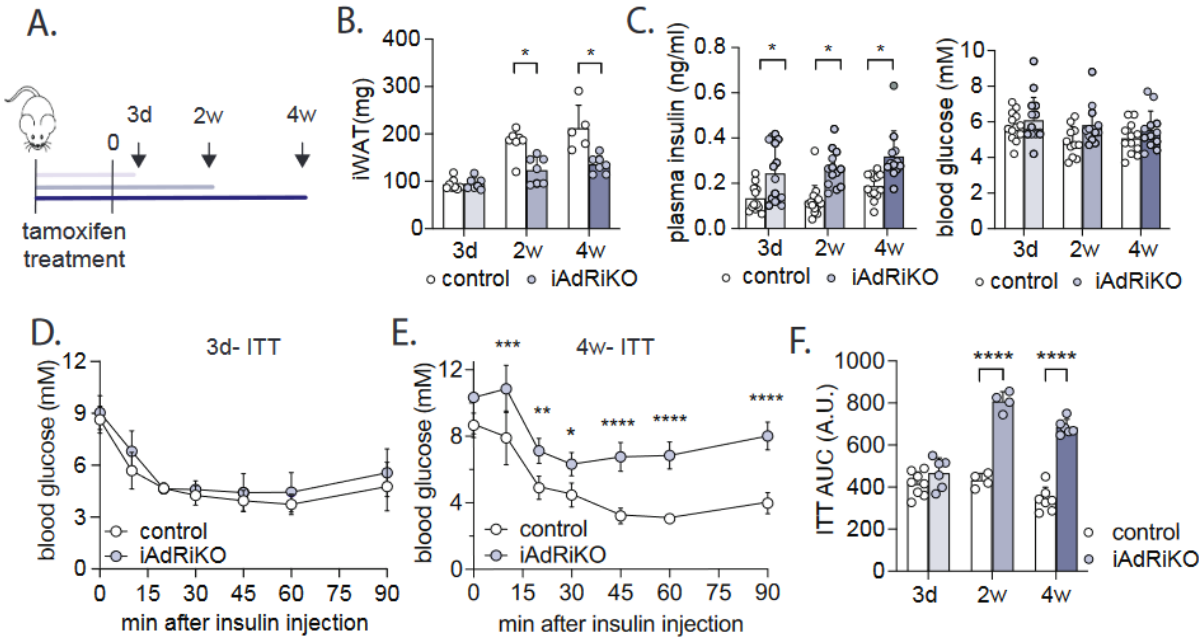

Figure 1. Loss of adipose mTORC2 acutely impairs whole-body energy homeostasis
(A) Experimental design of the longitudinal studies.
(B) Tissue weight of inguinal iWAT (iWAT) in *ad libitum*-fed control and iAdRiKO mice three days (n= 8;7), two (n=7), and four weeks (n= 5;7) after tamoxifen treatment. Student's t-test, *p<0.05.
(C) Plasma insulin and blood glucose levels of control and iAdRiKO mice after 16 hours starvation three days (n=13;15), two (15;13), and four weeks (13;12) after tamoxifen treatment. Student's t-test, *p<0.05.
(D) Insulin tolerance test (ITT) on control and iAdRiKO mice three days after tamoxifen treatment (n= 5;8).
(E) ITT on control and iAdRiKO mice four weeks after tamoxifen treatment (n=5;6). 2-way ANOVA, *p<0.05, **p<0.01, ***p<0.001, **** p<0.0001.
(F) Area under the curve (AUC) for ITT on control and iAdRiKO mice three days (n= 5;8), two (n= 4), and four weeks (n= 5;6) after tamoxifen treatment. Student's t-test, **** p<0.0001.

Figure 2

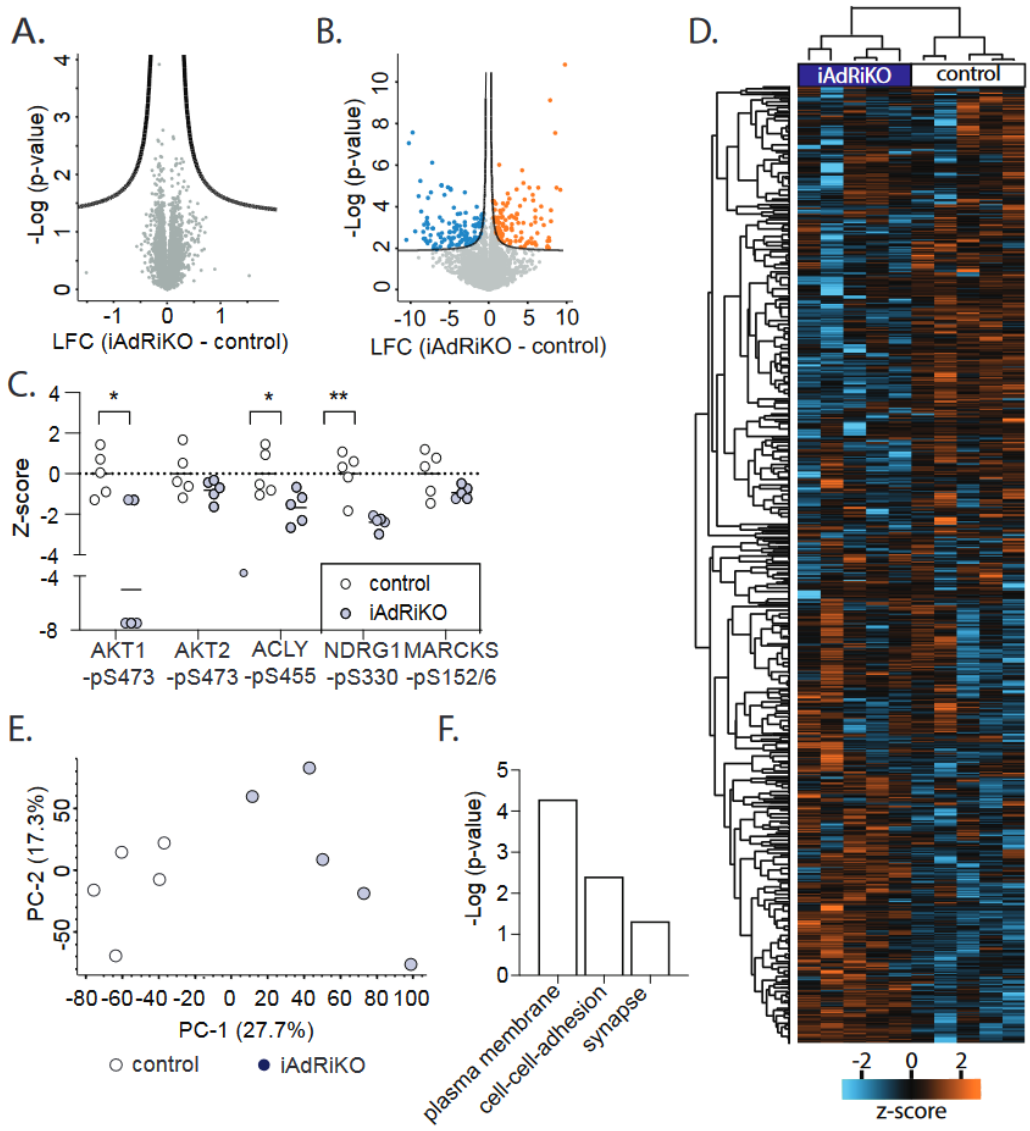

Figure 2. Loss of mTORC2 alters proteins associated with synapse formation in WAT
(A) Volcano-plot displaying the comparison of proteins derived from inguinal WAT (iWAT) of control and iAdRiKO mice at three days after tamoxifen treatment (n=5). LFC= Log_2 fold change.
(B) Volcano-plot displaying the comparison of phosphosites derived from iWAT of control and iAdRiKO mice three days after tamoxifen treatment (n= 5). LFC= Log_2 fold change.
(C) Z-scores of mTORC2-regulated phosphosites in iWAT three days after tamoxifen treatment (n= 5). Student's t-test, *p<0.05, **p<0.01.
(D) Unsupervised hierarchical clustering using Euclidian distance of the phosphoproteome data set (n=5).
(E) Principal component analysis (PCA) for iWAT-derived phosphoproteome of control and iAdRiKO mice three days after tamoxifen treatment (n=5).
(F) Pathway enrichment analysis of phosphoproteins altered in iWAT of iAdRiKO mice compared to control mice analyzed and visualized by the Database for Annotation, Visualization and Integrated Discovery (DAVID).

Figure 3

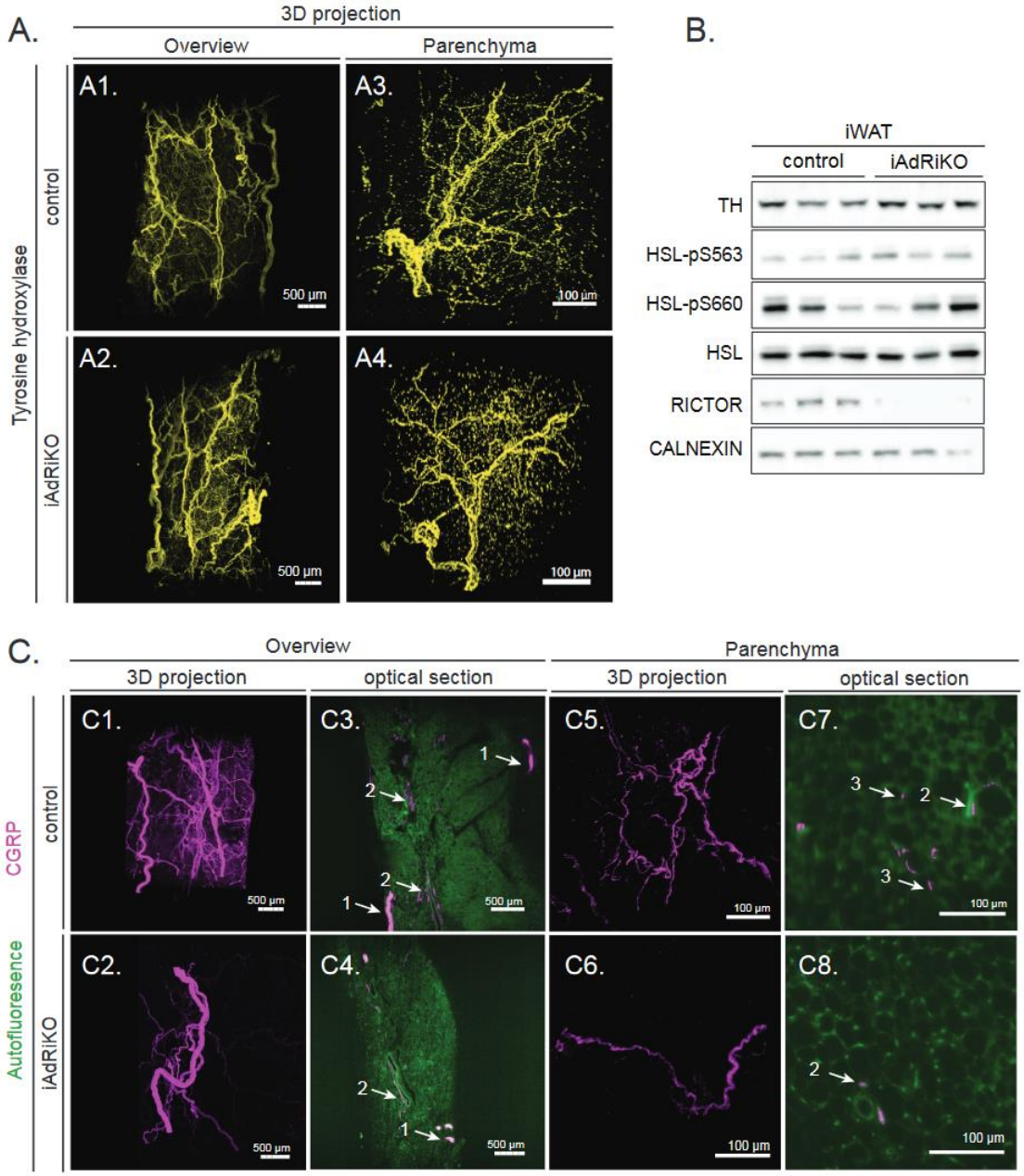
A.
3D projection
Overview
Parenchyma
Tyrosine hydroxylase
control
iAdRiKO
A1.
A2.
A3.
A4.
500 µm
100 µm
B.
iWAT
control
iAdRiKO
TH
HSL-pS563
HSL-pS660
HSL
RICTOR
CALNEXIN
C.
Overview
Parenchyma
3D projection
optical section
3D projection
optical section
CGRP
Autofluoresence
control
iAdRiKO
C1.
C2.
C3.
C4.
C5.
C6.
C7.
C8.
500 µm
100 µm

Figure 3. Sensory but not sympathetic innervation is altered upon loss of adipose mTORC2

(A) 2D representatives of a 3D reconstruction of inguinal WAT (iWAT) four weeks after tamoxifen treatment immunostained with tyrosine hydroxylase (TH; yellow).
(A1-2) Low magnification projection of sympathetic neuronal network in control and iAdRiKO mice (N=4;5). Scale bar= 500 μm.
(A3-4) High magnification projection of sympathetic neurons in iWAT parenchyma of control mice and iAdRiKO (N=19;10). Scale bar= 100 μm.
(B) Immunoblot analysis of iWAT from control and iAdRiKO mice four weeks after tamoxifen treatment. Hormone-sensitive lipase (HSL). (n=6;6).
(C) 2D representatives of a 3D reconstruction of iWAT four weeks after tamoxifen treatment immunostained with calcitonin gene-related peptide (CGRP; magenta).
(C1-2) Low magnification projection of sensory neuronal network in control and iAdRiKO mice (N=12;19). Scale bar= 500 μm.
(C3-4) Low magnification cross section of sensory neuronal network in control and iAdRiKO mice (N=12;19). Nerve bundle (1), innervation along blood vessel (2), tissue autofluorescence (green). Scale bar= 500 μm.
(C5-6) High magnification projection of sensory neurons in iWAT parenchyma of control mice and iAdRiKO (N=16;11). Scale bar= 100 μm.
(C7-8) High magnification cross section of neurons in control and iAdRiKO mice (N=16;11). Innervation along blood vessel (2), parenchymal innervation (3), tissue autofluorescence (green). Scale bar= 100 μm.

Figure 4

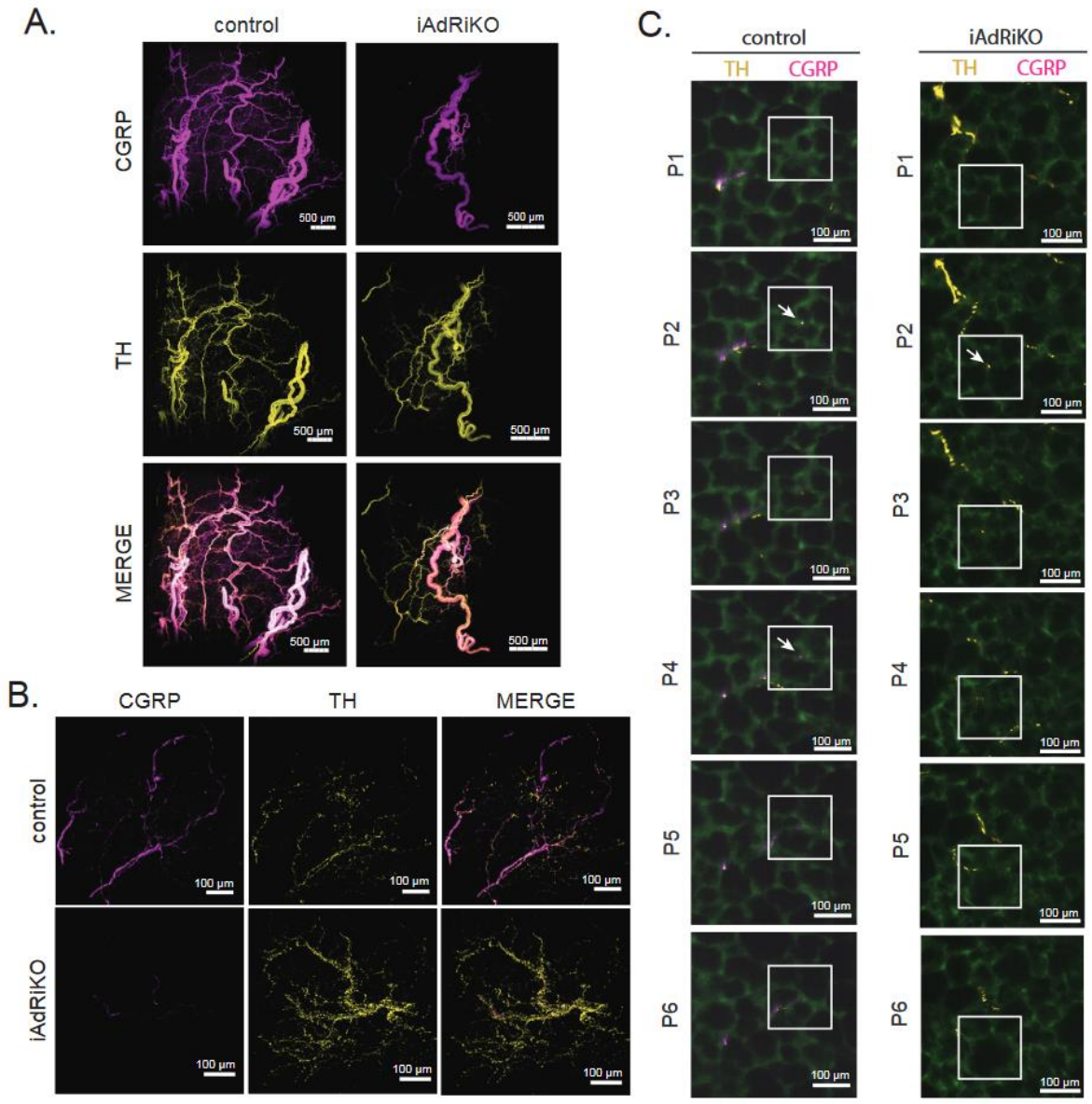

Figure 4. Loss of adipose mTORC2 reduces arborization of sensory neurons
(A) Low magnification projection of inguinal WAT (iWAT) four weeks after tamoxifen treatment co-immunostained with tyrosine hydroxylase (TH, yellow) and calcitonin gene-related peptide (CGRP, magenta) (N=15;18). Scale bar= 500 µm.
(B) High magnification projection of iWAT four weeks after tamoxifen treatment co-immunostained with TH (yellow) and CGRP (magenta) (N=21;22). Scale bar= 500 µm.
(C) Subsequent sections (P1-P6; 6.48/6.28 µm interval, respectively) of control and iAdRiKO iWAT immunostained with TH (yellow) and CGRP (magenta) illustrating single nerve fibers innervating the periphery. Region of interest: Nerve ending and potential synapses (arrows). Tissue autofluorescence= green. Scale bar= 100 µm.

Figure 5

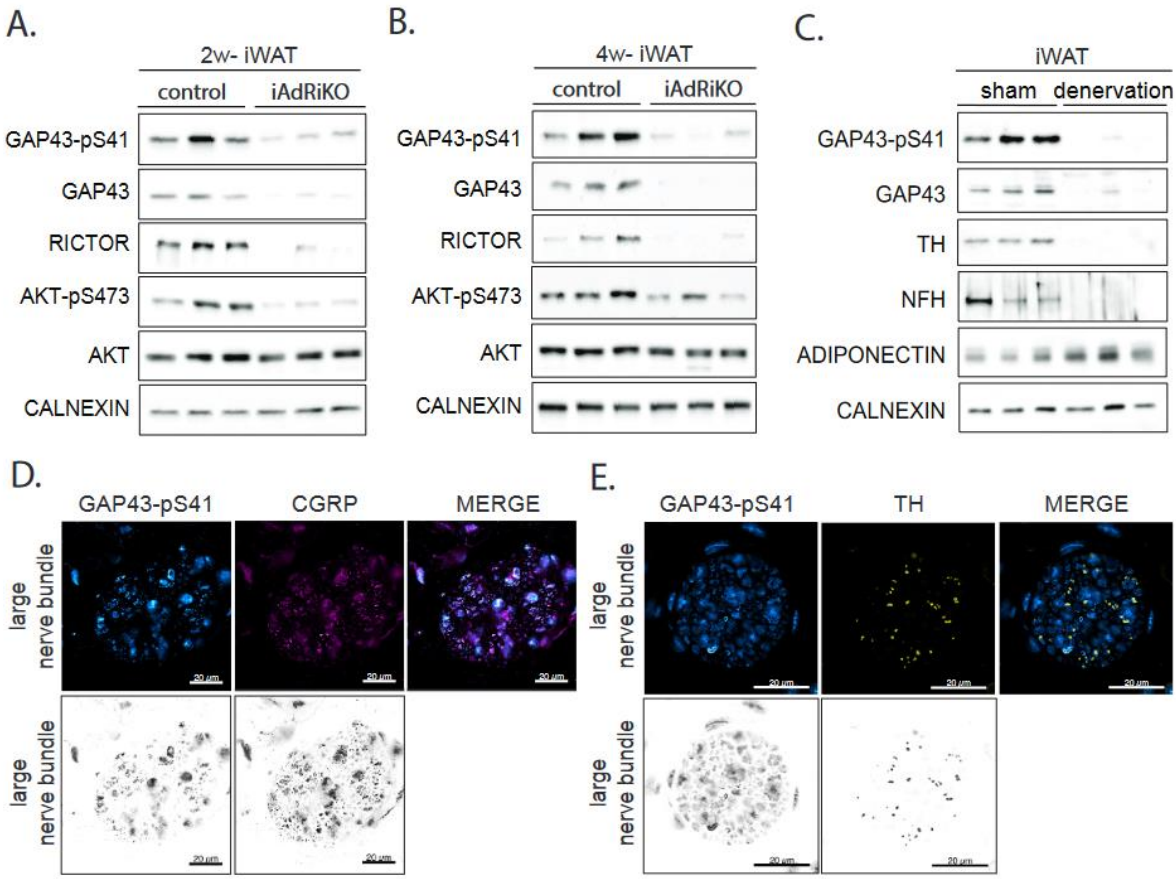

Figure 5. GAP43 expression is downregulated in CGRP-positive neurons upon loss of adipose mTORC2

(A) Immunoblot analysis of inguinal WAT (iWAT) tissue from control and iAdRiKO mice two weeks after tamoxifen treatment. (n=6;6).

(B) Immunoblot analysis of iWAT tissue from control and iAdRiKO mice four weeks after tamoxifen treatment. (n=6;6).

(C) Immunoblot analysis of surgically denervated iWAT depot (denervation) compared to iWAT depot from sham-operated mice (sham). Neurofilament heavy polypeptide (NFH). (n=5;5).

(D) Representative image of a large nerve bundle in iWAT of control mice immunostained with growth-associated protein 43 (GAP43)-pS41 and calcitonin gene-related peptide (CGRP). (N=11;9).

(E) Representative image of a large nerve bundle in iWAT of control mice immunostained with GAP43-pS41 and tyrosine hydroxylase (TH). (N=19;11).

3.1.7. Supplementary Figures

Supplementary Figure 1

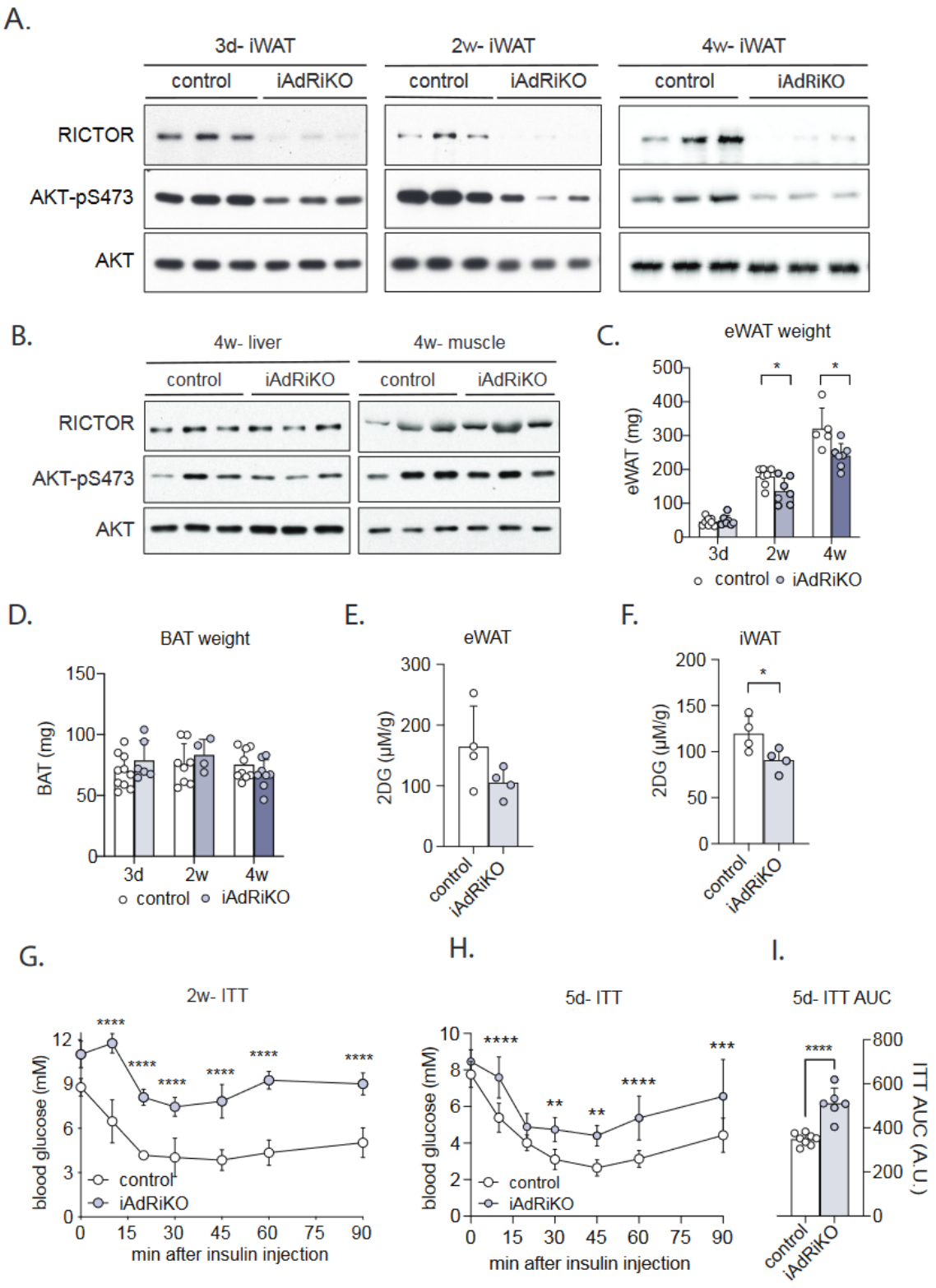

Supplementary Figure 1.
(A) Immunoblot analysis of inguinal WAT (iWAT) from control and iAdRiKO mice three days, two, and four weeks after tamoxifen treatment (n=6;6).
(B) Immunoblot analysis of liver and muscle tissue from control and iAdRiKO mice four weeks after tamoxifen treatment (n=6;6).
(C) Tissue weight of epididymal WAT (eWAT) in *ad libidum*-fed control and iAdRiKO mice three days (n=8;7), two (n=7), and four weeks (n=5;7) after tamoxifen treatment. Student's t-test, *p<0.05.
(D) Tissue weight of brown adipose tissue (BAT) in *ad libidum*-fed control and iAdRiKO mice at three days (n=10;6), two (n=8;4) and four (n=9;8) weeks after tamoxifen treatment.
(E) 2- deoxyglucose (2DG) uptake in eWAT of control and iAdRiKO mice three days after tamoxifen treatment (n=4).
(F) 2DG uptake in iWAT of control and iAdRiKO mice three days after tamoxifen treatment (n=4). Student's t-test, *p<0.05.
(G) Insulin tolerance test (ITT) on control and iAdRiKO mice two weeks after tamoxifen treatment (n=4). 2-way ANOVA, **** p<0.0001.
(H) ITT on control and iAdRiKO mice five days after tamoxifen treatment (n=8;6). 2-way ANOVA, **p<0.01, ***p<0.001, **** p<0.0001.
(I) Area under the curve (AUC) for ITT on control and iAdRiKO mice five days after tamoxifen treatment (n=8;6). Student's t-test, **** p<0.0001.

Supplementary Figure 2

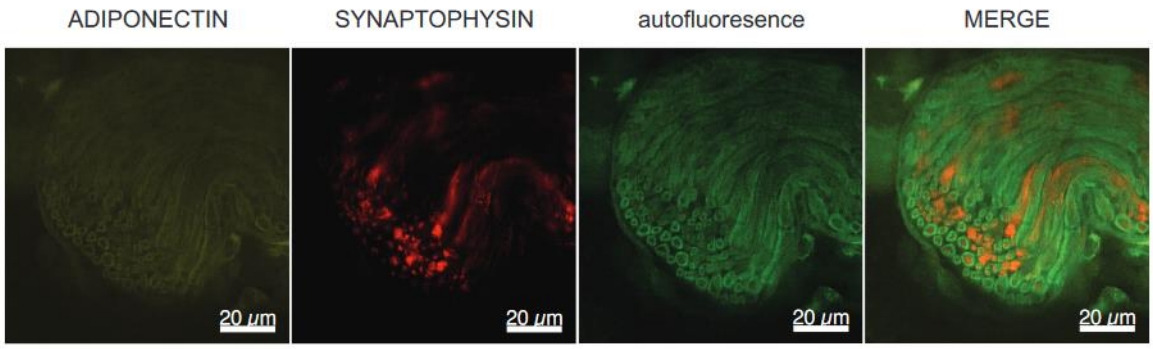

Supplementary Figure 2.
(A) Representative image of large nerve bundles in control iWAT immunostained for both ADIPONECTIN and SYNAPTOPHYSIN (N=4). Scale bar= 20 µm.

Supplementary Figure 3

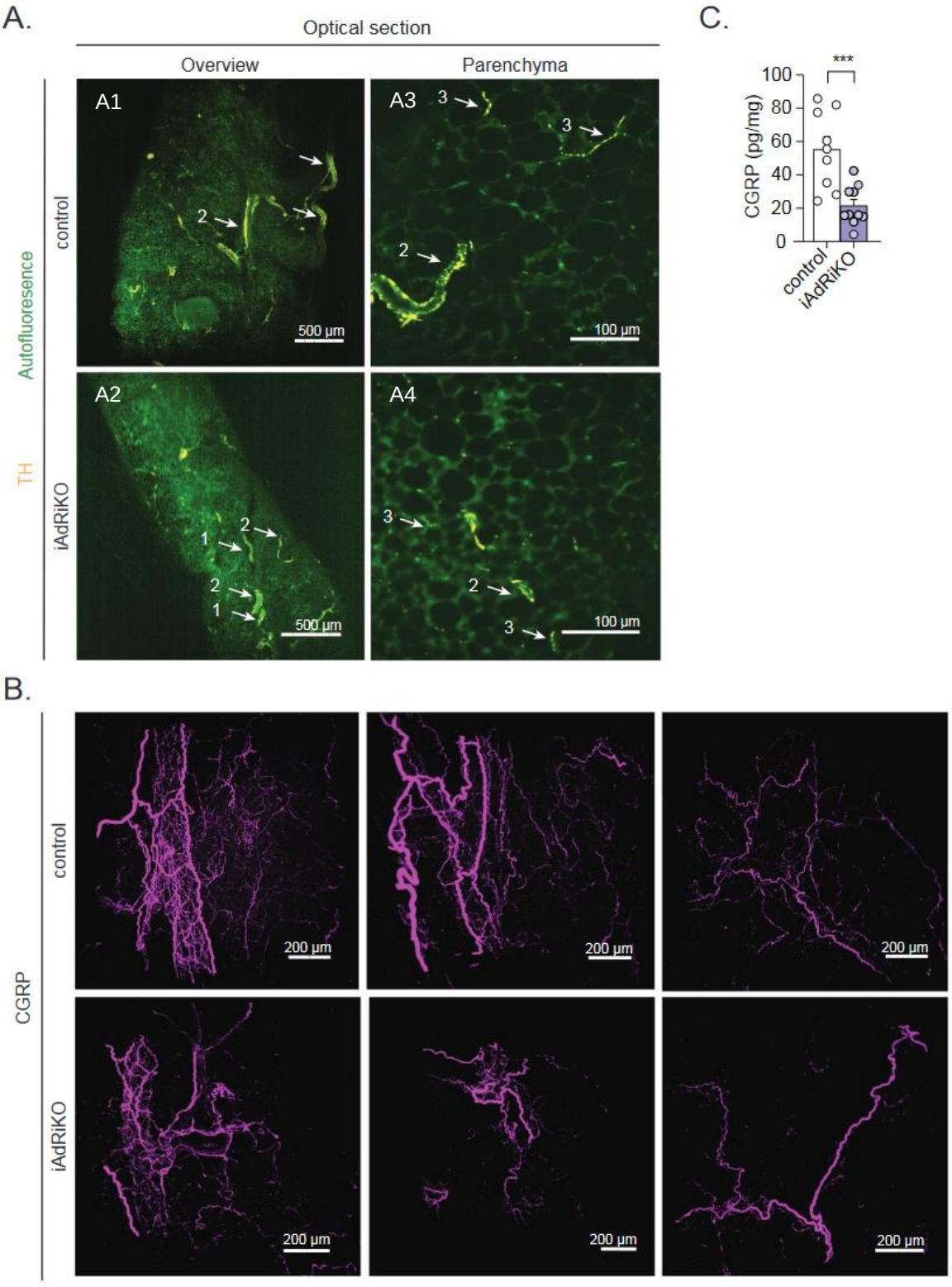

Supplementary Figure 3.
(A) Crosssections of inguinal WAT (iWAT) four weeks after tamoxifen treatment immunostained with tyrosine hydroxylase (TH; yellow).
(A1-2) Low magnification cross sections of sympathetic neuronal network in control and iAdRiKO mice (N=**4;5**). Nerve bundle (1), innervation around blood vessel (2), tissue autofluorescence (green). Scale bar= 500 μm.
(A3-4) High magnification cross section of sympathetic neurons in iWAT parenchyma of control and iAdRiKO mice (N=19;10). Scale bar= 100 μm.
(B) High magnification projections of calcitonin gene-related peptide (CGRP)-positive sensory neurons (magenta) in iWAT of different control and iAdRiKO mice. Scale bar= 200 μm. (N=13;8, n=3;3).
(C) Enzyme-linked immunosorbent assay (ELISA) for CGRP levels in iWAT of control and iAdRiKO mice (n=9). Student's t-test, ***$p<0.001$.

Supplementary Figure 4

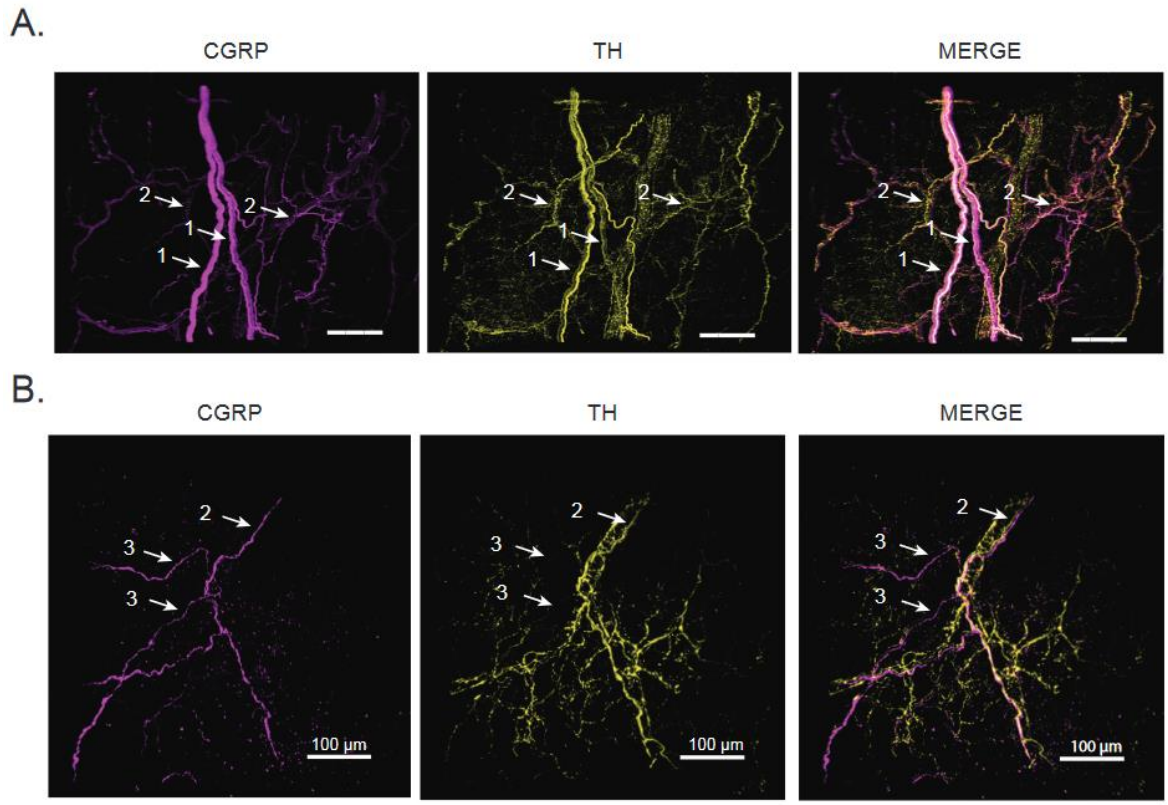

Supplementary Figure 4.
(A) 2D representative of a 3D reconstruction of an inguinal WAT (iWAT) section immunostained with calcitonin gene-related peptide (CGRP, magenta) and the tyrosine hydroxylase (TH, yellow) that illustrates how a large nerve bundle subdivides into smaller nerve bundles which in turn penetrate the tissue alongside blood vessels. Nerve bundle (1), innervation along blood vessel (2). Scale bar= 300 µm.
(B) 2D representative of a 3D reconstruction of the iWAT parenchyma of both CGRP-positive (magenta) and the TH-positive (yellow) neuronal networks in iWAT. Innervation along blood vessel (2), parenchymal innervation (3). Scale bar= 100 µm.

Supplementary Figure 5

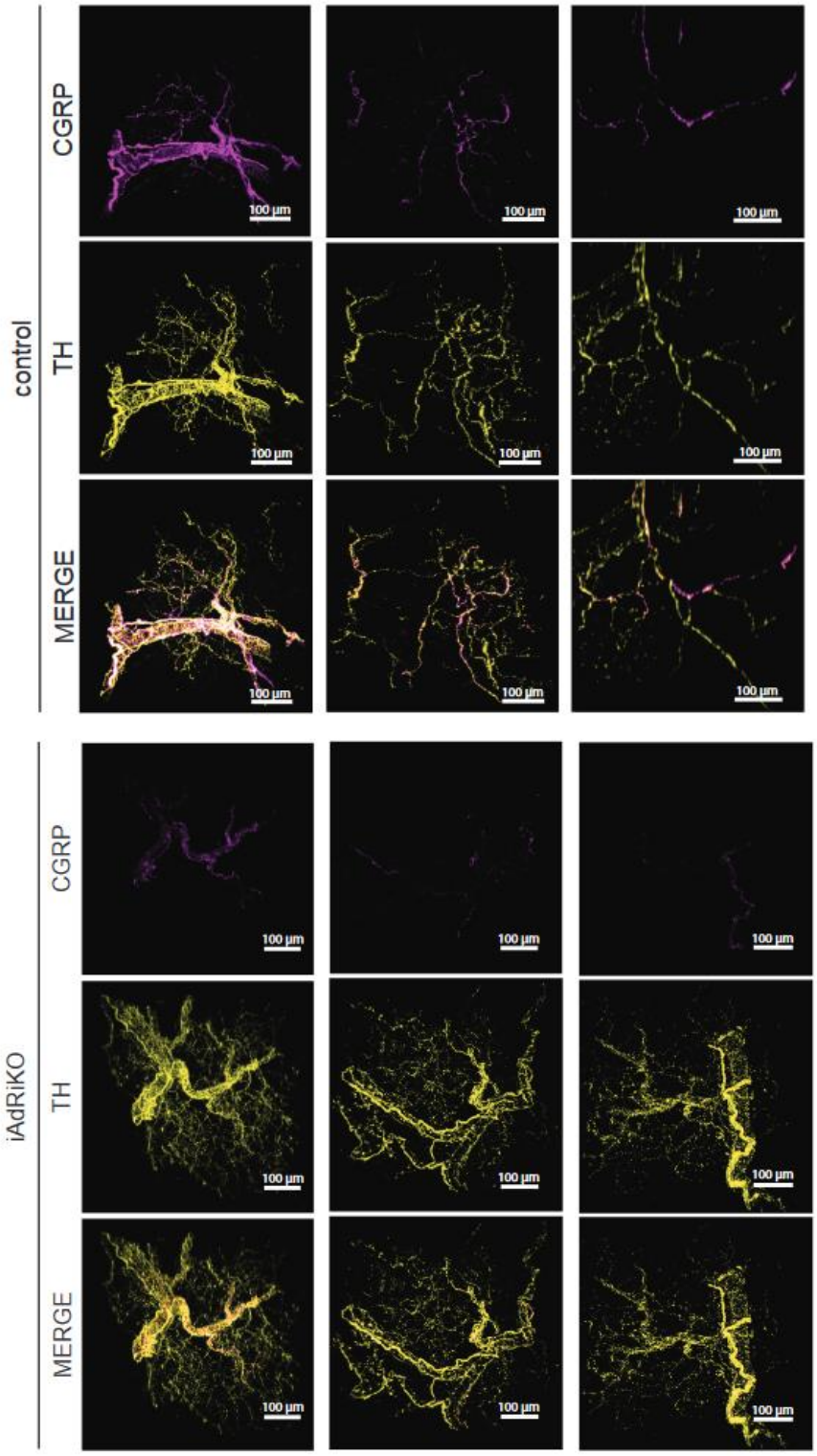

Supplementary Figure 5.
2D representative of a 3D reconstruction of inguinal WAT sections from control and iAdRiKO mice immunostained with calcitonin gene-related peptide (CGRP; magenta) and tyrosine hydroxylase (TH; yellow) (N=21;22). Scale bar= 100 µm.

Supplementary Figure 6

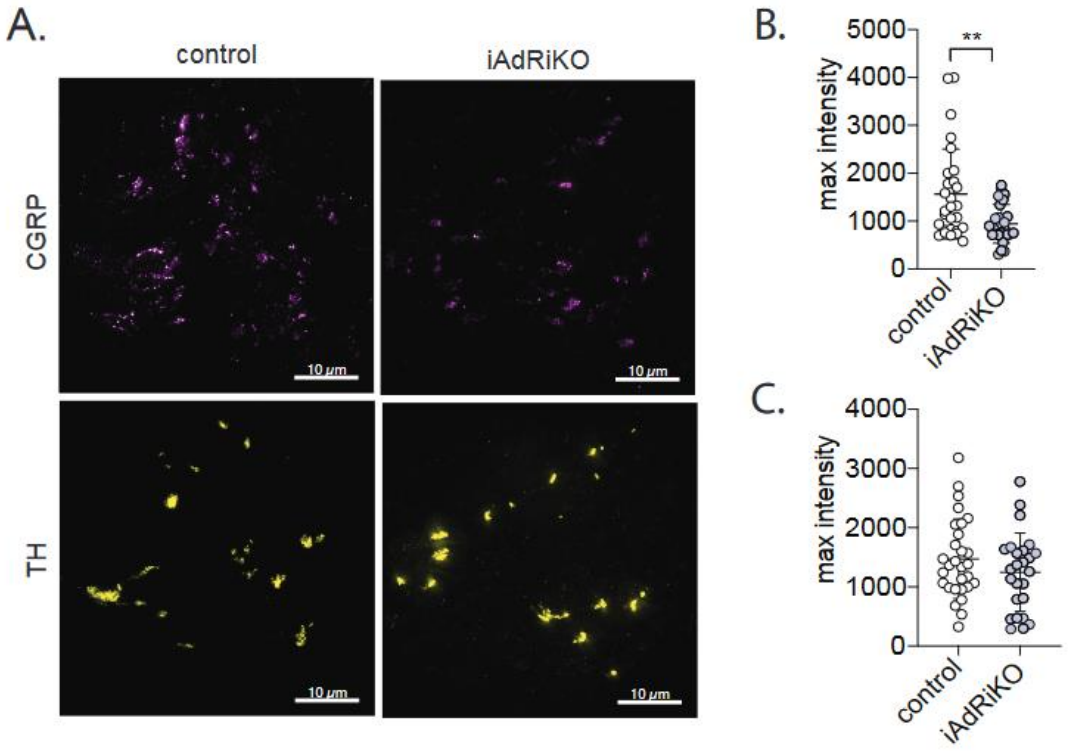

Supplementary Figure 6.
(A) Representative image of a large nerve bundle in control and iAdRiKO iWAT paraffine sections immunostained with CGRP (magenta) and tyrosine hydroxylase (TH, yellow) (N= 29;25). Scale bar= 10 µm.
(B) Quantification of maximal intensity of CGRP-immunostaining in large nerve bundles of iWAT of control and iAdRiKO mice (N= 29;25). Student's t-test, **p<0.01.
(C) Quantification of maximal intensity of TH-immunostaining in large nerve bundles of iWAT of control and iAdRiKO mice (N= 29;25). Student's t-test, **p<0.01.

3.2 Manuscript 2:

Adipose and hepatic mTORC2 promote energy storage and maintains glucose homeostasis

Irina C. Frei[1], Diana Weissenberger[1], Michael N. Hall[1]*, Mitsugu Shimobayashi[1,2]*

[1] Biozentrum, University of Basel, Basel 4056, Switzerland

[2] Laboratory of Clinical and Experimental Endocrinology, Department of Chronic Diseases and Metabolism, KU Leuven, Leuven 3000, Belgium

[*] Corresponding authors:

e-mail: m.hall@unibas.ch (MNH) and mitsugu.shimobayashi@kuleuven.be (MS)

3.2.1. Abstract

mTORC2 is a protein kinase complex that plays an important role in energy homeostasis. It has been demonstrated that loss of adipose mTORC2 in mice reduces lipogenic enzyme expression and DNL in adipose tissue and increases triglyceride accumulation in the liver. However, the underlying mechanism and the physiological role of hepatic triglyceride accumulation upon loss of adipose mTORC2 are unknown. In this study, we show that loss of adipose mTORC2 increases expression of *de novo* lipogenic enzymes in the liver thereby causing hypertriglyceridemia and non-alcoholic fatty liver disease. Loss of lipogenic enzymes in adipose tissue and liver by simultaneous ablation of mTORC2 prevents the accumulation of triglycerides in the liver, but instead causes severe insulin resistance and glucose intolerance in mice. Thus, our findings suggest that increased hepatic lipogenesis is a compensatory mechanism to cope with the loss of mTORC2 and lipogenesis in adipose tissue and further suggest that mTORC2 in adipose tissue and liver plays a crucial role in maintaining whole-body energy homeostasis.

3.2.2. Introduction

Organisms adapt their metabolism in response to nutrient availability. Under nutrition rich conditions, excess energy is stored in WAT in the form of TG (Rosen & Spiegelman, 2006). The importance of WAT is well documented in studies of patients with lipodystrophy, which fail to store a surplus of energy in WAT due to impaired WAT function (Lim, Haider, Adams, Sleigh, & Savage, 2021). Although most patients with lipodystrophy appear lean, they develop similar symptoms to patients with obesity, such as cardiovascular diseases, type II diabetes, NAFLD, and hypertriglyceridemia. Thus, it is important to study the consequences of impaired WAT function on whole-body energy homeostasis to counteract these adverse effects.

A major regulator of energy storage is the hormone insulin that promotes energy uptake and storage upon nutrition intake. WAT is able to import different circulating energy carriers, most noteworthy FFAs and glucose. Once imported into the cell, FFA are esterified and stored as TGs. Glucose is imported upon insulin stimulation and converted into FFAs and TGs by a metabolic process called DNL. One of the major kinases regulating insulin-stimulated glucose uptake and DNL is mTORC2 (Hsiao et al., 2020; Tang et al., 2016). mTORC2 is a serine/threonine kinase complex, which consists of core components including the kinase mTOR and RICTOR (Jacinto et al., 2004; Loewith et al., 2002; Sarbassov et al., 2004). The physiological role of mTORC2 in adipocytes has been studied *in vivo* by

characterizing conditional *Rictor* knockout mice (Cybulski et al., 2009; Kumar et al., 2010; Tang et al., 2016; Yu et al., 2019). It has been demonstrated that loss of adipose mTORC2 impairs the expression of genes encoding key lipogenic enzymes including FASN and ACC and thus DNL (Hsiao et al., 2020; Tang et al., 2016). Mice lacking mTORC2 in WAT develop hyperinsulinemia, systemic insulin resistance and accumulation of TGs in liver (Cybulski et al., 2009; Tang et al., 2016; Yu et al., 2019). Surprisingly, these mice remain glucose tolerant, suggesting a compensatory mechanism that counteracts the reduced storage capacity of WAT lacking mTORC2.

In the liver, mTORC2 also promotes DNL (Hagiwara et al., 2012). Similar to WAT, loss of hepatic mTORC2 reduces the expression of the lipogenic enzymes FASN and ACC and prevents hepatic TG accumulation. Mice lacking hepatic mTORC2 develop glucose intolerance and mild insulin resistance (Hagiwara et al., 2012) indicating that hepatic mTORC2 is important to maintain whole-body energy homeostasis.

In this study, we show that the acute loss of mTORC2 in mature adipocytes causes mild lipodystrophy due to impaired glucose uptake and expression of lipogenic enzymes. We found that hepatic DNL is upregulated upon loss of adipose mTORC2 and observed accumulation of TGs in the liver and the plasma. We hypothesized that the increase in hepatic DNL and TG accumulation is to compensate for impaired WAT function. Accordingly, simultaneous deletion of mTORC2 in both adipose tissue and liver blocked the expression of DNL enzymes in both organs and prevented TG accumulation in the liver and the plasma. However, mice lacking both adipose and hepatic mTORC2 develop severe insulin resistance and glucose intolerance. Thus, our findings suggest that the increased hepatic DNL upon loss of adipose mTORC2 is a physiological response to compensate for impaired energy storge in WAT.

3.2.3. Results

Loss of mTORC2 in adult mice causes mild lipodystrophy. Previous studies have shown that mice lacking adipose mTORC2 from birth display impaired glucose uptake and reduced expression of lipogenic enzymes including ACC and FASN in WAT (Hsiao et al., 2020; Tang et al., 2016). However, adipose tissue is not fully developed until six weeks of age and thus impaired glucose uptake and DNL could be due to a developmental defect. To probe the role of mTORC2 in mature adipocytes, we characterized inducible adipose-specific *Rictor* knockout mice (*Rictor*$^{fl/fl}$, *Adipoq-CreER*^{T2}). *Rictor* deletion was induced in six- to eight-week-old mice by tamoxifen injections and we confirmed loss of RICTOR and mTORC2

activity by immunoblot (**Figure 1A-B**). Next, we tested the expression of lipogenic enzymes such as ACC and FASN in WAT. Consistent with previous studies (Hsiao et al., 2020; Tang et al., 2016), ACC and FASN expression were downregulated in WAT of iAdRiKO compared to control littermates indicating reduced DNL (**Figure 1A-B**). To test whether loss of adipose mTORC2 in mature adipocytes also reduces glucose uptake, we performed a 2-deoxy glucose (2DG) uptake assay. Glucose uptake was reduced ~ 70% in WAT of iAdRiKO mice, compared to controls (**Figures 1C and S1A**). These findings suggest that mTORC2 directly promotes both glucose uptake and the expression of lipogenic enzymes in mature adipocytes. Next, we examined if reduced glucose uptake and DNL in WAT had an impact on body composition. Similar to mice lacking adipose mTORC2 from birth (Cybulski et al., 2009; Tang et al., 2016; Yu et al., 2019), body weight of iAdRiKO mice was normal (**Figure S1B**). However, body composition analysis revealed a ~ 25% reduction in fat mass in iAdRiKO mice compared to controls and a corresponding increase in lean mass (**Figure 1D**). Further analysis revealed a reduction in the weights of epididymal and inguinal WAT depots, but not in BAT (**Figure 1E**). Taken together, our findings suggest that loss of mTORC2 in mature adipocytes causes mild lipodystrophy due to impaired glucose uptake and DNL in WAT.

Loss of adipose mTORC2 in adult mice causes increased hepatic lipogenesis. Despite the reduced glucose uptake in WAT, iAdRiKO mice remained glucose tolerant (**Figure S1C**). Thus, we hypothesized that impaired glucose uptake in WAT is compensated by another organ. Similar to other studies (Tang et al., 2016; Yu et al., 2019), we found that iAdRiKO mice displayed increased liver weight while other organs were unaffected (**Figures 2A and S1D**). Histological analyses revealed an increase in the number of lipid droplets in the liver of iAdRiKO mice compared to controls (**Figure 2B**). Accumulation of hepatic TG was also confirmed by biochemical measurements, although the difference did not reach statistical significance (**Figure 2C**). Based on these observations, we hypothesized that impaired glucose uptake in WAT is compensated by hepatic DNL. Indeed, we found increased expression of FASN and ACC in the liver of iAdRiKO compared to controls (**Figures 2D-E**). Normally, the liver secretes *de novo* synthesized TGs to be stored in WAT. Interestingly, plasma TG levels were significantly higher in iAdRiKO mice compared to controls (**Figure 2F**). These data suggest that acute loss of adipose mTORC2 increases hepatic DNL as a compensatory mechanism for impaired glucose uptake and DNL in adipocytes.

Compensatory increase in hepatic DNL upon impaired WAT function is diminished upon loss of hepatic mTORC2. Next, we investigated the significance of the compensatory increase in hepatic DNL upon loss of adipose mTORC2. Since mTORC2 promotes the expression of FASN and ACC in both the liver and adipose tissue (Hagiwara et al., 2012; Tang et al., 2016), we generated adipose- and liver-specific double *Rictor* knockout mice (dRiKO: *Adipoq-CreER^{T2}, Alb-Cre, Rictor$^{fl/fl}$*) by crossing iAdRiKO with liver-specific *Rictor* knockout mice (*Alb-Cre; Rictor$^{fl/fl}$*). No differences in body weight were observed in dRiKO mice compared to iAdRiKO, LiRiKO, and control mice (**Figure S2A**). Similar to iAdRiKO mice, dRiKO mice displayed decreased fat mass due to smaller WAT depots (**Figures 3A-D**). Histological analyses of WAT revealed a reduction of adipocyte diameter in WAT of both iAdRiKO and dRiKO mice indicating mild lipodystrophy (**Figures 3E-F**). Next, we examined glucose uptake and DNL in WAT. We found that both iAdRiKO and dRiKO mice displayed reduced glucose uptake in WAT, compared to controls (**Figures 3G**). Glucose uptake was also slightly decreased in WAT of LiRiKO mice, although this difference did not reach statistical significance (**Figures 3G**). In contrast, hepatic mTORC2 ablation increases the expression of lipogenic enzymes such as ACC and FASN, although the differences did not reach statistical significance (**Figures H and S2B**). Next, we examined the effect of hepatic mTORC2 ablation on TG accumulation in the liver. As expected, liver weight of dRiKO mice was smaller than control and iAdRiKO mice (**Figure 4A**). Histological and biochemical analyses confirmed a reduction of hepatic and plasma TG in dRiKO mice compared to iAdRiKO and control mice (**Figures 4B-C**). To examine whether the reduction of hepatic and plasma TG was due to decreased expression of lipogenic enzymes in the liver, we analyzed hepatic FASN and ACC expression. We found that loss of hepatic mTORC2 reduces FASN and ACC expression in the liver of both LiRiKO and dRiKO mice (**Figures 4D-4E**). These data suggest that hepatic mTORC2 is required for the compensatory increase in DNL upon impaired WAT function.

Simultaneous loss of adipose and hepatic mTORC2 causes severe insulin resistance and glucose intolerance. Next, we investigated the loss of adipose and hepatic mTORC2 on whole body energy homeostasis. Fasting plasma insulin and glucose level were both significantly increased in dRiKO mice compared to control mice (**Figures 5A-B**). Since glucose is the major source for DNL in both adipose tissue and liver, we assessed whole body glucose homeostasis by performing a glucose tolerance test. As previously reported, LiRiKO mice were slightly glucose intolerant (Hagiwara et al., 2012) while iAdRiKO and control mice

were glucose tolerant (**Figures 5C-D**). In contrast, dRiKO mice displayed severe glucose intolerance (**Figures 5C-D**). Next, we performed an insulin tolerance test to determine systemic insulin sensitivity. Consistent with previous studies (Cybulski et al., 2009; Hagiwara et al., 2012; Kumar et al., 2010; Tang et al., 2016), iAdRiKO and LiRiKO mice were insulin resistant compared to control mice (**Figures 5E-F**). We found that dRiKO mice display severe insulin resistance, the severity of which is synergistic to the effect detected in iAdRiKO and LiRiKO mice (**Figures 5E-F**). Taken together, our findings show that adipose and liver mTORC2 are indispensable to maintain whole body energy homeostasis and that simultaneous loss of both hepatic and WAT mTORC2 signaling has a synergistic effect on the severity of systemic insulin resistance and glucose intolerance.

3.2.4. Discussion

In this study, we highlight the physiological importance of both adipose and hepatic mTORC2 in maintaining whole body lipid and glucose homeostasis. Loss of mTORC2 in mature adipocytes impairs adipose DNL, causes mild lipodystrophy and increases hepatic TG accumulation and DNL. We show that blocking hepatic TG accumulation and DNL in presence of impaired WAT function has detrimental effects on whole-body energy homeostasis, causing severe insulin resistance and glucose intolerance. Thus, our findings suggest that increased hepatic TG accumulation and DNL in mice with impaired WAT function is an important physiological response to compensate for impaired TG storage in WAT.

AKT is the best characterized mTORC2 substrate. Previously, it was reported that loss of adipose AKT1 and AKT2 causes severe lipodystrophy and hepatic TG accumulation (Shearin, Monks, Seale, & Birnbaum, 2016). Adipose-specific AKT1 and AKT2 knockout (Adipo-AKT KO) mice were insulin resistant but glucose tolerant. However, it is unknown why Adipo-AKT KO mice remain glucose tolerant. Similar to Adipo-AKT KO mice, we show that mice lacking adipose mTORC2 displayed lipodystrophy, hepatic TG accumulation and systemic insulin resistance but remained glucose tolerant. We show that the accumulation of hepatic TGs in mice lacking adipose mTORC2 is due to an increased expression of lipogenic enzymes in the liver. Blocking hepatic DNL and TG accumulation in presence of impaired WAT function caused severe glucose intolerance, suggesting that increased hepatic DNL and TG accumulation in iAdRiKO mice is a compensatory mechanism to sustain glucose homeostasis. Considering that AKT 1 and AKT2 are mTORC2 substrates, our findings suggest that TG accumulation observed in Adipo-AKT KO mice may also be a mechanism to compensate for impaired WAT function to maintain whole-body glucose homeostasis.

While mice lacking adipose mTORC2 from birth displayed no change in fat mass (Cybulski et al., 2009; Tang et al., 2016), the current study shows a reduction in fat mass upon acute loss of adipose mTORC2. Where do these differences derive from? It has been demonstrated that adiponectin is expressed in adipocyte precursors in WAT (Hong et al., 2015) and that *Adipoq* expression is already detectable in WAT at embryonic day 17.5 (Birsoy et al., 2011). Although the deletion of RICTOR in adipocyte precursors needs to be confirmed, loss of mTORC2 during early adipogenesis may provoke compensatory mechanisms to maintain proper adipose tissue development.

Hepatic TG accumulation is a common symptom observed in patients and mouse models of lipodystrophy (Lim et al., 2021). Since hepatocytes are not specialized to store high quantities of TGs, patients and mice with impaired WAT develop NAFLD, a chronic liver disease that can progress to cirrhosis and hepatocellular carcinoma. To treat NAFLD, DNL inhibitors are currently being tested in clinical trials (Ferguson & Finck, 2021). However, our findings show the importance of hepatic DNL for whole-body energy homeostasis in mice with impaired WAT function. Thus, our data indicate that targeting hepatic DNL may not be ideal to treat NAFLD in patients with underlying metabolic disorders.

The immunosuppressant drug rapamycin has shown potential to extend lifespan and prevent age-related diseases including neurogenerative disease and cancer. However, it has been shown that rapamycin treatment causes insulin resistance and glucose intolerance (Cummings & Lamming, 2017; G. Y. Liu & Sabatini, 2020). A previous study demonstrated that these rapamycin-mediated adverse effects are mainly caused by the inhibition of hepatic mTORC2 (Lamming et al., 2012). However, chronic rapamycin treatment also inhibited adipose mTORC2 (Lamming et al., 2012). The contribution of mTORC2 loss in WAT together with hepatic mTORC2 has not been previously investigated. Our studies provide a new insight that inhibition of both adipose and liver mTORC2 may significantly contribute to the pathogenesis of rapamycin-induced insulin resistance and glucose intolerance. Thus, our findings stress the necessity of developing selective mTORC1 (Lee et al., 2021; Schreiber et al., 2019).

3.2.5. Materials and Methods

Mice. Tamoxifen-inducible adipose-specific *Rictor* knockout (iAdRiKO:*Rictor*$^{fl/fl}$*, adipoq-CreER*^{T2}) and liver specific-Rictor knockout (LiRiKO: *Rictor*$^{fl/fl}$*, alb-Cre*) mice were described previously (Hagiwara et al., 2012; Shimobayashi et al., 2018). iAdRiKO and LiRiKO mice were crossed to generate adipose- and liver-specific double *Rictor* knockout (dRiKO: *Rictor*$^{fl/fl}$*, adipoq-CreER*^{T2}*, alb-Cre)* mice. For iAdRiKO and dRiKO mice, *Rictor* knockout was induced by *i.p. injection of* 1 mg/mouse tamoxifen (Sigma-Aldrich) in corn oil (Sigma-Aldrich) for 5 days. Littermate *Cre* negative animals were used as a control. Control mice were also treated with tamoxifen. Mice were housed at 22 ºC in a conventional facility with a 12 hour light/dark cycle with unlimited access to water and normal chow diet (KLIBA). Only male mice between 6 and 12 weeks of age were used for experiments. Body composition was measured by nuclear magnetic resonance imaging (Echo Medical Systems).

Immunoblots. Isolated tissues were snap frozen in liquid nitrogen and stored at -80 ºC. Frozen tissues were homogenized in a lysis buffer containing 100 mM Tris (Merck) pH7.5, 2 mM EDTA (Sigma-Aldrich), 2 mM EGTA (Sigma-Aldrich), 150 mM NaCl (Sigma-Aldrich), 1% Triton X-100 (Fluka), cOmplete inhibitor cocktail (Roche) and PhosSTOP (Roche). Protein concentration was determined by Bradford assay (Bio-rad), and equal amounts of protein were separated by SDS-PAGE, and transferred onto nitrocellulose membranes (GE Healthcare). Antibodies used in this study were as follows: RICTOR (Cat#2140) AKT (Cat#4685 or Cat#2920), AKT-pS473 (Cat#4060), FASN (Cat#3189), and ACC (Cat#3662) from Cell Signaling Technology, and CALNEXIN (Cat#ADI-SPA-860-F) from Enzo Life Sciences.

Body composition measurement. Body composition was measured by nuclear magnetic resonance imaging (Echo Medical Systems).

2-Deoxyglucose uptake assay. Mice were fasted for five hours, then injected i.p. with Humalog insulin (Lilly; 0.75 U/kg body weight), followed 10 minutes later with an injection of 2-deoxyglucose (Sigma- Aldrich; 32.8 µg/g body weight). Tissues were collected 20 minutes after administration of 2-deoxyglucose. Tissues were lysed in 10 mM Tris-HCL, pH 8.0, by boiling for 15 minutes. 2-Deoxyglucose-6-phosphate (2DGP) was measured using a Glucose Uptake-Glo Assay Kit (Promega) following the manufacturer's instructions.

Histology. Tissues were fixed in 4% formalin (Biosystems), embedded in paraffin (Biosystems), and sliced into 4 µm thick sections. Tissue sections were stained with Hematoxylin (Sigma-Aldrich) and eosin (Waldeck), and imaged by a conventional microscope (Zeiss). Adipocyte diameters were quantified with FIJI by using the Adiposoft plugin (Galarraga et al., 2012).

Triglyceride measurement. 50-100 mg liver tissues were homogenized by a dounce homogenizer in 5% NP-40 in ddH_2O. The homogenates were slowly heated up to 90 ºC for 5 minutes and cooled down to room temperature. This heating-cooling cycle was repeated once more. The homogenates were centrifuged at 14'000 g for 2 min and the supernatant was used to measure triglyceride using a triglyceride quantification kit (Abcam) by following the manufacture's instruction. The hepatic TG levels were normalized to liver weights. Plasma

TG levels were measured by a biochemical analyzer (Cobas c III analyser, Roche) or a triglyceride quantification kit (Abcam).

Fasting insulin measurement. Mice were fasted for 16 hours and blood samples were collected to determine fasting insulin and blood glucose levels. Plasma insulin levels were measured by ultrasensitive mouse insulin ELISA kit (Crystal Chem) according to the manufacturer's instructions.

Insulin and glucose tolerant test. For the insulin and glucose tolerance tests, mice were fasted for 6 hours or overnight, respectively. Insulin Humalog (Lilly, i.p. 0.5 U/kg body weight) for insulin tolerance test or glucose (Sigma-Aldrich, 2 g/kg body weight) for glucose tolerance test was i.p. administered. Blood glucose was measured with a blood glucose meter (Accu-Check, Roche). Plasma insulin levels were measured by ultrasensitive mouse insulin ELISA kit (Crystal Chem) according to the manufacturer's instructions.

Study Approval. All animal experiments were performed in accordance with federal guidelines for animal experimentation and were approved by the Kantonales Veterinäramt of the Kanton Basel-Stadt.

Statistics. Sample size was chosen according to our previous studies and published reports in which similar experimental procedures were described. All data are shown as the mean ± SEM. Sample numbers are indicated in each figure legend. To determine the statistical significance between 2 groups, an unpaired two-tailed Student's t-test was performed. For more than 3 groups, one-way ANOVA was performed. For insulin tolerance test and glucose tolerance test, two-way ANOVA was performed. All statistical analyses were performed using GraphPad Prism 9 (GraphPad Software). A p value of less than 0.05 was considered statistically significant.

Acknowledgements

We thank Stefan Offermanns (MPI-HLR, Germany) for mouse, Cécile Aude Pfaff (Biozentrum) for technical supports, and Geert Carmeliet (KU Leuven), Karen Moermans (KU Leuven) for supports for histology. We acknowledge support from the Swiss National Science Foundation (project 179569 and NCCR 182880 to MNH and 161510 to MS), European Foundation of the study of Diabetes/Novo Nordisk Foundation (MS), The Louis Jeantet Foundation (MNH), and the Canton of Basel (MNH).

Author contribution

ICF, MNH and MS conceived the project and designed the experiments. ICF, DW, and MS performed experiments and analyzed data. ICF, MNH and MS wrote the manuscript.

3.2.6. Figures

Figure 1

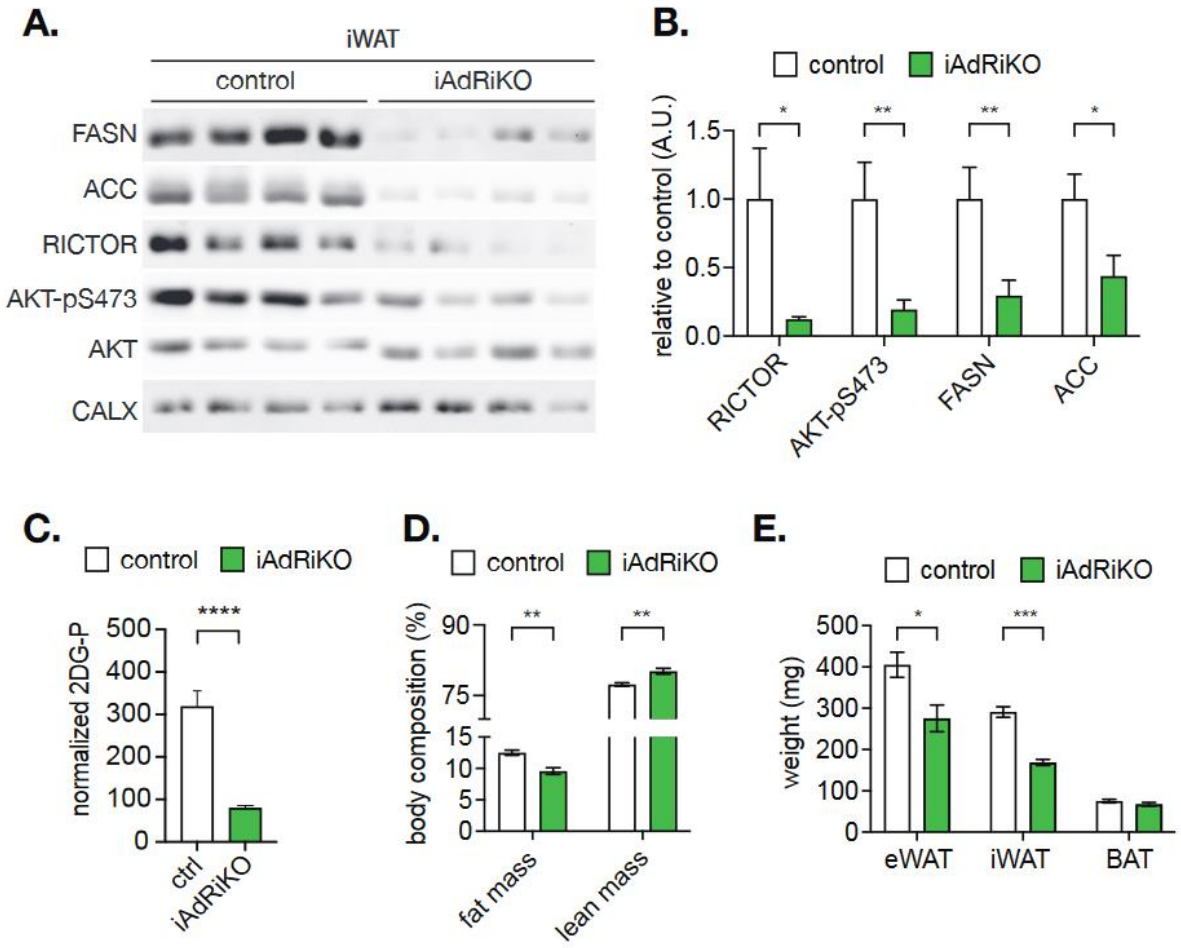

Figure 1. Loss of adipose mTORC2 in adult mice causes mild lipodystrophy
(A) Immunoblot analyses of inguinal WAT (iWAT) from control and iAdRiKO mice. CALX serves as a loading control. n=9 (control) and 12 (iAdRiKO).
(B) Quantification of immunoblots in D. The intensities of RICTOR, FASN, ACC were normalized to CALX and the intensities of AKT-pS473 were normalized to AKT. Student's t-test, *p<0.05, **p<0.01.
(C) 2- deoxyglucose (2DG) uptake in iWAT of control and iAdRiKO mice (n= 6). Student's t-test, **** p<0.0001
(D) Body composition of control and iAdRiKO mice. Student's t-test, **p<0.01. n=5 (control) and 8 (iAdRiKO).
(E) Organ weight for epididymal white adipose tissue (eWAT), iWAT, and brown adipose tissue (BAT). Student's t-test, *p<0.05, ***p<0.001. n=9 (control) and 8 (iAdRiKO).

Figure 2

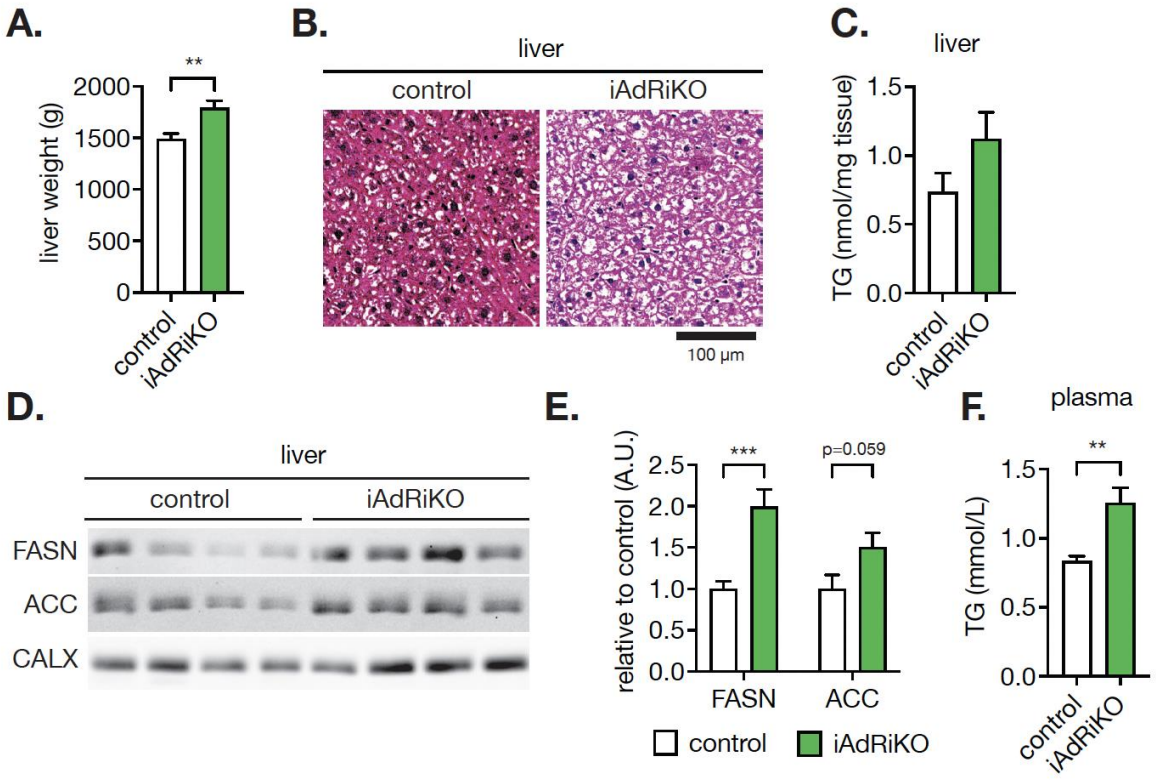

Figure 2. Loss of adipose mTORC2 in adult mice increases expression of lipogenic enzymes in the liver and hypertriglyceridemia

(A) The liver weight of control and iAdRiKO mice. Student's t-test, **p<0.01. n=9 (control) and 8 (iAdRiKO).

(B) Representative hematoxylin and eosin staining of control and iAdRiKO liver. n=3 (control) and 3 (iAdRiKO).

(C) Hepatic triglyceride (TG) levels in control and iAdRiKO mice. Student's t-test. n=9 (control) and 12 (iAdRiKO).

(D) Immunoblot analyses of liver from control and iAdRiKO mice. CALX serves as a loading control. n=9 (control) and 12 (iAdRiKO).

(E) Quantification of immunoblots in E. The intensities of FASN and ACC were normalized to CALX. Student's t-test, **p<0.01.

(F) Plasma TG levels in control and iAdRiKO mice. Student's t-test, **p<0.01. n=15 (control) and 15 (iAdRiKO).

Figure 3

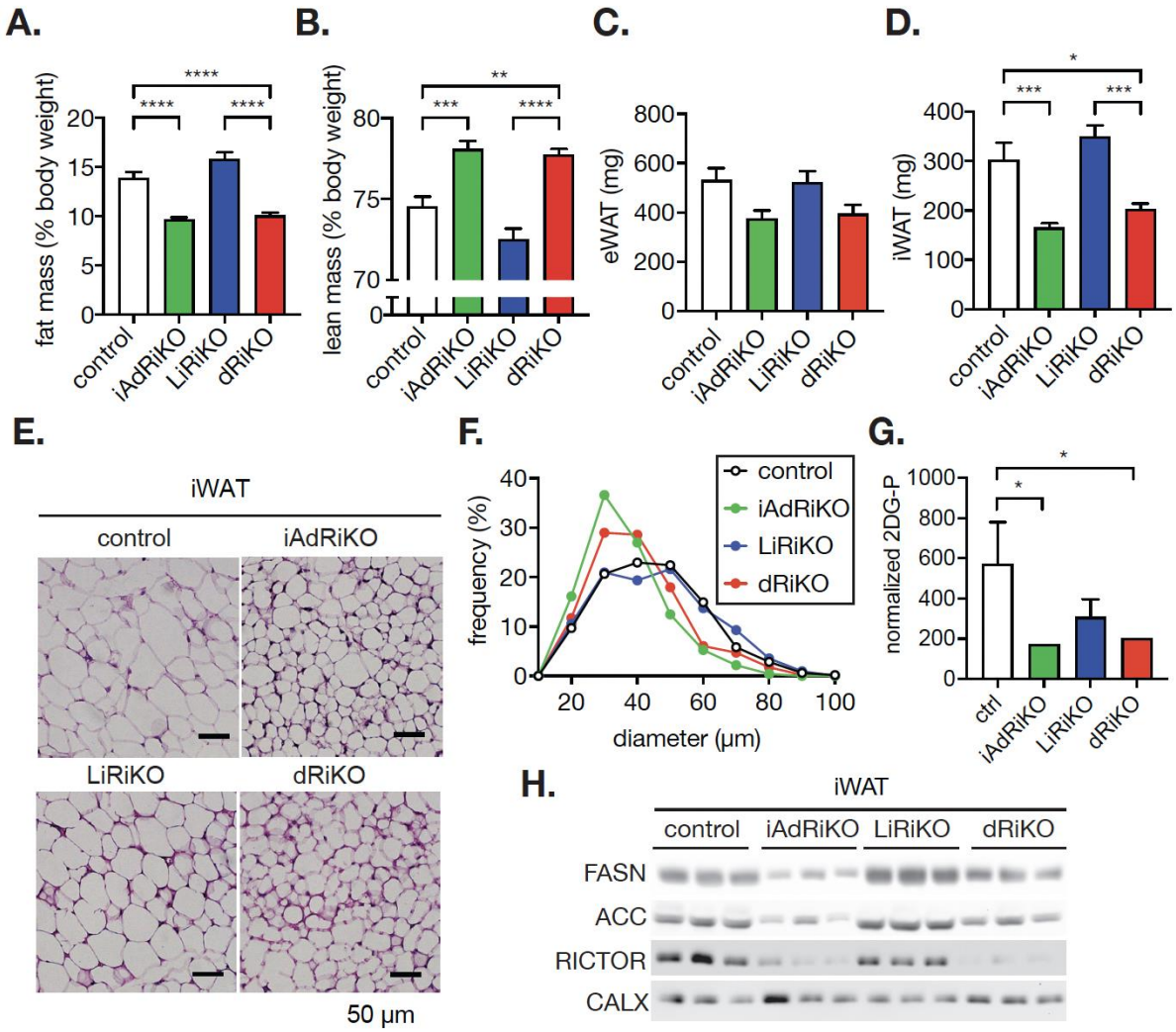
A.
fat mass (% body weight)
control
iAdRiKO
LiRiKO
dRiKO
B.
lean mass (% body weight)
C.
eWAT (mg)
D.
iWAT (mg)
E.
iWAT
control
iAdRiKO
LiRiKO
dRiKO
50 µm
F.
frequency (%)
diameter (µm)
G.
normalized 2DG-P
ctrl
H.
iWAT
FASN
ACC
RICTOR
CALX

Figure 3. Loss of adipose and hepatic mTORC2 causes mild lipodystrophy
(A-B) Fat mass (A) and lean mass (B) of control, iAdRiKO, LiRiKO, and dRiKO mice. One-way ANOVA, **p<0.01, ***p<0.001, ****p<0.0001. n=11 (control), 12 (iAdRiKO), 13 (LiRiKO), and 12 (dRiKO).
(C) Epididymal white adipose tissue (eWAT) weight of control, iAdRiKO, LiRiKO, and dRiKO mice. One-way ANOVA. n=9 (control), 11 (iAdRiKO), 11 (LiRiKO), and 7 (dRiKO).
(D) Inguinal white adipose tissue (iWAT) weight of control, iAdRiKO, LiRiKO, and dRiKO mice. One-way ANOVA, *p<0.05, ***p<0.001. n=9 (control), 11 (iAdRiKO), 11 (LiRiKO), and 7 (dRiKO).
(E) Representative hematoxylin and eosin staining of control, iAdRiKO, LiRiKO, and dRiKO iWAT. n=7 (control), 3 (iAdRiKO), 6 (LiRiKO), 7 (dRiKO).
(F) Quantification of adipocyte diameters for the images in F.
(G) 2- deoxyglucose (2DG) uptake in iWAT of control, iAdRiKO, LiRiKO and dRiKO mice. n=6 (control), 11 (iAdRiKO), 8 (LiRiKO), 12 (dRiKO). Student's t test, * p<0.05
(H) Immunoblot analyses of liver from control, iAdRiKO, LiRiKO, and dRiKO mice. CALX serves as a loading control. n=9 (control), 12 (iAdRiKO), 11 (LiRiKO), 7(dRiKO).

Figure 4

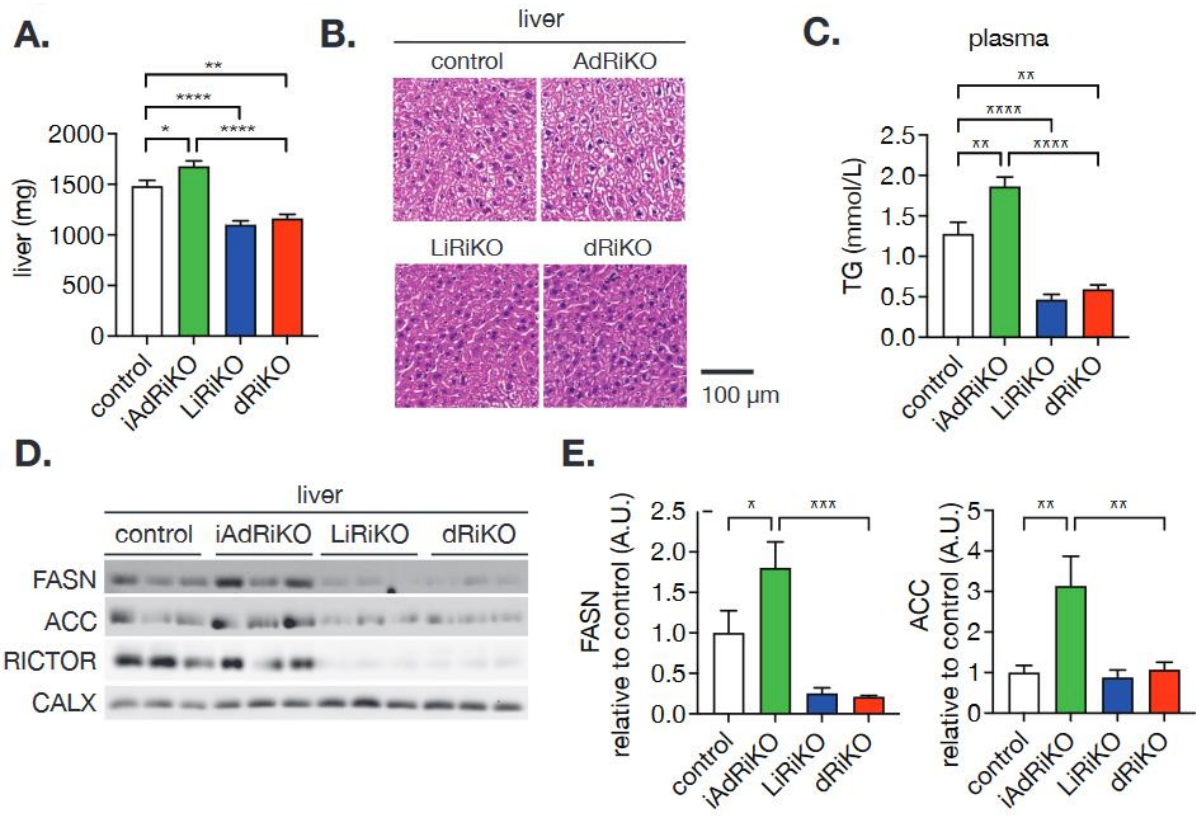

Figure 4. Loss of adipose and hepatic mTORC2 causes reduced expression of lipogenic enzymes in the liver and hypotriglyceridemia in mice.
(A) The liver weight of control, iAdRiKO, LiRiKO, and dRiKO mice. n=9 (control), 11 (iAdRiKO), 11 (LiRiKO), 7 (dRiKO). One-way ANOVA, *p<0.05, **p<0.01, ****p<0.001.
(B) Representative hematoxylin and eosin staining of control, iAdRiKO, LiRiKO, and dRiKO liver. n=3 (control), 3 (iAdRiKO), 3 (LiRiKO), 3 (dRiKO).
(C) Plasma TG levels in control, iAdRiKO, LiRiKO, and dRiKO mice. One-way ANOVA, **p<0.01, ****p<0.001. n=9 (control), 11 (iAdRiKO), 11 (LiRiKO), 7 (dRiKO).
(D) Immunoblot analyses of liver from control, iAdRiKO, LiRiKO, and dRiKO mice. CALX serves as a loading control. n=6 (control), 6 (iAdRiKO), 6 (LiRiKO), 6 (dRiKO).
(E) Quantification of immunoblots in D. The intensities of FASN and ACC were normalized to control. One-way ANOVA, **p<0.01.

Figure 5

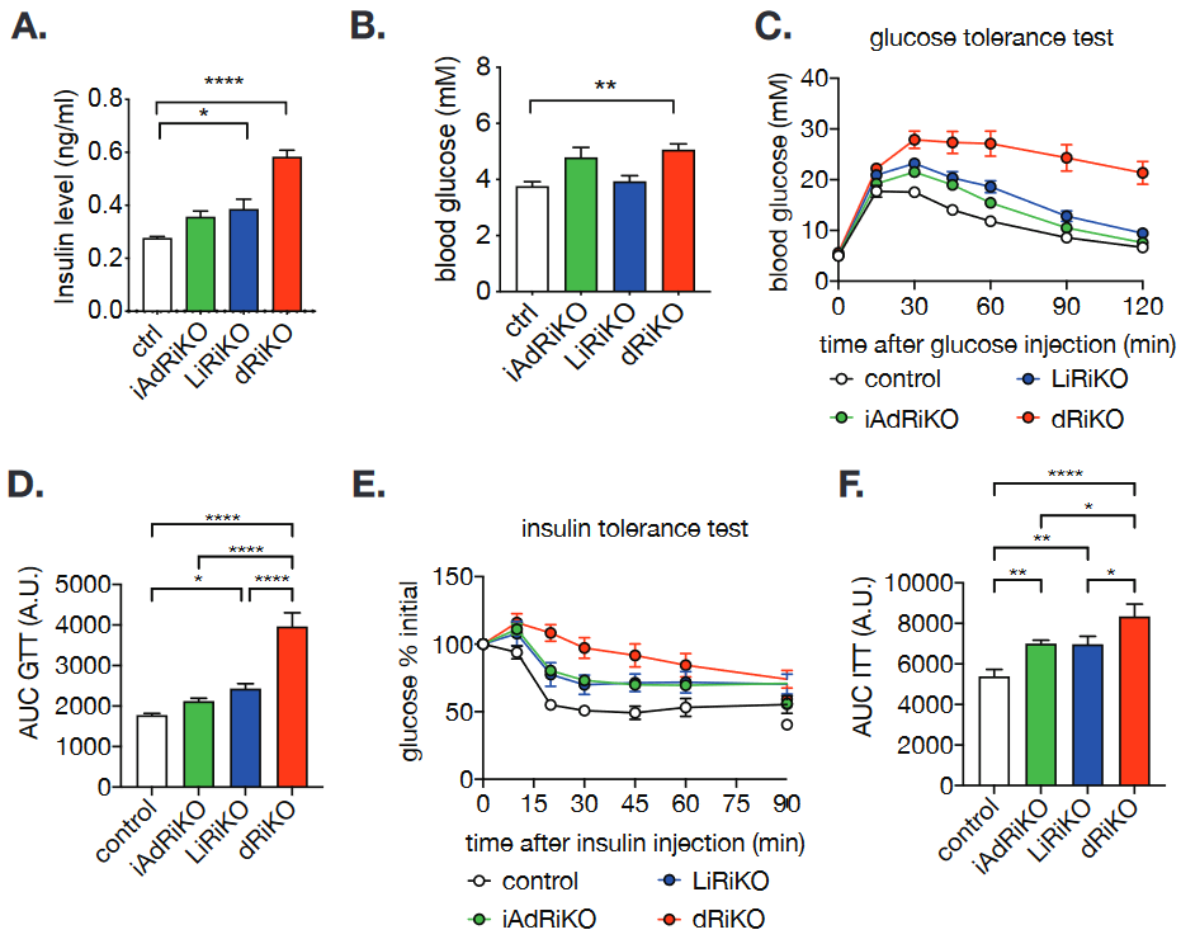

Figure 5. Loss of adipose and hepatic mTORC2 causes insulin resistance and glucose intolerance.

(A) Plasma insulin levels of control, iAdRiKO, LiRiKO and dRiKO mice after 16 hour starvation. One-way ANOVA, *p<0.05, ****p<0.0001. n= 4 (control), 5 (iAdRiKO), 5 (LiRiKO), 7 (dRiKO).

(B) Blood glucose levels of control, iAdRiKO, LiRiKO and RidKO mice mice after 16 hour starvation, One-way ANOVA, **p<0.01. n= 4 (control), 5 (iAdRiKO), 5 (LiRiKO), 7 (dRiKO).

(C) Glucose tolerance test on control, iAdRiKO, LiRiKO, and dRiKO mice. The mice were fasted for 14 hours and injected with glucose (2 g/kg body weight). n=7 (control), 19 (iAdRiKO), 10 (LiRiKO), 9 (dRiKO).

(D) Area under the curve (AUC) of the blood glucose curves in C. Two-way ANOVA. *p<0.05, ****p<0.0001.

(E) Insulin tolerance test on control, iAdRiKO, LiRiKO, and dRiKO mice. The mice were fasted for 6 hours and injected with insulin (0.75 U/kg body weight). n=18 (control), 19 (iAdRiKO), 11 (LiRiKO), 9 (dRiKO).

(F) Area under the curve (AUC) of the blood glucose curves in E. Two-way ANOVA. **p<0.01, ****p<0.0001.

3.2.7. Supplementary Figures

Supplementary Figure 1

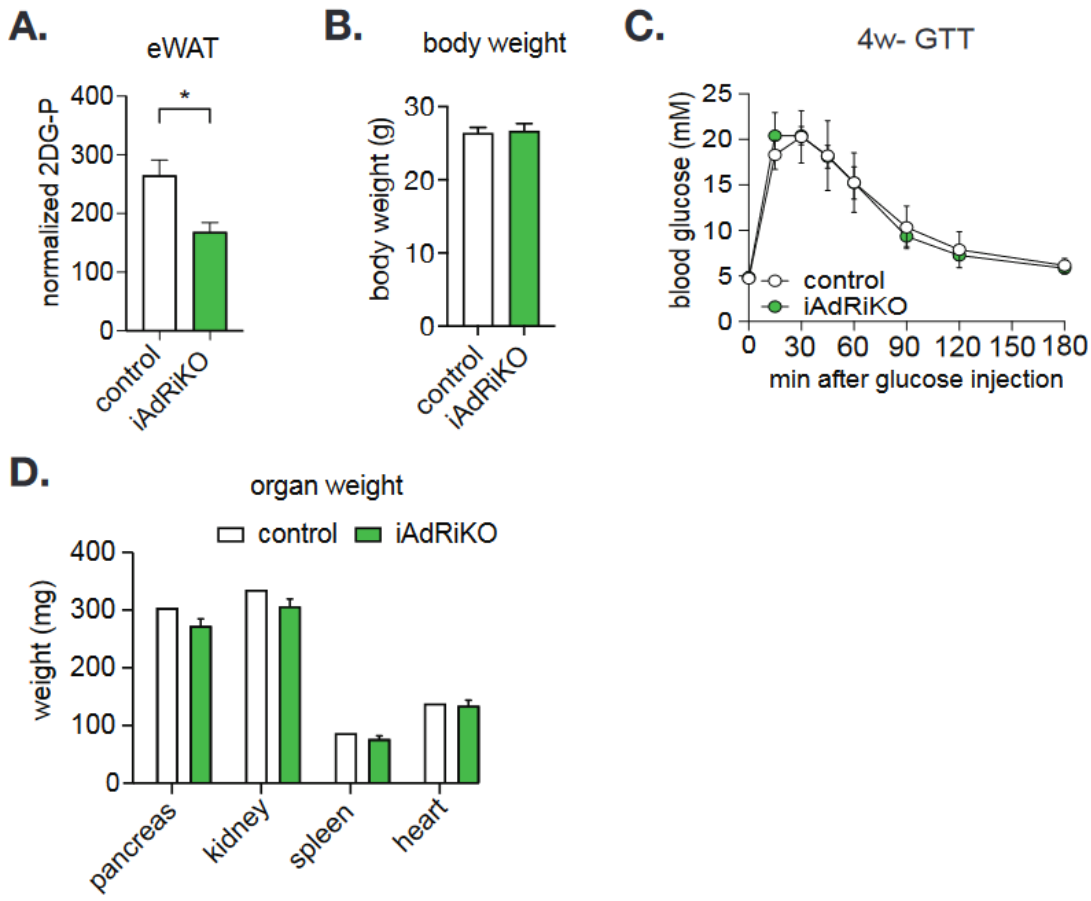

Supplementary Figure 1.
(A) 2-deoxyglucose (2DG) uptake in epididymal WAT (eWAT) of control and iAdRiKO mice four weeks after tamoxifen treatment. n= 6, Student's t-test, * $p<0.05$
(B) Body weight of control and iAdRiKO mice. n=9 (control) and 8 (iAdRiKO).
(C) Glucose tolerance test on control and iAdRiKO mice. n= 6
(D) Organ weight for pancreas, kidney, spleen and heart. n=7 (control) and 6 (iAdRiKO).

Supplementary Figure 2

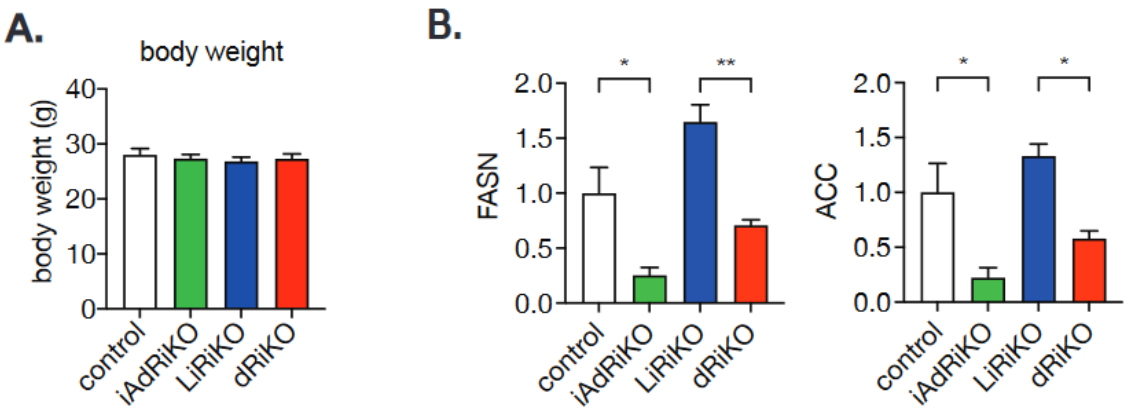

Supplementary Figure 2.
(A) Body weight of control, iAdRiKO, LiRiKO, and dRiKO mice. n=9 (control), 12 (iAdRiKO), 11 (LiRiKO), and 7 (dRiKO).
(B) Quantification of immunoblots in Figure 3H. The intensities of FASN and ACC were normalized to control. One-way ANOVA, *p<0.05, **p<0.01.

3.3 Supplementary Data

Supplementary Data 1

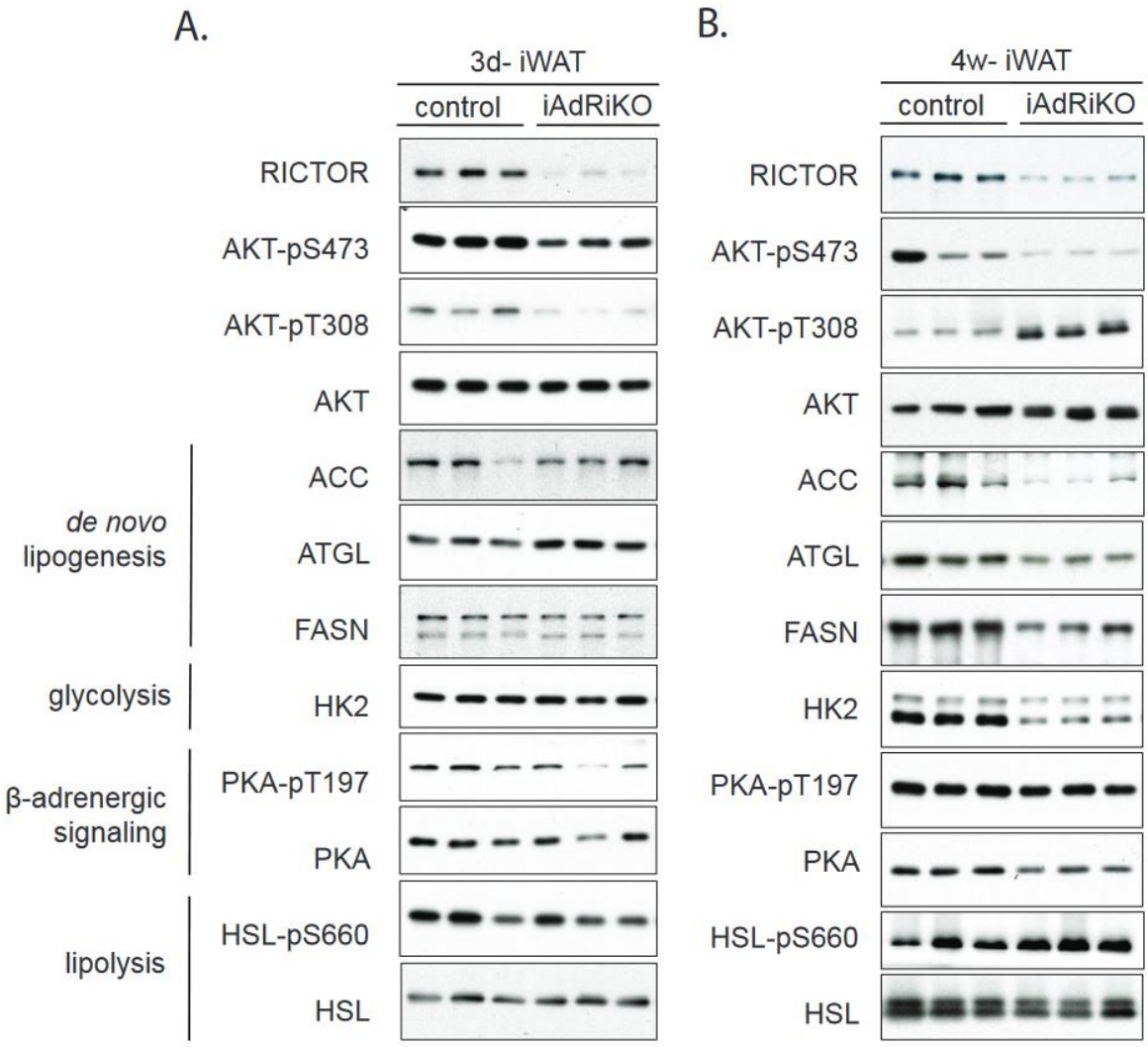

Supplementary data 1: De novo lipogenesis is not reduced upon acute loss of adipose mTORC2
(A) Immunoblot analysis of inguinal WAT (iWAT) from control and iAdRiKO mice three days after tamoxifen treatment.
(B) Immunoblot analysis of inguinal WAT (iWAT) from control and iAdRiKO mice four weeks after tamoxifen treatment.

Supplementary Data 2

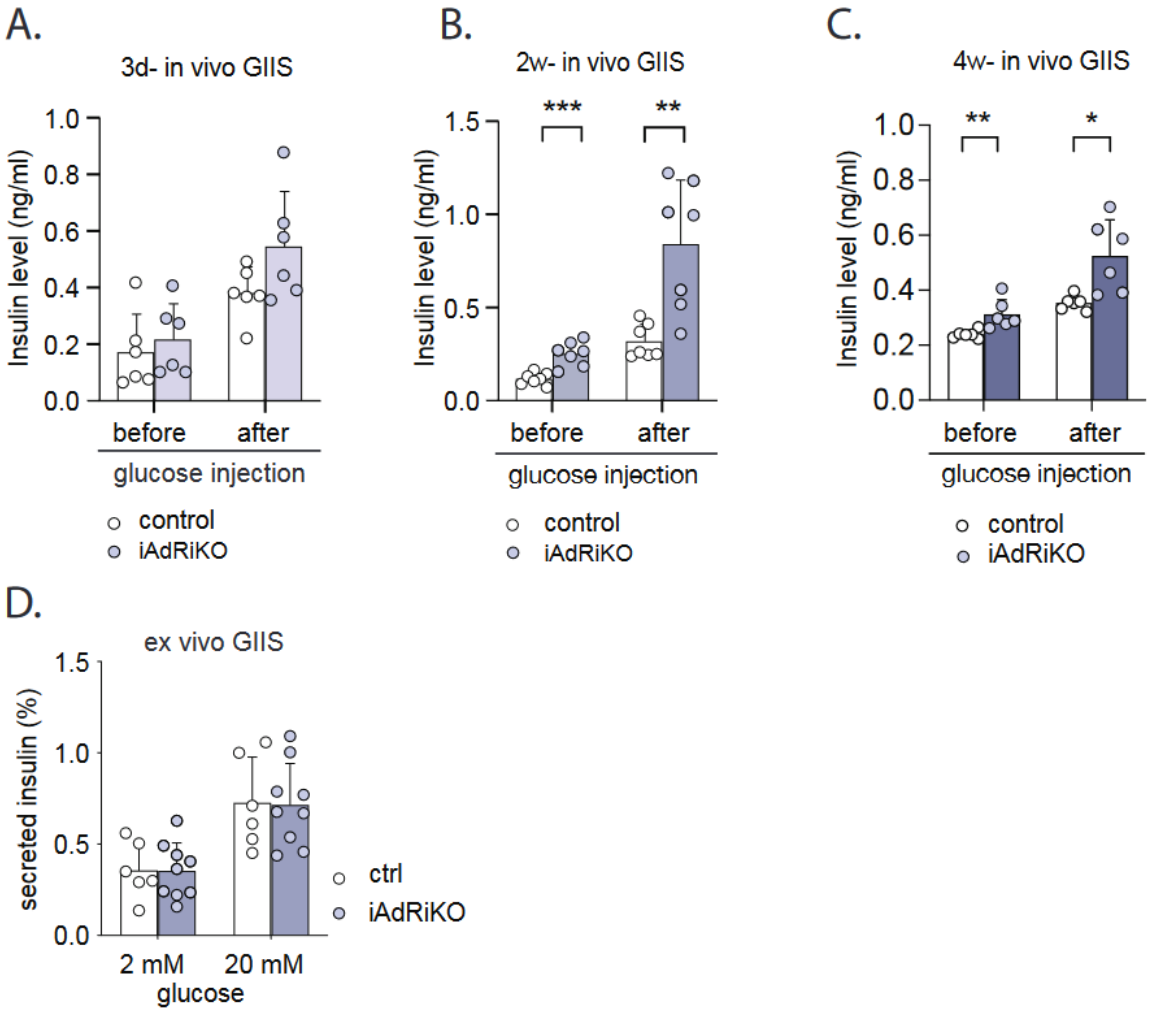

Supplementary data 2: *In vivo* and *ex vivo* insulin secretion assays suggest the existence of a mTORC2-dependent factor *in vivo*

(A) *In vivo* glucose-induced insulin secretion (GIIS) of pancreatic β-cells in control and iAdRiKO mice three days after tamoxifen treatment (n=6).

(B) *In vivo* GIIS of pancreatic β-cells in control and iAdRiKO mice two weeks after tamoxifen treatment (n=7). Student's t-test, **p<0.01, ***p<0.001

(C) *In vivo* GIIS of pancreatic β-cells in control and iAdRiKO mice four weeks after tamoxifen treatment. Student's t-test, *p<0.05, **p<0.01

(D) *Ex vivo* GIIS of isolated pancreatic islets for control and iAdRiKO mice two weeks after tamoxifen treatment (n=6;9).

Supplementary Data 3

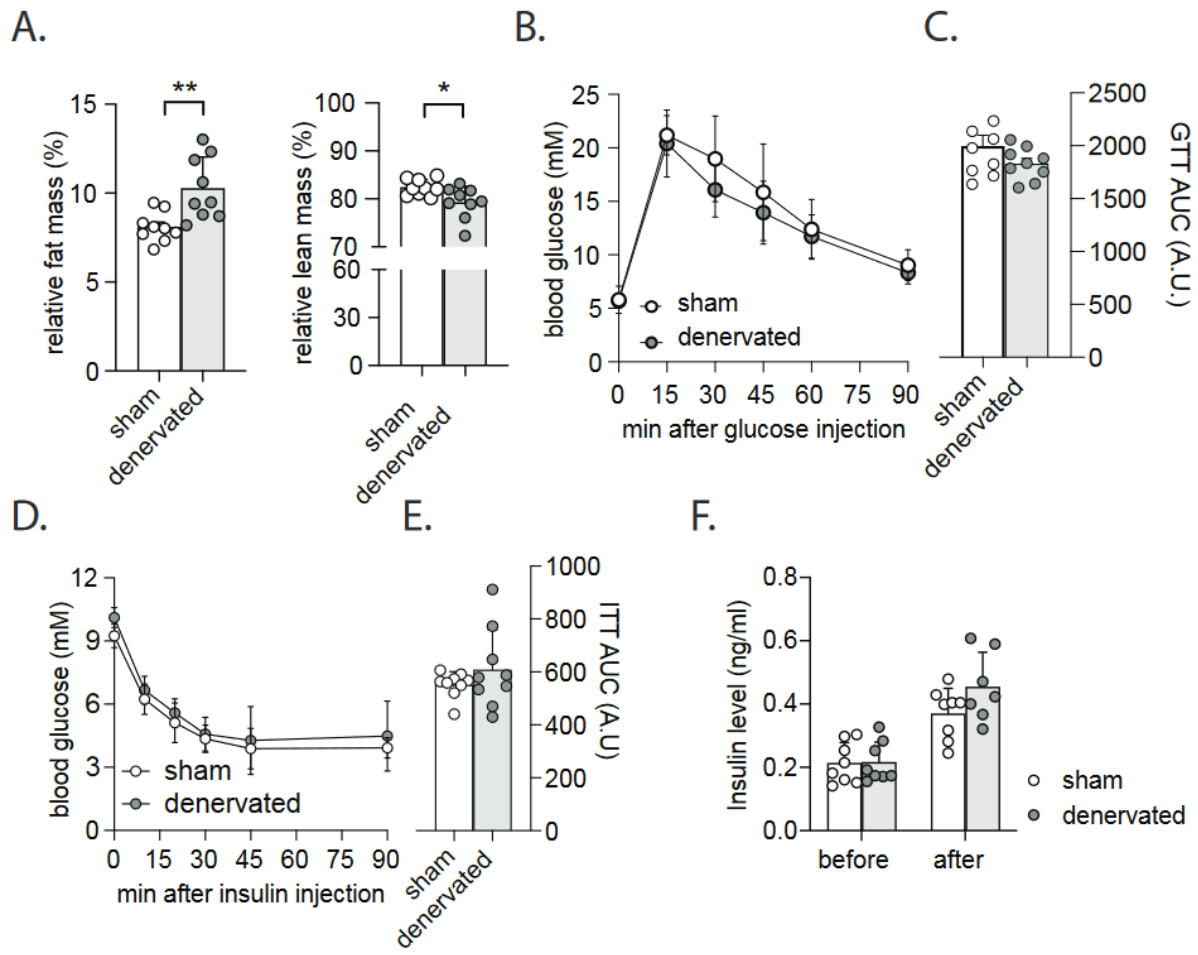

Supplementary data 3: Surgical denervation of both inguinal fat pads did not impact whole-body energy homeostasis

(A) Body composition of surgical denervated and sham-operated mice (n=9). Student's t-test, *p<0.05, **p<0.01

(B) Glucose tolerance test (GTT) on surgical denervated and sham-operated mice (n=9).

(C) Area under the curve for GTT on surgical denervated and sham-operated mice (n=9).

(D) Insulin tolerance test (ITT) on surgical denervated and sham-operated mice (n=9).

(E) Area under the curve for ITT on surgical denervated and sham-operated mice (n=9).

(F) *In vivo* GIIS of pancreatic β-cells in surgical denervated and sham-operated mice (n=9).

Supplementary Data 4

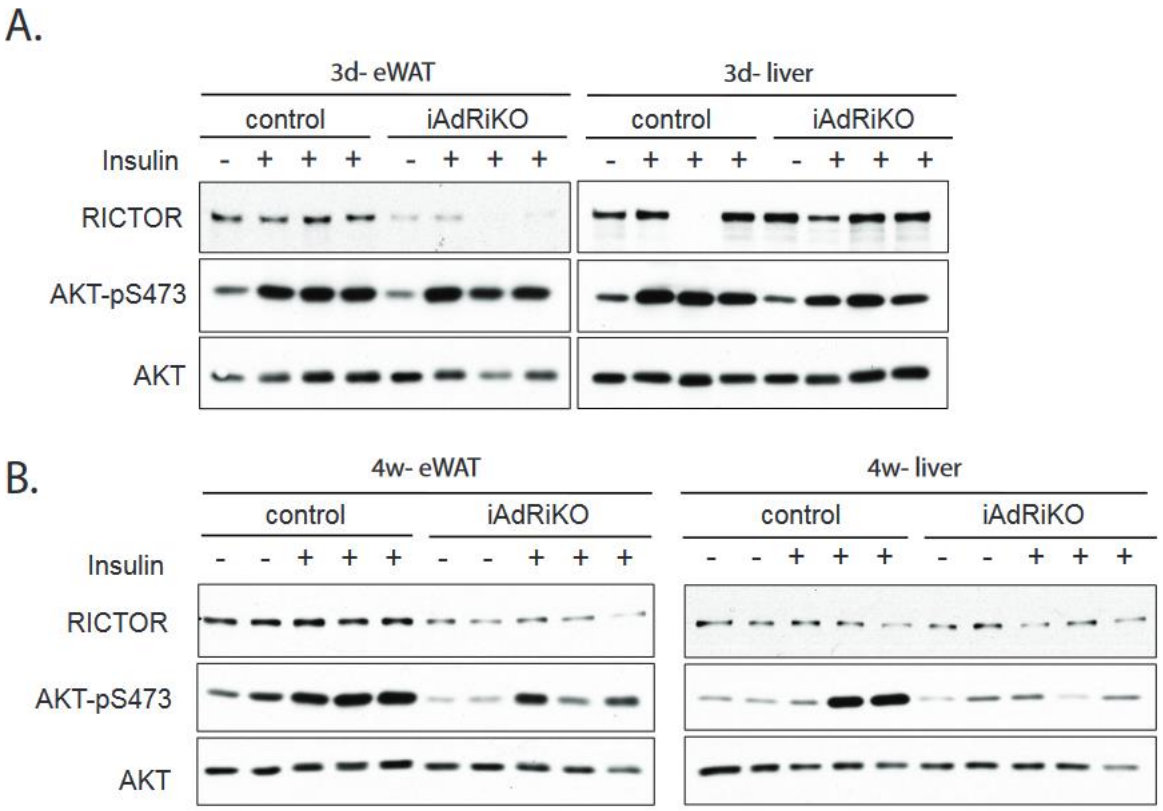

Supplementary data 4: iAdRiKO mice develop hepatic insulin resistance
(A) Insulin-stimulated phosphorylation of AKT in epididymal white adipose tissue (eWAT) and liver of iAdRiKO mice three days after tamoxifen treatment.
(B) Insulin-stimulated phosphorylation of AKT in eWAT and liver of iAdRiKO mice four weeks after tamoxifen treatment.

Supplementary Data 5

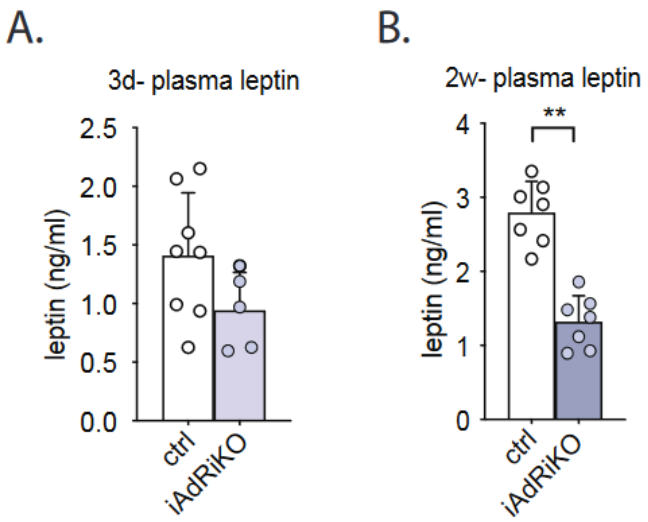

Supplementary data 5: Loss of adipose mTORC2 reduces plasma leptin level
(A) Plasma leptin level in control and iAdRiKO mice three days after tamoxifen treatment. (n=8;5)
(B) Plasma leptin level in control and iAdRiKO mice two weeks after tamoxifen treatment (n=7). Student's t-test, **p<0.01

Chapter 4: Discussion

4. Discussion

In this thesis, we aimed to study the role of mTORC2 in mature adipocytes and its impact on whole-body energy homeostasis. To achieve our goal, we generated tamoxifen-inducible adipose-specific RICTOR knockout (iAdRiKO) mice and performed a longitudinal study to examine the effect of acute loss of adipose mTORC2.

4.1 Role of mTORC2 in adipocytes

Previous studies using mice lacking adipose mTORC2 from birth have reported an essential role of mTORC2 in glucose uptake and DNL (Cybulski et al., 2009; Hsiao et al., 2020; Kumar et al., 2010; Tang et al., 2016). In agreement with these findings, we show that loss of mTORC2 activity in mature adipocytes reduces glucose uptake and expression of lipogenic genes such as ACC and FASN (**Supplementary Data 1**). These findings indicate that mTORC2 directly regulates both glucose uptake and DNL and the previous findings were not due to a developmental defect. In addition, our longitudinal study revealed an immediate reduction of glucose uptake upon acute loss of adipose mTORC2 (three day after tamoxifen treatment) while ACC and FASN expression were still intact (**Supplementary Data 1**). Results from our proteome and phosphoproteome analysis suggest that acute phenotypes are due to changes in protein phosphorylation. These observations are consistent with prior results showing that mTORC2 substrates AKT and PKC promote the translocation of the glucose transporter GLUT4 to the plasma membrane via phosphorylation (Alessi et al., 1997; Bandyopadhyay et al., 1997). A previous study has proposed that mTORC2 transcriptionally regulates adipose DNL by promoting the expression of the transcription factor ChREBPβ (Tang, 2016). Since it has been established that glucose influx promotes ChREBPα activity and thereby ChREBPβ expression (Herman et al., 2012), our and previous data indicate that mTORC2-dependent decrease of glucose influx may downregulate ChREBPβ expression. In agreement with this notion, high sucrose diet rescues CHREBPβ, ACC and FASN expression in WAT lacking mTORC2 (Tang et al., 2016). However, a recent study challenges the role of ChREBPβ in adipose DNL (Recazens, 2022). Thus, glucose influx may promote ACC and FASN expression in a ChREBPβ- independent manner.

Acute loss of adipose mTORC2 not only impacts glucose uptake, but also changes the phosphorylation of proteins associated with the plasma membrane. Alterations in the plasma

membrane influence the import and export of molecules, the abundance of transmembrane receptors and affects extracellular matrix composition. Interestingly, adipose extracellular matrix remodeling has been previously associated with insulin resistance and obesity (Lin, Chun, & Kang, 2016). Thus, loss of adipose mTORC2 provides a potential mechanism for extracellular matrix remodeling upon insulin resistance.

Despite the fact that both constitutive and acute knockout of adipose mTORC2 impair glucose uptake and DNL, only acute mTORC2 ablation causes mild lipodystrophy. Where do these differences arise from? For the deletion of RICTOR, we and others have used the adiponectin promoter as the Cre-driver (Tang et al., 2016). It has been demonstrated that adiponectin is expressed in adipocyte precursors in WAT (Hong et al., 2015) and that *Adipoq* mRNA is already detectable in WAT at embryonic day 17.5 (Birsoy et al., 2011). Although the deletion of RICTOR in adipocyte precursors first requires experimentally confirmation, it is plausible that loss of mTORC2 during adipogenesis poses a unique selective pressure that may promote a compensatory mechanism. For example, adipocytes derived from adipocyte precursors lacking mTORC2 may possess reduced metabolic capacity. This is in agreement with the observation that mice lacking adipose mTORC2 from birth exhibit normal fat mass, but are resistant to both high fat diet- and high sucrose diet- induced adiposity (Tang et al., 2016).

Taken together, our study confirmed the importance of adipose mTORC2 in glucose uptake and DNL. Impaired mTORC2 activity diminishes the capacity of adipose tissue to absorb excess energy and thus prevents energy storage. In addition, we provide evidence for an important regulatory role of adipose mTORC2 in plasma membrane-associated processes.

4.2 Role of adipose mTORC2 in whole-body energy homeostasis

In this thesis, we show that loss of adipose mTORC2 in mature adipocytes rapidly impairs whole-body energy homeostasis. Hyperinsulinemia develops upon acute adipose mTORC2 ablation, suggesting a potential regulatory role of adipose mTORC2 in insulin secretion from pancreatic β-cells. Accordingly, we found that mice lacking adipose mTORC2 display increased glucose-stimulated insulin secretion *in vivo* compared to controls (**Supplementary Data 2**). However, isolated pancreatic islets from these mice lose the capacity to secrete more insulin than islets from controls suggesting the presence of a mTORC2-dependent factor *in vivo* (**Supplementary Data 2**). Interestingly, the increase in fasting insulin levels appears contemporaneously with changes in the phosphorylation status of proteins involved in

synapse formation. Thus, we hypothesized that sensory inputs from WAT may promote insulin secretion in pancreatic β-cells to compensate for reduced insulin signaling in adipose tissue. Further investigation revealed reduced arborization of sensory neurons in WAT lacking mTORC2. Although the exact role of sensory neurons in WAT remains uncharacterized, there is evidence for a regulatory role in energy homeostasis (Blaszkiewicz, Willows, Johnson, et al., 2019). For example, systemic ablation of CGRP-positive sensory neurons prevents accumulation of fat mass to a similar extent as ablation of adipose mTORC2 (Makwana et al., 2021). In addition, FFA and leptin are the only experimentally confirmed stimuli for sensory neurons in WAT and both are secreted depending on the metabolic state of adipocytes (Garretson et al., 2016; K. T. Murphy et al., 2013). Nevertheless, surgical denervation of both inguinal fat pads did not confirm a role for peripheral neurons in whole-body energy homeostasis (**Supplementary Data 3**). Both inguinal fat pads account for approximately 10% of fat mass in adult mice. Thus, loss of sensory neurons derived from inguinal fat pads may not be enough to derail systemic metabolic parameters. Further investigation with mice lacking CGRP-positive neurons in WAT is required to make a definite conclusion on the role of WAT-innervating sensory neurons in whole body energy homeostasis.

How does mTORC2 impair whole-body energy homeostasis if it is not via the sensory neurons? Impaired whole-body energy homeostasis in mice lacking mTORC2 coincides with reduced fat mass and smaller adipocytes, indicating lipodystrophy. Lipodystrophy is characterized by loss of adipose tissue resulting in severe systemic insulin resistance and ectopic accumulation of lipid droplets (Rochford, 2014). In agreement, mice lacking adipose mTORC2 rapidly develop systemic insulin resistance and accumulate TGs in the liver. Several studies reported a similar phenotype in mice lacking the insulin receptor, insulin-like growth factor 1 receptor and AKT1/2, indicating an important role of the insulin/mTORC2/AKT pathway in adipose tissue function and maintenance (Qiang et al., 2016; Sakaguchi et al., 2017; Shearin et al., 2016). In comparison to mice lacking mTORC2, lipodystrophy develops even faster and is more severe in mice following acute deletion of the insulin receptor (Sakaguchi et al., 2017). Interestingly, these mice recover shortly afterwards and exhibit normal whole-body energy homeostasis due to newly generated adipocytes (Sakaguchi et al., 2017). In contrast, we do not see a compensatory increase in adipogenesis and amelioration of metabolic parameters in mice lacking adipose mTORC2. Thus, adipose mTORC2 seems to be more relevant for storage of excess energy rather than adipose tissue

maintenance. Nevertheless, mild lipodystrophy and impaired storage capacity likely the reason for the observed impairment of whole-body energy homeostasis.

It is well established that impaired WAT function leads to accumulation of TGs in the liver. Accordingly, we and others have shown increased hepatic TG content in mice lacking adipose mTORC2 (Cybulski et al., 2009; Tang et al., 2016). In this thesis, we show that mice lacking adipose mTORC2 display increased expression of lipogenic enzymes in the liver. Normally, insulin promotes expression of lipogenic enzymes via mTORC2-dependent SREBP1c activation (Hagiwara et al., 2012). However, mice lacking adipose mTORC2 show reduced hepatic insulin sensitivity including diminished AKT-pS473 phosphorylation (**Supplementary Data 4**). Hence, reduced hepatic DNL would be the expected consequence. A possible explanation for this discrepancy is the increased influx of glucose into the liver (**Supplementary Data 4**). Glucose and its breakdown products increase ChREBP transcription and activity, thereby promoting the expression of lipogenic genes (Postic, Dentin, Denechaud, & Girard, 2007). In addition, basal AKT-p473 phosphorylation is still present in the absence of insulin stimulation, a condition found in insulin resistant livers. Thus, hepatic insulin resistance cannot be compared to genetic ablation of hepatic RICTOR which completely abolishes AKT-pS473 (Postic et al., 2007). In agreement with this notion, we show that mice lacking both hepatic and adipose mTORC2 display reduced expression of ACC and FASN and no accumulation of TG in the liver. Taken together, we and others have shown the importance of adipose mTORC2 in the regulation of excess energy in the form of glucose, lipids and FFAs (Cybulski, 2009; Albert, 2015; Tang, 2016; Hsiao, 2021). Thus, the rapid disruption of whole-body energy homeostasis detected after acute loss of adipose mTORC2 is likely due to impaired energy storage.

4.3. Role of adipose mTORC2 in neuronal innervation

While searching for a possible role of mTORC2 in interorgan communication, we discovered that adipose mTORC2 is essential for arborization of sensory neurons in WAT. To date, adipose mTORC2 is the only known regulator of sensory innervation in adipose tissue. However, the exact mechanism remains elusive. Adipose mTORC2 may promote neuronal growth, stability or both in sensory neurons while sympathetic neurons are unaffected. Thus, the underlying mechanism has to be specific only for sensory neurons. Interestingly, we found reduced GAP43 expression in WAT lacking adipose mTORC2, a protein associated with neuronal growth and synaptic plasticity (Snipes et al., 1987). Further investigations revealed

that GAP43 is only expressed in sensory neurons, but not in sympathetic neurons in WAT. The strong and rapid downregulation of GAP43 upon acute mTORC2 ablation suggests a regulatory role of adipose mTORC2 on neuronal growth and plasticity via GAP43, although we cannot formally exclude the possibility that loss of GAP43 is due to reduced sensory arborization. Thus, more experiments are required to distinguish whether adipose mTORC2 affects neuronal growth or stability, for example by examining the neuronal network prior to mTORC2 ablation.

How can adipose mTORC2 regulate growth or stability in sensory neurons? Our phosphoproteomic analysis revealed alterations in the phosphorylation status of membrane-associated proteins and cell-cell adhesion proteins upon loss of adipose mTORC2. Thus, loss of mTORC2 in adipocytes may disrupt the postsynaptic membrane, thereby destabilizing synapses. Alternatively, sensory neurons may require a secreted stimulatory factor from adipocytes to undergo arborization. It has been suggested that sensory neurons respond to secreted free fatty acids produced by lipolysis or *de novo* lipogenesis in adipocytes (Garretson et al., 2016; Guilherme et al., 2018). Since mTORC2 promotes *de novo* lipogenesis (Hagiwara et al., 2012; Tang et al., 2016), loss of mTORC2 may decrease the release of particular species of bioactive free fatty acids by adipocytes which may in turn decrease arborization of sensory neurons. Another candidate that may promote arborization of sensory neurons is leptin. In support of this hypothesis, plasma leptin level is reduced upon acute ablation of adipose mTORC2 (**Supplementary Data 5**). It was previously proposed that leptin may not only act directly on the CNS, but also via sensory neurons (K. T. Murphy et al., 2013). Thus, reduced leptin level may destabilize sensory neurons and thereby communicate to the CNS the declining TG reserves due to loss of adipose mTORC2.

The role of sensory neurons in WAT is poorly understood. It has been proposed that sensory neurons provide a feedback loop between WAT and the CNS to coordinate energy storage and expenditure (Guilherme et al., 2019). For example, sensory activity in WAT modulates SNS activity in distal fat pads by a sympathetic-sensory feedback loop (Garretson et al., 2016). However, we detect no change in sympathetic innervation or activity in mice lacking adipose mTORC2. The reason for this discrepancy is likely due to the far more complex phenotype of mice lacking adipose mTORC2. Sensory neurons not only transmit information from WAT to CNS, but also secrete neuropeptides such as CGRP. CGRP has a vasodilatory and an immunoregulatory function. However, its precise role in WAT is not studied. Mice lacking CGRP exhibit reduced fat mass and increased lipolysis (T. Liu et al.,

2017) indicating a regulatory role of CGRP in WAT metabolism. However, further studies are necessary to determine the precise role of WAT-innervating sensory neurons.

Chapter 5: Acknowledgements

5. Acknowledgements

I would like to thank Michael N. Hall for hosting me in his Lab. I'm grateful for the opportunity to work on these exciting projects and the support that was given to me.
Many thanks to Mitsugu Shimobayashi for his guidance, support and his endless patience during our long discussions. It was an honour to be supervised by him.
I would also like to thank all the current and past members of the Hall Lab for the supportive and joyful atmosphere in the Lab. A special thanks to Diana Weissenberger for introducing me to mouse work and continuously providing me with great technical support, Asier Gonzales, Don Benjamin, and Amandine Thomas for their mentoring and scientific discussions and Sujin Park, Stefania Battaglioni and Brigitte Olufsen for always providing a helping hand.
I'm grateful for the professional and constructive support that was offered by the Core Facilities of the Biozentrum, particularly the mouse facility with Frédérik Schmitt, David Überschlag, and Cassie Liss, the imaging core facility with Wolf Heusermann, Sara Roig and Kai Schleicher and the proteomics core facility with Danilo Ritz.
And finally, I would like to thank my family and friends who had to endure my limited availability. I'm thankful for all the support, advice and patience I received during my PhD.

Chapter 6: References

6. References

Aderem, A. (1992). The MARCKS brothers: a family of protein kinase C substrates. *Cell, 71*(5), 713-716. doi:10.1016/0092-8674(92)90546-o

Ahrne, E., Glatter, T., Vigano, C., Schubert, C., Nigg, E. A., & Schmidt, A. (2016). Evaluation and Improvement of Quantification Accuracy in Isobaric Mass Tag-Based Protein Quantification Experiments. *J Proteome Res, 15*(8), 2537-2547. doi:10.1021/acs.jproteome.6b00066

Albert, V., Svensson, K., Shimobayashi, M., Colombi, M., Munoz, S., Jimenez, V., . . . Hall, M. N. (2016). mTORC2 sustains thermogenesis via Akt-induced glucose uptake and glycolysis in brown adipose tissue. *EMBO Mol Med, 8*(3), 232-246. doi:10.15252/emmm.201505610

Alessi, D. R., James, S. R., Downes, C. P., Holmes, A. B., Gaffney, P. R., Reese, C. B., & Cohen, P. (1997). Characterization of a 3-phosphoinositide-dependent protein kinase which phosphorylates and activates protein kinase Balpha. *Curr Biol, 7*(4), 261-269. doi:10.1016/s0960-9822(06)00122-9

Allan, C., Burel, J. M., Moore, J., Blackburn, C., Linkert, M., Loynton, S., . . . Swedlow, J. R. (2012). OMERO: flexible, model-driven data management for experimental biology. *Nat Methods, 9*(3), 245-253. doi:10.1038/nmeth.1896

Ameer, F., Scandiuzzi, L., Hasnain, S., Kalbacher, H., & Zaidi, N. (2014). De novo lipogenesis in health and disease. *Metabolism, 63*(7), 895-902. doi:10.1016/j.metabol.2014.04.003

Angliker, N., & Ruegg, M. A. (2013). In vivo evidence for mTORC2-mediated actin cytoskeleton rearrangement in neurons. *Bioarchitecture, 3*(4), 113-118. doi:10.4161/bioa.26497

Anthonsen, M. W., Ronnstrand, L., Wernstedt, C., Degerman, E., & Holm, C. (1998). Identification of novel phosphorylation sites in hormone-sensitive lipase that are phosphorylated in response to isoproterenol and govern activation properties in vitro. *J Biol Chem, 273*(1), 215-221. doi:10.1074/jbc.273.1.215

Baffi, T. R., Lorden, G., Wozniak, J. M., Feichtner, A., Yeung, W., Kornev, A. P., . . . Newton, A. C. (2021). mTORC2 controls the activity of PKC and Akt by phosphorylating a conserved TOR interaction motif. *Sci Signal, 14*(678). doi:10.1126/scisignal.abe4509

Bandyopadhyay, G., Sajan, M. P., Kanoh, Y., Standaert, M. L., Quon, M. J., Lea-Currie, R., . . . Farese, R. V. (2002). PKC-zeta mediates insulin effects on glucose transport in cultured preadipocyte-derived human adipocytes. *J Clin Endocrinol Metab, 87*(2), 716-723. doi:10.1210/jcem.87.2.8252

Bandyopadhyay, G., Standaert, M. L., Zhao, L., Yu, B., Avignon, A., Galloway, L., . . . Farese, R. V. (1997). Activation of protein kinase C (alpha, beta, and zeta) by insulin in 3T3/L1 cells. Transfection studies suggest a role for PKC-zeta in glucose transport. *J Biol Chem, 272*(4), 2551-2558. doi:10.1074/jbc.272.4.2551

Bartness, T. J., Liu, Y., Shrestha, Y. B., & Ryu, V. (2014). Neural innervation of white adipose tissue and the control of lipolysis. *Front Neuroendocrinol, 35*(4), 473-493. doi:10.1016/j.yfrne.2014.04.001

Bartness, T. J., Shrestha, Y. B., Vaughan, C. H., Schwartz, G. J., & Song, C. K. (2010). Sensory and sympathetic nervous system control of white adipose tissue lipolysis. *Mol Cell Endocrinol, 318*(1-2), 34-43. doi:10.1016/j.mce.2009.08.031

Battaglioni, S., Benjamin, D., Wälchli, M., Maier, T., & Hall, M. N. (2022). mTOR substrate phosphorylation in growth control. *Cell*.

Bentzinger, C. F., Romanino, K., Cloetta, D., Lin, S., Mascarenhas, J. B., Oliveri, F., . . . Ruegg, M. A. (2008). Skeletal muscle-specific ablation of raptor, but not of rictor, causes metabolic changes and results in muscle dystrophy. *Cell Metab, 8*(5), 411-424. doi:10.1016/j.cmet.2008.10.002

Betz, C., & Hall, M. N. (2013). Where is mTOR and what is it doing there? *J Cell Biol, 203*(4), 563-574. doi:10.1083/jcb.201306041

Betz, C., Stracka, D., Prescianotto-Baschong, C., Frieden, M., Demaurex, N., & Hall, M. N. (2013). Feature Article: mTOR complex 2-Akt signaling at mitochondria-associated endoplasmic reticulum membranes (MAM) regulates mitochondrial physiology. *Proc Natl Acad Sci U S A, 110*(31), 12526-12534. doi:10.1073/pnas.1302455110

Biggs, W. H., 3rd, Meisenhelder, J., Hunter, T., Cavenee, W. K., & Arden, K. C. (1999). Protein kinase B/Akt-mediated phosphorylation promotes nuclear exclusion of the winged helix transcription factor FKHR1. *Proc Natl Acad Sci U S A, 96*(13), 7421-7426. doi:10.1073/pnas.96.13.7421

Birsoy, K., Berry, R., Wang, T., Ceyhan, O., Tavazoie, S., Friedman, J. M., & Rodeheffer, M. S. (2011). Analysis of gene networks in white adipose tissue development reveals a role for ETS2 in adipogenesis. *Development, 138*(21), 4709-4719. doi:10.1242/dev.067710

Blaszkiewicz, M., Willows, J. W., Dubois, A. L., Waible, S., DiBello, K., Lyons, L. L., . . . Townsend, K. L. (2019). Neuropathy and neural plasticity in the subcutaneous white adipose depot. *PLoS One, 14*(9), e0221766. doi:10.1371/journal.pone.0221766

Blaszkiewicz, M., Willows, J. W., Johnson, C. P., & Townsend, K. L. (2019). The Importance of Peripheral Nerves in Adipose Tissue for the Regulation of Energy Balance. *Biology (Basel), 8*(1). doi:10.3390/biology8010010

Bluher, M., & Mantzoros, C. S. (2015). From leptin to other adipokines in health and disease: facts and expectations at the beginning of the 21st century. *Metabolism, 64*(1), 131-145. doi:10.1016/j.metabol.2014.10.016

Cao, Y., Wang, H., Wang, Q., Han, X., & Zeng, W. (2018). Three-dimensional volume fluorescence-imaging of vascular plasticity in adipose tissues. *Mol Metab, 14*, 71-81. doi:10.1016/j.molmet.2018.06.004

Cao, Y., Wang, H., & Zeng, W. (2018). Whole-tissue 3D imaging reveals intra-adipose sympathetic plasticity regulated by NGF-TrkA signal in cold-induced beiging. *Protein Cell, 9*(6), 527-539. doi:10.1007/s13238-018-0528-5

Castellano, E., & Downward, J. (2011). RAS Interaction with PI3K: More Than Just Another Effector Pathway. *Genes Cancer, 2*(3), 261-274. doi:10.1177/1947601911408079

Castro, E., Vieira, T. S., Oliveira, T. E., Ortiz-Silva, M., Andrade, M. L., Tomazelli, C. A., . . . Festuccia, W. T. (2021). Adipocyte-specific mTORC2 deficiency impairs BAT and iWAT thermogenic capacity without affecting glucose uptake and energy expenditure in cold-acclimated mice. *Am J Physiol Endocrinol Metab, 321*(5), E592-E605. doi:10.1152/ajpendo.00587.2020

Chellappa, K., Brinkman, J. A., Mukherjee, S., Morrison, M., Alotaibi, M. I., Carbajal, K. A., . . . Lamming, D. W. (2019). Hypothalamic mTORC2 is essential for metabolic health and longevity. *Aging Cell, 18*(5), e13014. doi:10.1111/acel.13014

Chi, J., Crane, A., Wu, Z., & Cohen, P. (2018). Adipo-Clear: A Tissue Clearing Method for Three-Dimensional Imaging of Adipose Tissue. *J Vis Exp*(137). doi:10.3791/58271

Chi, J., Wu, Z., Choi, C. H. J., Nguyen, L., Tegegne, S., Ackerman, S. E., . . . Cohen, P. (2018). Three-Dimensional Adipose Tissue Imaging Reveals Regional Variation in Beige Fat Biogenesis and PRDM16-Dependent Sympathetic Neurite Density. *Cell Metab, 27*(1), 226-236 e223. doi:10.1016/j.cmet.2017.12.011

Cohen, P., & Kajimura, S. (2021). The cellular and functional complexity of thermogenic fat. *Nat Rev Mol Cell Biol, 22*(6), 393-409. doi:10.1038/s41580-021-00350-0

Collins, S. (2011). beta-Adrenoceptor Signaling Networks in Adipocytes for Recruiting Stored Fat and Energy Expenditure. *Front Endocrinol (Lausanne), 2*, 102. doi:10.3389/fendo.2011.00102

Corvera, S. (2021). Cellular Heterogeneity in Adipose Tissues. *Annu Rev Physiol, 83*, 257-278. doi:10.1146/annurev-physiol-031620-095446

Cummings, N. E., & Lamming, D. W. (2017). Regulation of metabolic health and aging by nutrient-sensitive signaling pathways. *Mol Cell Endocrinol, 455*, 13-22. doi:10.1016/j.mce.2016.11.014

Cybulski, N., Polak, P., Auwerx, J., Ruegg, M. A., & Hall, M. N. (2009). mTOR complex 2 in adipose tissue negatively controls whole-body growth. *Proc Natl Acad Sci U S A, 106*(24), 9902-9907. doi:10.1073/pnas.0811321106

DeFronzo, R. A., Ferrannini, E., Sato, Y., Felig, P., & Wahren, J. (1981). Synergistic interaction between exercise and insulin on peripheral glucose uptake. *J Clin Invest, 68*(6), 1468-1474. doi:10.1172/jci110399

Dong, Q., Giorgianni, F., Beranova-Giorgianni, S., Deng, X., O'Meally, R. N., Bridges, D., . . . Raghow, R. (2015). Glycogen synthase kinase-3-mediated phosphorylation of serine 73 targets sterol response element binding protein-1c (SREBP-1c) for proteasomal degradation. *Biosci Rep, 36*(1), e00284. doi:10.1042/BSR20150234

Donnelly, K. L., Smith, C. I., Schwarzenberg, S. J., Jessurun, J., Boldt, M. D., & Parks, E. J. (2005). Sources of fatty acids stored in liver and secreted via lipoproteins in patients with nonalcoholic fatty liver disease. *J Clin Invest, 115*(5), 1343-1351. doi:10.1172/JCI23621

Duncan, R. E., Ahmadian, M., Jaworski, K., Sarkadi-Nagy, E., & Sul, H. S. (2007). Regulation of lipolysis in adipocytes. *Annu Rev Nutr, 27*, 79-101. doi:10.1146/annurev.nutr.27.061406.093734

Ebner, M., Sinkovics, B., Szczygiel, M., Ribeiro, D. W., & Yudushkin, I. (2017). Localization of mTORC2 activity inside cells. *J Cell Biol, 216*(2), 343-353. doi:10.1083/jcb.201610060

Facchinetti, V., Ouyang, W., Wei, H., Soto, N., Lazorchak, A., Gould, C., . . . Jacinto, E. (2008). The mammalian target of rapamycin complex 2 controls folding and stability of Akt and protein kinase C. *EMBO J, 27*(14), 1932-1943. doi:10.1038/emboj.2008.120

Fantini, F., & Johansson, O. (1992). Expression of growth-associated protein 43 and nerve growth factor receptor in human skin: a comparative immunohistochemical investigation. *J Invest Dermatol, 99*(6), 734-742. doi:10.1111/1523-1747.ep12614465

Farr, O. M., Gavrieli, A., & Mantzoros, C. S. (2015). Leptin applications in 2015: what have we learned about leptin and obesity? *Curr Opin Endocrinol Diabetes Obes, 22*(5), 353-359. doi:10.1097/MED.0000000000000184

Fasshauer, M., & Bluher, M. (2015). Adipokines in health and disease. *Trends Pharmacol Sci, 36*(7), 461-470. doi:10.1016/j.tips.2015.04.014

Ferguson, D., & Finck, B. N. (2021). Emerging therapeutic approaches for the treatment of NAFLD and type 2 diabetes mellitus. *Nat Rev Endocrinol, 17*(8), 484-495. doi:10.1038/s41574-021-00507-z

Foster, D. W., & Bloom, B. (1963). The synthesis of fatty acids by rat liver slices in tritiated water. *J Biol Chem, 238*, 888-892. Retrieved from https://www.ncbi.nlm.nih.gov/pubmed/13958891

Foster, M. T., & Bartness, T. J. (2006). Sympathetic but not sensory denervation stimulates white adipocyte proliferation. *Am J Physiol Regul Integr Comp Physiol, 291*(6), R1630-1637. doi:10.1152/ajpregu.00197.2006

Frias, M. A., Thoreen, C. C., Jaffe, J. D., Schroder, W., Sculley, T., Carr, S. A., & Sabatini, D. M. (2006). mSin1 is necessary for Akt/PKB phosphorylation, and its isoforms define three distinct mTORC2s. *Curr Biol, 16*(18), 1865-1870. doi:10.1016/j.cub.2006.08.001

Friedman, J. M. (2019). Leptin and the endocrine control of energy balance. *Nat Metab, 1*(8), 754-764. doi:10.1038/s42255-019-0095-y

Fu, W., & Hall, M. N. (2020). Regulation of mTORC2 Signaling. *Genes (Basel), 11*(9). doi:10.3390/genes11091045

Funcke, J. B., & Scherer, P. E. (2019). Beyond adiponectin and leptin: adipose tissue-derived mediators of inter-organ communication. *J Lipid Res, 60*(10), 1648-1684. doi:10.1194/jlr.R094060

Galarraga, M., Campion, J., Munoz-Barrutia, A., Boque, N., Moreno, H., Martinez, J. A., . . . Ortiz-de-Solorzano, C. (2012). Adiposoft: automated software for the analysis of white adipose tissue cellularity in histological sections. *J Lipid Res, 53*(12), 2791-2796. doi:10.1194/jlr.D023788

Gan, X., Wang, J., Wang, C., Sommer, E., Kozasa, T., Srinivasula, S., . . . Wu, D. (2012). PRR5L degradation promotes mTORC2-mediated PKC-delta phosphorylation and cell migration downstream of Galpha12. *Nat Cell Biol, 14*(7), 686-696. doi:10.1038/ncb2507

Garcia-Martinez, J. M., & Alessi, D. R. (2008). mTOR complex 2 (mTORC2) controls hydrophobic motif phosphorylation and activation of serum- and glucocorticoid-induced protein kinase 1 (SGK1). *Biochem J, 416*(3), 375-385. doi:10.1042/BJ20081668

Garretson, J. T., Szymanski, L. A., Schwartz, G. J., Xue, B., Ryu, V., & Bartness, T. J. (2016). Lipolysis sensation by white fat afferent nerves triggers brown fat thermogenesis. *Mol Metab, 5*(8), 626-634. doi:10.1016/j.molmet.2016.06.013

Gaubitz, C., Prouteau, M., Kusmider, B., & Loewith, R. (2016). TORC2 Structure and Function. *Trends Biochem Sci, 41*(6), 532-545. doi:10.1016/j.tibs.2016.04.001

Giordano, A., Morroni, M., Santone, G., Marchesi, G. F., & Cinti, S. (1996). Tyrosine hydroxylase, neuropeptide Y, substance P, calcitonin gene-related peptide and vasoactive intestinal peptide in nerves of rat periovarian adipose tissue: an immunohistochemical and ultrastructural investigation. *J Neurocytol, 25*(2), 125-136. doi:10.1007/BF02284791

Grabner, G. F., Xie, H., Schweiger, M., & Zechner, R. (2021). Lipolysis: cellular mechanisms for lipid mobilization from fat stores. *Nat Metab, 3*(11), 1445-1465. doi:10.1038/s42255-021-00493-6

Guilherme, A., Henriques, F., Bedard, A. H., & Czech, M. P. (2019). Molecular pathways linking adipose innervation to insulin action in obesity and diabetes mellitus. *Nat Rev Endocrinol, 15*(4), 207-225. doi:10.1038/s41574-019-0165-y

Guilherme, A., Pedersen, D. J., Henriques, F., Bedard, A. H., Henchey, E., Kelly, M., . . . Czech, M. P. (2018). Neuronal modulation of brown adipose activity through perturbation of white adipocyte lipogenesis. *Mol Metab, 16*, 116-125. doi:10.1016/j.molmet.2018.06.014

Guri, Y., Colombi, M., Dazert, E., Hindupur, S. K., Roszik, J., Moes, S., . . . Hall, M. N. (2017). mTORC2 Promotes Tumorigenesis via Lipid Synthesis. *Cancer Cell, 32*(6), 807-823 e812. doi:10.1016/j.ccell.2017.11.011

Hagiwara, A., Cornu, M., Cybulski, N., Polak, P., Betz, C., Trapani, F., . . . Hall, M. N. (2012). Hepatic mTORC2 activates glycolysis and lipogenesis through Akt, glucokinase, and SREBP1c. *Cell Metab, 15*(5), 725-738. doi:10.1016/j.cmet.2012.03.015

Hajri, T., & Abumrad, N. A. (2002). Fatty acid transport across membranes: relevance to nutrition and metabolic pathology. *Annu Rev Nutr, 22*, 383-415. doi:10.1146/annurev.nutr.22.020402.130846

Han, H. S., Kang, G., Kim, J. S., Choi, B. H., & Koo, S. H. (2016). Regulation of glucose metabolism from a liver-centric perspective. *Exp Mol Med, 48*, e218. doi:10.1038/emm.2015.122

Hatting, M., Tavares, C. D. J., Sharabi, K., Rines, A. K., & Puigserver, P. (2018). Insulin regulation of gluconeogenesis. *Ann N Y Acad Sci, 1411*(1), 21-35. doi:10.1111/nyas.13435

Haugen, F., & Drevon, C. A. (2007). The interplay between nutrients and the adipose tissue. *Proc Nutr Soc, 66*(2), 171-182. doi:10.1017/S0029665107005423

Hegarty, B. D., Bobard, A., Hainault, I., Ferre, P., Bossard, P., & Foufelle, F. (2005). Distinct roles of insulin and liver X receptor in the induction and cleavage of sterol regulatory element-binding protein-1c. *Proc Natl Acad Sci U S A, 102*(3), 791-796. doi:10.1073/pnas.0405067102

Heitman, J., Movva, N. R., & Hall, M. N. (1991). Targets for cell cycle arrest by the immunosuppressant rapamycin in yeast. *Science, 253*(5022), 905-909. doi:10.1126/science.1715094

Hellerstein, M. K., Christiansen, M., Kaempfer, S., Kletke, C., Wu, K., Reid, J. S., . . . Shackleton, C. H. (1991). Measurement of de novo hepatic lipogenesis in humans using stable isotopes. *J Clin Invest, 87*(5), 1841-1852. doi:10.1172/JCI115206

Herman, M. A., Peroni, O. D., Villoria, J., Schon, M. R., Abumrad, N. A., Bluher, M., . . . Kahn, B. B. (2012). A novel ChREBP isoform in adipose tissue regulates systemic glucose metabolism. *Nature, 484*(7394), 333-338. doi:10.1038/nature10986

Hong, K. Y., Bae, H., Park, I., Park, D. Y., Kim, K. H., Kubota, Y., . . . Koh, G. Y. (2015). Perilipin+ embryonic preadipocytes actively proliferate along growing vasculatures for adipose expansion. *Development, 142*(15), 2623-2632. doi:10.1242/dev.125336

Hsiao, W. Y., Jung, S. M., Tang, Y., Haley, J. A., Li, R., Li, H., . . . Guertin, D. A. (2020). The Lipid Handling Capacity of Subcutaneous Fat Is Programmed by mTORC2 during Development. *Cell Rep, 33*(1), 108223. doi:10.1016/j.celrep.2020.108223

Huang da, W., Sherman, B. T., & Lempicki, R. A. (2009). Systematic and integrative analysis of large gene lists using DAVID bioinformatics resources. *Nat Protoc, 4*(1), 44-57. doi:10.1038/nprot.2008.211

Ikenoue, T., Inoki, K., Yang, Q., Zhou, X., & Guan, K. L. (2008). Essential function of TORC2 in PKC and Akt turn motif phosphorylation, maturation and signalling. *EMBO J, 27*(14), 1919-1931. doi:10.1038/emboj.2008.119

Jacinto, E., Loewith, R., Schmidt, A., Lin, S., Ruegg, M. A., Hall, A., & Hall, M. N. (2004). Mammalian TOR complex 2 controls the actin cytoskeleton and is rapamycin insensitive. *Nat Cell Biol, 6*(11), 1122-1128. doi:10.1038/ncb1183

Jiang, H., Ding, X., Cao, Y., Wang, H., & Zeng, W. (2017). Dense Intra-adipose Sympathetic Arborizations Are Essential for Cold-Induced Beiging of Mouse White Adipose Tissue. *Cell Metab, 26*(4), 686-692 e683. doi:10.1016/j.cmet.2017.08.016

Jung, S. M., Hung, C. M., Hildebrand, S. R., Sanchez-Gurmaches, J., Martinez-Pastor, B., Gengatharan, J. M., . . . Guertin, D. A. (2019). Non-canonical mTORC2 Signaling Regulates Brown Adipocyte Lipid Catabolism through SIRT6-FoxO1. *Mol Cell, 75*(4), 807-822 e808. doi:10.1016/j.molcel.2019.07.023

Keenan, C., & Kelleher, D. (1998). Protein kinase C and the cytoskeleton. *Cell Signal, 10*(4), 225-232. doi:10.1016/s0898-6568(97)00121-6

Kleinert, M., Parker, B. L., Chaudhuri, R., Fazakerley, D. J., Serup, A., Thomas, K. C., . . . Richter, E. A. (2016). mTORC2 and AMPK differentially regulate muscle triglyceride content via Perilipin 3. *Mol Metab, 5*(8), 646-655. doi:10.1016/j.molmet.2016.06.007

Kleinert, M., Parker, B. L., Fritzen, A. M., Knudsen, J. R., Jensen, T. E., Kjobsted, R., . . . Richter, E. A. (2017). Mammalian target of rapamycin complex 2 regulates muscle glucose uptake during exercise in mice. *J Physiol, 595*(14), 4845-4855. doi:10.1113/JP274203

Knudsen, J. R., Fritzen, A. M., James, D. E., Jensen, T. E., Kleinert, M., & Richter, E. A. (2020). Growth Factor-Dependent and -Independent Activation of mTORC2. *Trends Endocrinol Metab, 31*(1), 13-24. doi:10.1016/j.tem.2019.09.005

Kobayashi, M., & Zochodne, D. W. (2018). Diabetic neuropathy and the sensory neuron: New aspects of pathogenesis and their treatment implications. *J Diabetes Investig, 9*(6), 1239-1254. doi:10.1111/jdi.12833

Kocalis, H. E., Hagan, S. L., George, L., Turney, M. K., Siuta, M. A., Laryea, G. N., . . . Niswender, K. D. (2014). Rictor/mTORC2 facilitates central regulation of energy and glucose homeostasis. *Mol Metab, 3*(4), 394-407. doi:10.1016/j.molmet.2014.01.014

Kovalski, J. R., Bhaduri, A., Zehnder, A. M., Neela, P. H., Che, Y., Wozniak, G. G., & Khavari, P. A. (2019). The Functional Proximal Proteome of Oncogenic Ras Includes mTORC2. *Mol Cell, 73*(4), 830-844 e812. doi:10.1016/j.molcel.2018.12.001

Kumar, A., Harris, T. E., Keller, S. R., Choi, K. M., Magnuson, M. A., & Lawrence, J. C., Jr. (2008). Muscle-specific deletion of rictor impairs insulin-stimulated glucose transport and enhances Basal glycogen synthase activity. *Mol Cell Biol, 28*(1), 61-70. doi:10.1128/MCB.01405-07

Kumar, A., Lawrence, J. C., Jr., Jung, D. Y., Ko, H. J., Keller, S. R., Kim, J. K., . . . Harris, T. E. (2010). Fat cell-specific ablation of rictor in mice impairs insulin-regulated fat cell and whole-body glucose and lipid metabolism. *Diabetes, 59*(6), 1397-1406. doi:10.2337/db09-1061

Kunz, J., Henriquez, R., Schneider, U., Deuter-Reinhard, M., Movva, N. R., & Hall, M. N. (1993). Target of rapamycin in yeast, TOR2, is an essential phosphatidylinositol kinase homolog required for G1 progression. *Cell, 73*(3), 585-596. doi:10.1016/0092-8674(93)90144-f

Kwok, K. H., Lam, K. S., & Xu, A. (2016). Heterogeneity of white adipose tissue: molecular basis and clinical implications. *Exp Mol Med, 48*, e215. doi:10.1038/emm.2016.5

Lamming, D. W., Ye, L., Katajisto, P., Goncalves, M. D., Saitoh, M., Stevens, D. M., . . . Baur, J. A. (2012). Rapamycin-induced insulin resistance is mediated by mTORC2 loss and uncoupled from longevity. *Science, 335*(6076), 1638-1643. doi:10.1126/science.1215135

Lee, B. J., Boyer, J. A., Burnett, G. L., Thottumkara, A. P., Tibrewal, N., Wilson, S. L., . . . Rosen, N. (2021). Author Correction: Selective inhibitors of mTORC1 activate 4EBP1 and suppress tumor growth. *Nat Chem Biol, 17*(8), 925. doi:10.1038/s41589-021-00843-1

Lim, K., Haider, A., Adams, C., Sleigh, A., & Savage, D. B. (2021). Lipodistrophy: a paradigm for understanding the consequences of "overloading" adipose tissue. *Physiol Rev, 101*(3), 907-993. doi:10.1152/physrev.00032.2020

Lin, Chun, T. H., & Kang, L. (2016). Adipose extracellular matrix remodelling in obesity and insulin resistance. *Biochem Pharmacol, 119*, 8-16. doi:10.1016/j.bcp.2016.05.005

Liu, G. Y., & Sabatini, D. M. (2020). mTOR at the nexus of nutrition, growth, ageing and disease. *Nat Rev Mol Cell Biol, 21*(4), 183-203. doi:10.1038/s41580-019-0199-y

Liu, P., Gan, W., Chin, Y. R., Ogura, K., Guo, J., Zhang, J., . . . Wei, W. (2015). PtdIns(3,4,5)P3-Dependent Activation of the mTORC2 Kinase Complex. *Cancer Discov, 5*(11), 1194-1209. doi:10.1158/2159-8290.CD-15-0460

Liu, T., Kamiyoshi, A., Sakurai, T., Ichikawa-Shindo, Y., Kawate, H., Yang, L., . . . Shindo, T. (2017). Endogenous Calcitonin Gene-Related Peptide Regulates Lipid Metabolism and Energy Homeostasis in Male Mice. *Endocrinology, 158*(5), 1194-1206. doi:10.1210/en.2016-1510

Loewith, R., Jacinto, E., Wullschleger, S., Lorberg, A., Crespo, J. L., Bonenfant, D., . . . Hall, M. N. (2002). Two TOR complexes, only one of which is rapamycin sensitive, have distinct roles in cell growth control. *Mol Cell, 10*(3), 457-468. doi:10.1016/s1097-2765(02)00636-6

Longo, M., Zatterale, F., Naderi, J., Parrillo, L., Formisano, P., Raciti, G. A., . . . Miele, C. (2019). Adipose Tissue Dysfunction as Determinant of Obesity-Associated Metabolic Complications. *Int J Mol Sci, 20*(9). doi:10.3390/ijms20092358

Magnusson, I., Rothman, D. L., Katz, L. D., Shulman, R. G., & Shulman, G. I. (1992). Increased rate of gluconeogenesis in type II diabetes mellitus. A 13C nuclear magnetic resonance study. *J Clin Invest, 90*(4), 1323-1327. doi:10.1172/JCI115997

Makwana, K., Chodavarapu, H., Morones, N., Chi, J., Barr, W., Novinbakht, E., . . . Riera, C. E. (2021). Sensory neurons expressing calcitonin gene-related peptide alpha regulate adaptive thermogenesis and diet-induced obesity. *Mol Metab, 45*, 101161. doi:10.1016/j.molmet.2021.101161

Manning, B. D., & Toker, A. (2017). AKT/PKB Signaling: Navigating the Network. *Cell, 169*(3), 381-405. doi:10.1016/j.cell.2017.04.001

Martinez Calejman, C., Trefely, S., Entwisle, S. W., Luciano, A., Jung, S. M., Hsiao, W., . . . Guertin, D. A. (2020). mTORC2-AKT signaling to ATP-citrate lyase drives brown adipogenesis and de novo lipogenesis. *Nat Commun, 11*(1), 575. doi:10.1038/s41467-020-14430-w

McCabe, M. P., Cullen, E. R., Barrows, C. M., Shore, A. N., Tooke, K. I., Laprade, K. A., . . . Weston, M. C. (2020). Genetic inactivation of mTORC1 or mTORC2 in neurons reveals distinct functions in glutamatergic synaptic transmission. *Elife, 9*. doi:10.7554/eLife.51440

Mueckler, M., & Thorens, B. (2013). The SLC2 (GLUT) family of membrane transporters. *Mol Aspects Med, 34*(2-3), 121-138. doi:10.1016/j.mam.2012.07.001

Murphy, E. J. (2006). Stable isotope methods for the in vivo measurement of lipogenesis and triglyceride metabolism. *J Anim Sci, 84 Suppl*, E94-104. doi:10.2527/2006.8413_supple94x

Murphy, K. T., Schwartz, G. J., Nguyen, N. L., Mendez, J. M., Ryu, V., & Bartness, T. J. (2013). Leptin-sensitive sensory nerves innervate white fat. *Am J Physiol Endocrinol Metab, 304*(12), E1338-1347. doi:10.1152/ajpendo.00021.2013

Murray, J. T., Campbell, D. G., Morrice, N., Auld, G. C., Shpiro, N., Marquez, R., . . . Cohen, P. (2004). Exploitation of KESTREL to identify NDRG family members as physiological substrates for SGK1 and GSK3. *Biochem J, 384*(Pt 3), 477-488. doi:10.1042/BJ20041057

Nakanishi, H., Brewer, K. A., & Exton, J. H. (1993). Activation of the zeta isozyme of protein kinase C by phosphatidylinositol 3,4,5-trisphosphate. *J Biol Chem, 268*(1), 13-16. Retrieved from https://www.ncbi.nlm.nih.gov/pubmed/8380153

Nedvidkova, J., Smitka, K., Kopsky, V., & Hainer, V. (2005). Adiponectin, an adipocyte-derived protein. *Physiol Res, 54*(2), 133-140. Retrieved from https://www.ncbi.nlm.nih.gov/pubmed/15544426

Niijima, A. (1998). Afferent signals from leptin sensors in the white adipose tissue of the epididymis, and their reflex effect in the rat. *J Auton Nerv Syst, 73*(1), 19-25. doi:10.1016/s0165-1838(98)00109-x

Nordlie, R. C., Foster, J. D., & Lange, A. J. (1999). Regulation of glucose production by the liver. *Annu Rev Nutr, 19*, 379-406. doi:10.1146/annurev.nutr.19.1.379

Oh, W. J., Wu, C. C., Kim, S. J., Facchinetti, V., Julien, L. A., Finlan, M., . . . Jacinto, E. (2010). mTORC2 can associate with ribosomes to promote cotranslational phosphorylation and stability of nascent Akt polypeptide. *EMBO J, 29*(23), 3939-3951. doi:10.1038/emboj.2010.271

Pepino, M. Y., Kuda, O., Samovski, D., & Abumrad, N. A. (2014). Structure-function of CD36 and importance of fatty acid signal transduction in fat metabolism. *Annu Rev Nutr, 34*, 281-303. doi:10.1146/annurev-nutr-071812-161220

Pilkis, S. J., & Claus, T. H. (1991). Hepatic gluconeogenesis/glycolysis: regulation and structure/function relationships of substrate cycle enzymes. *Annu Rev Nutr, 11*, 465-515. doi:10.1146/annurev.nu.11.070191.002341

Pilkis, S. J., el-Maghrabi, M. R., & Claus, T. H. (1988). Hormonal regulation of hepatic gluconeogenesis and glycolysis. *Annu Rev Biochem, 57*, 755-783. doi:10.1146/annurev.bi.57.070188.003543

Post, H., Penning, R., Fitzpatrick, M. A., Garrigues, L. B., Wu, W., MacGillavry, H. D., . . . Altelaar, A. F. (2017). Robust, Sensitive, and Automated Phosphopeptide Enrichment Optimized for Low Sample Amounts Applied to Primary Hippocampal Neurons. *J Proteome Res, 16*(2), 728-737. doi:10.1021/acs.jproteome.6b00753

Postic, C., Dentin, R., Denechaud, P. D., & Girard, J. (2007). ChREBP, a transcriptional regulator of glucose and lipid metabolism. *Annu Rev Nutr, 27*, 179-192. doi:10.1146/annurev.nutr.27.061406.093618

Qiang, G., Whang Kong, H., Xu, S., Pham, H. A., Parlee, S. D., Burr, A. A., . . . Liew, C. W. (2016). Lipodystrophy and severe metabolic dysfunction in mice with adipose tissue-specific insulin receptor ablation. *Mol Metab, 5*(7), 480-490. doi:10.1016/j.molmet.2016.05.005

Rada, P., Gonzalez-Rodriguez, A., Garcia-Monzon, C., & Valverde, A. M. (2020). Understanding lipotoxicity in NAFLD pathogenesis: is CD36 a key driver? *Cell Death Dis, 11*(9), 802. doi:10.1038/s41419-020-03003-w

Rochford, J. J. (2014). Mouse models of lipodystrophy and their significance in understanding fat regulation. *Curr Top Dev Biol, 109*, 53-96. doi:10.1016/B978-0-12-397920-9.00005-6

Rosen, E. D., & Spiegelman, B. M. (2006). Adipocytes as regulators of energy balance and glucose homeostasis. *Nature, 444*(7121), 847-853. doi:10.1038/nature05483

Saci, A., Cantley, L. C., & Carpenter, C. L. (2011). Rac1 regulates the activity of mTORC1 and mTORC2 and controls cellular size. *Mol Cell, 42*(1), 50-61. doi:10.1016/j.molcel.2011.03.017

Sakaguchi, M., Fujisaka, S., Cai, W., Winnay, J. N., Konishi, M., O'Neill, B. T., . . . Kahn, C. R. (2017). Adipocyte Dynamics and Reversible Metabolic Syndrome in Mice with an Inducible Adipocyte-Specific Deletion of the Insulin Receptor. *Cell Metab, 25*(2), 448-462. doi:10.1016/j.cmet.2016.12.008

Sanders, F. W., & Griffin, J. L. (2016). De novo lipogenesis in the liver in health and disease: more than just a shunting yard for glucose. *Biol Rev Camb Philos Soc, 91*(2), 452-468. doi:10.1111/brv.12178

Sarbassov, D. D., Ali, S. M., Kim, D. H., Guertin, D. A., Latek, R. R., Erdjument-Bromage, H., . . . Sabatini, D. M. (2004). Rictor, a novel binding partner of mTOR, defines a

rapamycin-insensitive and raptor-independent pathway that regulates the cytoskeleton. *Curr Biol, 14*(14), 1296-1302. doi:10.1016/j.cub.2004.06.054

Sarbassov, D. D., Guertin, D. A., Ali, S. M., & Sabatini, D. M. (2005). Phosphorylation and regulation of Akt/PKB by the rictor-mTOR complex. *Science, 307*(5712), 1098-1101. doi:10.1126/science.1106148

Sassmann, A., Offermanns, S., & Wettschureck, N. (2010). Tamoxifen-inducible Cre-mediated recombination in adipocytes. *Genesis, 48*(10), 618-625. doi:10.1002/dvg.20665

Savage, D. B., & O'Rahilly, S. (2002). Leptin: a novel therapeutic role in lipodystrophy. *J Clin Invest, 109*(10), 1285-1286. doi:10.1172/JCI15326

Scaiola, A., Mangia, F., Imseng, S., Boehringer, D., Berneiser, K., Shimobayashi, M., . . . Maier, T. (2020). The 3.2-A resolution structure of human mTORC2. *Sci Adv, 6*(45). doi:10.1126/sciadv.abc1251

Scherer, P. E., Williams, S., Fogliano, M., Baldini, G., & Lodish, H. F. (1995). A novel serum protein similar to C1q, produced exclusively in adipocytes. *J Biol Chem, 270*(45), 26746-26749. doi:10.1074/jbc.270.45.26746

Schmidt, R. E., Spencer, S. A., Coleman, B. D., & Roth, K. A. (1991). Immunohistochemical localization of GAP-43 in rat and human sympathetic nervous system--effects of aging and diabetes. *Brain Res, 552*(2), 190-197. doi:10.1016/0006-8993(91)90083-8

Schreiber, K. H., Arriola Apelo, S. I., Yu, D., Brinkman, J. A., Velarde, M. C., Syed, F. A., . . . Lamming, D. W. (2019). A novel rapamycin analog is highly selective for mTORC1 in vivo. *Nat Commun, 10*(1), 3194. doi:10.1038/s41467-019-11174-0

Schroder, W. A., Buck, M., Cloonan, N., Hancock, J. F., Suhrbier, A., Sculley, T., & Bushell, G. (2007). Human Sin1 contains Ras-binding and pleckstrin homology domains and suppresses Ras signalling. *Cell Signal, 19*(6), 1279-1289. doi:10.1016/j.cellsig.2007.01.013

Sekiya, M., Yahagi, N., Matsuzaka, T., Takeuchi, Y., Nakagawa, Y., Takahashi, H., . . . Shimano, H. (2007). SREBP-1-independent regulation of lipogenic gene expression in adipocytes. *J Lipid Res, 48*(7), 1581-1591. doi:10.1194/jlr.M700033-JLR200

Shearin, A. L., Monks, B. R., Seale, P., & Birnbaum, M. J. (2016). Lack of AKT in adipocytes causes severe lipodystrophy. *Mol Metab, 5*(7), 472-479. doi:10.1016/j.molmet.2016.05.006

Shimobayashi, M., Albert, V., Woelnerhanssen, B., Frei, I. C., Weissenberger, D., Meyer-Gerspach, A. C., . . . Hall, M. N. (2018). Insulin resistance causes inflammation in adipose tissue. *J Clin Invest, 128*(4), 1538-1550. doi:10.1172/JCI96139

Shin, H., Ma, Y., Chanturiya, T., Cao, Q., Wang, Y., Kadegowda, A. K. G., . . . Yu, L. (2017). Lipolysis in Brown Adipocytes Is Not Essential for Cold-Induced Thermogenesis in Mice. *Cell Metab, 26*(5), 764-777 e765. doi:10.1016/j.cmet.2017.09.002

Shinde, A. B., Song, A., & Wang, Q. A. (2021). Brown Adipose Tissue Heterogeneity, Energy Metabolism, and Beyond. *Front Endocrinol (Lausanne), 12*, 651763. doi:10.3389/fendo.2021.651763

Snipes, G. J., Chan, S. Y., McGuire, C. B., Costello, B. R., Norden, J. J., Freeman, J. A., & Routtenberg, A. (1987). Evidence for the coidentification of GAP-43, a growth-associated protein, and F1, a plasticity-associated protein. *J Neurosci, 7*(12), 4066-4075. Retrieved from https://www.ncbi.nlm.nih.gov/pubmed/3694262

Song, C. K., Schwartz, G. J., & Bartness, T. J. (2009). Anterograde transneuronal viral tract tracing reveals central sensory circuits from white adipose tissue. *Am J Physiol Regul Integr Comp Physiol, 296*(3), R501-511. doi:10.1152/ajpregu.90786.2008

Stuttfeld, E., Aylett, C. H., Imseng, S., Boehringer, D., Scaiola, A., Sauer, E., . . . Ban, N. (2018). Architecture of the human mTORC2 core complex. *Elife, 7*. doi:10.7554/eLife.33101

Tainaka, K., Murakami, T. C., Susaki, E. A., Shimizu, C., Saito, R., Takahashi, K., . . . Ueda, H. R. (2018). Chemical Landscape for Tissue Clearing Based on Hydrophilic Reagents. *Cell Rep, 24*(8), 2196-2210 e2199. doi:10.1016/j.celrep.2018.07.056

Tan, C. Y., & Vidal-Puig, A. (2008). Adipose tissue expandability: the metabolic problems of obesity may arise from the inability to become more obese. *Biochem Soc Trans, 36*(Pt 5), 935-940. doi:10.1042/BST0360935

Tang, Y., Wallace, M., Sanchez-Gurmaches, J., Hsiao, W. Y., Li, H., Lee, P. L., . . . Guertin, D. A. (2016). Adipose tissue mTORC2 regulates ChREBP-driven de novo lipogenesis and hepatic glucose metabolism. *Nat Commun, 7*, 11365. doi:10.1038/ncomms11365

Thomanetz, V., Angliker, N., Cloetta, D., Lustenberger, R. M., Schweighauser, M., Oliveri, F., . . . Ruegg, M. A. (2013). Ablation of the mTORC2 component rictor in brain or Purkinje cells affects size and neuron morphology. *J Cell Biol, 201*(2), 293-308. doi:10.1083/jcb.201205030

Tyanova, S., Temu, T., Sinitcyn, P., Carlson, A., Hein, M. Y., Geiger, T., . . . Cox, J. (2016). The Perseus computational platform for comprehensive analysis of (prote)omics data. *Nat Methods, 13*(9), 731-740. doi:10.1038/nmeth.3901

Urbanska, M., Gozdz, A., Swiech, L. J., & Jaworski, J. (2012). Mammalian target of rapamycin complex 1 (mTORC1) and 2 (mTORC2) control the dendritic arbor morphology of hippocampal neurons. *J Biol Chem, 287*(36), 30240-30256. doi:10.1074/jbc.M112.374405

Usoskin, D., Furlan, A., Islam, S., Abdo, H., Lonnerberg, P., Lou, D., . . . Ernfors, P. (2015). Unbiased classification of sensory neuron types by large-scale single-cell RNA sequencing. *Nat Neurosci, 18*(1), 145-153. doi:10.1038/nn.3881

van Dam, T. J., Zwartkruis, F. J., Bos, J. L., & Snel, B. (2011). Evolution of the TOR pathway. *J Mol Evol, 73*(3-4), 209-220. doi:10.1007/s00239-011-9469-9

Vaughan, C. H., Zarebidaki, E., Ehlen, J. C., & Bartness, T. J. (2014). Analysis and measurement of the sympathetic and sensory innervation of white and brown adipose tissue. *Methods Enzymol, 537*, 199-225. doi:10.1016/B978-0-12-411619-1.00011-2

Vegiopoulos, A., Rohm, M., & Herzig, S. (2017). Adipose tissue: between the extremes. *EMBO J, 36*(14), 1999-2017. doi:10.15252/embj.201696206

Walden, T. B., Hansen, I. R., Timmons, J. A., Cannon, B., & Nedergaard, J. (2012). Recruited vs. nonrecruited molecular signatures of brown, "brite," and white adipose tissues. *Am J Physiol Endocrinol Metab, 302*(1), E19-31. doi:10.1152/ajpendo.00249.2011

Wang, P., Loh, K. H., Wu, M., Morgan, D. A., Schneeberger, M., Yu, X., . . . Friedman, J. (2020). A leptin-BDNF pathway regulating sympathetic innervation of adipose tissue. *Nature, 583*(7818), 839-844. doi:10.1038/s41586-020-2527-y

Wang, Y., Yang, F., Gritsenko, M. A., Wang, Y., Clauss, T., Liu, T., . . . Smith, R. D. (2011). Reversed-phase chromatography with multiple fraction concatenation strategy for proteome profiling of human MCF10A cells. *Proteomics, 11*(10), 2019-2026. doi:10.1002/pmic.201000722

Willows, J. W., Blaszkiewicz, M., Lamore, A., Borer, S., Dubois, A. L., Garner, E., . . . Townsend, K. L. (2021). Visualization and analysis of whole depot adipose tissue neural innervation. *iScience, 24*(10), 103127. doi:10.1016/j.isci.2021.103127

Witte, N., Muenzner, M., Rietscher, J., Knauer, M., Heidenreich, S., Nuotio-Antar, A. M., . . . Schupp, M. (2015). The Glucose Sensor ChREBP Links De Novo Lipogenesis to PPARgamma Activity and Adipocyte Differentiation. *Endocrinology, 156*(11), 4008-4019. doi:10.1210/EN.2015-1209

Yamamoto, K., Kiyohara, T., Murayama, Y., Kihara, S., Okamoto, Y., Funahashi, T., . . . Shinomura, Y. (2005). Production of adiponectin, an anti-inflammatory protein, in mesenteric adipose tissue in Crohn's disease. *Gut, 54*(6), 789-796. doi:10.1136/gut.2004.046516

Ye, R., & Scherer, P. E. (2013). Adiponectin, driver or passenger on the road to insulin sensitivity? *Mol Metab, 2*(3), 133-141. doi:10.1016/j.molmet.2013.04.001

Youngstrom, T. G., & Bartness, T. J. (1998). White adipose tissue sympathetic nervous system denervation increases fat pad mass and fat cell number. *Am J Physiol, 275*(5), R1488-1493. doi:10.1152/ajpregu.1998.275.5.R1488

Younossi, Z. M., Koenig, A. B., Abdelatif, D., Fazel, Y., Henry, L., & Wymer, M. (2016). Global epidemiology of nonalcoholic fatty liver disease-Meta-analytic assessment of prevalence, incidence, and outcomes. *Hepatology, 64*(1), 73-84. doi:10.1002/hep.28431

Yu, D., Tomasiewicz, J. L., Yang, S. E., Miller, B. R., Wakai, M. H., Sherman, D. S., . . . Lamming, D. W. (2019). Calorie-Restriction-Induced Insulin Sensitivity Is Mediated by Adipose mTORC2 and Not Required for Lifespan Extension. *Cell Rep, 29*(1), 236-248 e233. doi:10.1016/j.celrep.2019.08.084

Zeng, W., Pirzgalska, R. M., Pereira, M. M., Kubasova, N., Barateiro, A., Seixas, E., . . . Domingos, A. I. (2015). Sympathetic neuro-adipose connections mediate leptin-driven lipolysis. *Cell, 163*(1), 84-94. doi:10.1016/j.cell.2015.08.055

Zhang, Y., Proenca, R., Maffei, M., Barone, M., Leopold, L., & Friedman, J. M. (1994). Positional cloning of the mouse obese gene and its human homologue. *Nature, 372*(6505), 425-432. doi:10.1038/372425a0

Zinzalla, V., Stracka, D., Oppliger, W., & Hall, M. N. (2011). Activation of mTORC2 by association with the ribosome. *Cell, 144*(5), 757-768. doi:10.1016/j.cell.2011.02.014

Chapter 7: Appendix

7. Appendix

JCI The Journal of Clinical Investigation

Insulin resistance causes inflammation in adipose tissue

Mitsugu Shimobayashi, … , Ralph Peterli, Michael N. Hall

J Clin Invest. 2018;128(4):1538-1550. https://doi.org/10.1172/JCI96139.

Research Article **Inflammation** **Metabolism**

Obesity is a major risk factor for insulin resistance and type 2 diabetes. In adipose tissue, obesity-mediated insulin resistance correlates with the accumulation of proinflammatory macrophages and inflammation. However, the causal relationship of these events is unclear. Here, we report that obesity-induced insulin resistance in mice precedes macrophage accumulation and inflammation in adipose tissue. Using a mouse model that combines genetically induced, adipose-specific insulin resistance (mTORC2-knockout) and diet-induced obesity, we found that insulin resistance causes local accumulation of proinflammatory macrophages. Mechanistically, insulin resistance in adipocytes results in production of the chemokine monocyte chemoattractant protein 1 (MCP1), which recruits monocytes and activates proinflammatory macrophages. Finally, insulin resistance (high homeostatic model assessment of insulin resistance [HOMA-IR]) correlated with reduced insulin/mTORC2 signaling and elevated MCP1 production in visceral adipose tissue from obese human subjects. Our findings suggest that insulin resistance in adipose tissue leads to inflammation rather than vice versa.

Insulin resistance causes inflammation in adipose tissue

Mitsugu Shimobayashi,[1] Verena Albert,[1] Bettina Woelnerhanssen,[2] Irina C. Frei,[1] Diana Weissenberger,[1] Anne Christin Meyer-Gerspach,[2] Nicolas Clement,[3] Suzette Moes,[1] Marco Colombi,[1] Jerome A. Meier,[1] Marta M. Swierczynska,[1] Paul Jenö,[1] Christoph Beglinger,[2] Ralph Peterli,[3] and Michael N. Hall[1]

[1]Biozentrum, University of Basel, Basel, Switzerland. [2]Department of Research and [3]Department of Surgery, St. Claraspital, Basel, Switzerland.

Obesity is a major risk factor for insulin resistance and type 2 diabetes. In adipose tissue, obesity-mediated insulin resistance correlates with the accumulation of proinflammatory macrophages and inflammation. However, the causal relationship of these events is unclear. Here, we report that obesity-induced insulin resistance in mice precedes macrophage accumulation and inflammation in adipose tissue. Using a mouse model that combines genetically induced, adipose-specific insulin resistance (mTORC2-knockout) and diet-induced obesity, we found that insulin resistance causes local accumulation of proinflammatory macrophages. Mechanistically, insulin resistance in adipocytes results in production of the chemokine monocyte chemoattractant protein 1 (MCP1), which recruits monocytes and activates proinflammatory macrophages. Finally, insulin resistance (high homeostatic model assessment of insulin resistance [HOMA-IR]) correlated with reduced insulin/mTORC2 signaling and elevated MCP1 production in visceral adipose tissue from obese human subjects. Our findings suggest that insulin resistance in adipose tissue leads to inflammation rather than vice versa.

Introduction

Obesity-induced insulin resistance is a major risk factor for type 2 diabetes, hyperlipidemia, cardiovascular disease, and some types of cancer (1–3). Although the mechanism by which obesity causes insulin resistance is unclear, inflammation has been linked to the development of local and systemic insulin resistance, especially when the inflammation occurs in white adipose tissue (WAT) (4, 5).

WAT consists of adipocytes and stromal vascular cells (SVCs) including endothelial cells, preadipocytes, and immune cells (6). Among the immune cells, macrophages play a particularly important role in obesity-induced adipose tissue inflammation. Macrophages are classified into 2 types: proinflammatory M1 and antiinflammatory M2 macrophages. M1 macrophages express the surface marker CD11c (7, 8) and produce proinflammatory cytokines such as TNF-α (9, 10). M2 macrophages express the surface marker CD301 and produce antiinflammatory cytokines such as IL-10 (7). The relative and absolute number of M1 macrophages increases in WAT upon obesity, thereby promoting adipose tissue inflammation (7–11). Studies in rodents have suggested that adipose tissue inflammation causes local and systemic insulin resistance (9, 11–13). However, it has been demonstrated that immunocompromised mice are not protected from systemic insulin resistance induced by a short-term high-fat diet (HFD) (14). Furthermore, Tian et al. have shown that adipose tissue inflammation is dispensable for local and systemic insulin resistance (15). Another study has shown that inhibition of adipose tissue inflammation results in glucose intolerance, suggesting that inflammation may even be a mechanism to counter insulin resistance (16). In humans, expression of the macrophage markers CD68 and TNF-α in WAT correlates with BMI, suggesting that obesity may induce the accumulation of adipose tissue macrophages and inflammation in humans (9, 17). However, clinical trials targeting TNF-α have shown little or no beneficial effect on systemic insulin sensitivity (18–21). Thus, the causal relationship between adipose tissue inflammation and insulin resistance is unclear.

Two models have been proposed to explain the increase in the number of M1 macrophages in WAT upon obesity. The first is that circulating monocytes are recruited to WAT, where they differentiate into M1 macrophages (7, 22). The second is that obesity induces the proliferation of resident macrophages in WAT (23). The monocyte chemoattractant protein 1/C-C chemokine ligand 2 (MCP1/CCL2), presumably produced by adipocytes, is required to increase the number of macrophages in WAT (12, 23, 24). However, the mechanism(s) controlling MCP1 expression in adipocytes upon obesity are poorly understood.

The target of rapamycin complex 2 (TORC2) is an evolutionarily conserved serine/threonine protein kinase complex that controls growth and metabolism (reviewed in ref. 25). In mammals, mTORC2 consists of mTOR, rapamycin-insensitive companion of mTOR (RICTOR), mammalian stress-activated protein kinase–interacting protein 1 (mSIN1), and mammalian lethal with SEC thirteen 8 (mLST8) (26–31). Insulin stimulates mTORC2 to promote glucose uptake in adipose tissue (32–34), liver (35–37), and skeletal muscle (38, 39). Previously, we and others have shown that adipose-specific *Rictor* knockout (AdRiKO) exacerbates obesity-related complications in mice, such as systemic insulin resistance and hepatic steatosis (32–34).

Here, we used mTORC2-deficient and therefore insulin-resistant AdRiKO mice to investigate the causal relationship between

Conflict of interest: The authors have declared that no conflict of interest exists.
Submitted: July 7, 2017; **Accepted:** January 30, 2018.
Reference information: *J Clin Invest*. 2018;128(4):1538–1550.
https://doi.org/10.1172/JCI96139.

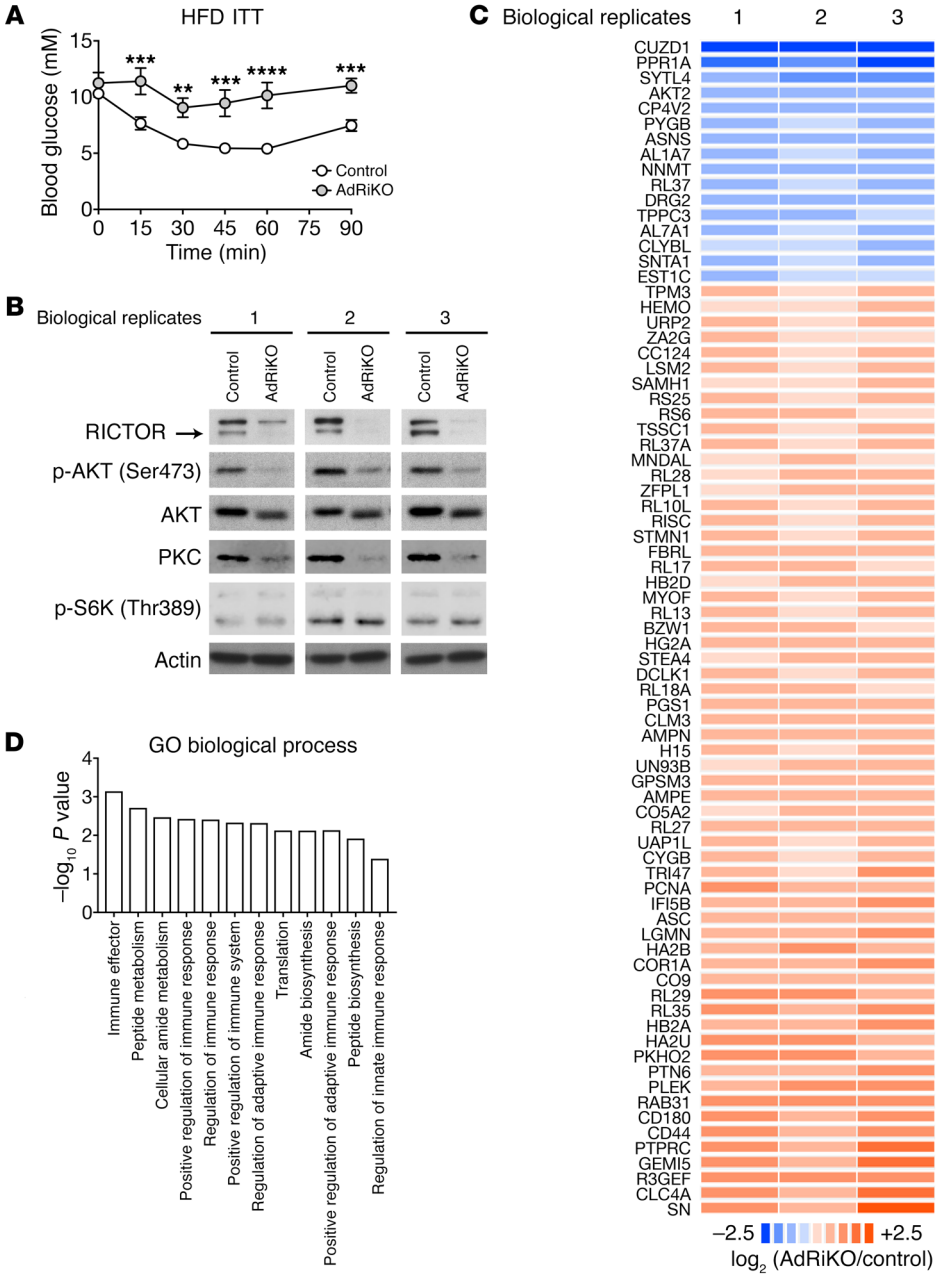

Figure 1. Quantitative proteome analysis reveals insulin/mTORC2 signaling functions in adipose tissue inflammation. (**A**) ITT for AdRiKO and control mice fed a HFD for 10 weeks. Mice were fasted for 5 hours prior to the ITT. Data are presented as the mean ± SEM. $^{**}P < 0.01$, $^{***}P < 0.001$, and $^{****}P < 0.0001$, by 2-way ANOVA. $n = 10$ (control) and $n = 5$ (AdRiKO). (**B**) Immunoblots of eWAT from HFD-fed AdRiKO and control mice. eWAT samples were collected from ad libitum–fed mice. The same lysates were used for proteome analysis. (**C**) Regulated proteome with 3 biological replicates. See also Supplemental Table 1. (**D**) GO term analysis of the regulated proteome. Data are presented as the mean ± SEM.

insulin resistance and inflammation. We found that inhibition of the insulin/mTORC2 pathway resulted in enhanced *Mcp1* transcription in mouse and human adipocytes and thereby promoted inflammation in visceral WAT. Furthermore, obesity-induced insulin resistance developed before the accumulation of proinflammatory M1 macrophages in visceral WAT of WT mice. Thus, insulin resistance precedes and causes inflammation in adipose tissue.

Results

Insulin/mTORC2 signaling in WAT negatively controls inflammation. AdRiKO exacerbates systemic insulin resistance upon obesity, as evidenced by impaired glucose clearance in response to insulin treatment (Figure 1A and refs. 32–34). Thus, the AdRiKO mouse is a good model to investigate the causal relationship between insulin resistance and inflammation upon obesity. To determine whether insulin resistance due to impaired insulin/mTORC2 signaling in WAT affects adipose inflammation, we performed quantitative proteomics on epididymal WAT (eWAT) from HFD-fed (for 10 weeks) AdRiKO (*aP2-Cre, Rictor*$^{fl/fl}$) and control (*Rictor*$^{fl/fl}$) mice. As previously reported (32–34), HFD-fed AdRiKO mice had an increased body size with no change in adiposity (Supplemental Figure 1, A–C; supplemental material available online with this article; https://doi.org/10.1172/JCI96139DS1). Furthermore, we confirmed that RICTOR expression, AKT (Ser473) phosphorylation, and PKC expression, readouts for mTORC2 signaling, were decreased, while S6K (Thr389) phosphorylation, a readout for mTORC1 signaling, was not affected in eWAT (Figure 1B; see complete unedited blots in the supplemental material). Among approximately 3,000 proteins identified in the proteome, 61 and 16 were up- and downregulated, respectively, in AdRiKO mice

compared with controls (Figure 1C and Supplemental Table 1). Gene Ontology (GO) analysis of the regulated proteins revealed enrichment of immune response–related biological processes (Figure 1D), suggesting that insulin resistance due to loss of mTORC2 signaling may cause inflammation upon obesity.

To examine further whether mTORC2 in WAT controls inflammation, we quantified immune cells in eWAT of HFD-fed AdRiKO and control mice by flow cytometry. While the numbers of B and T cells did not differ (Supplemental Figure 1D), the number of macrophages ($F4/80^+CD11b^+$) increased in AdRiKO eWAT at 10 weeks of HFD feeding (Figure 2, A and B, and Supplemental Figure 2A). The increase in macrophages correlated with increased macrophage gene expression (*Cd68* and *F4/80*) and F4/80 staining (Figure 2, C and D). Next, we determined whether the increase in the number of macrophages in AdRiKO eWAT was due to an increase in proinflammatory M1 ($F4/80^+CD11b^+CD11c^+$) and/or antiinflammatory M2 ($F4/80^+CD11b^+CD301^+$) macrophages. The numbers of both M1 and M2 macrophages increased in both AdRiKO and control mice during the HFD time course (Figure 2, E–G). AdRiKO eWAT showed a disproportionately large increase in M1 macrophages, starting at 6 weeks of HFD feeding (Figure 2, E and F). Quantification of proinflammatory cytokine TNF-α mRNA in SVCs and macrophages isolated from HFD-fed AdRiKO and control mice confirmed the disproportionate increase in M1 macrophages in AdRiKO eWAT (Figure 2, H and I, and Supplemental Figure 2, B and C). These observations indicate that AdRiKO leads to the accumulation of M1 macrophages, confirming that genetically induced insulin resistance due to loss of mTORC2 signaling in WAT promotes inflammation. We note that there was no difference in macrophage numbers between AdRiKO and control mice on a normal diet (ND) (Supplemental Figure 3, A–E), indicating that AdRiKO potentiates inflammation only in response to obesity.

Our AdRiKO model relies on the adipose-specific promoter *aP2* to drive *Cre* expression and thereby knock out *Rictor*. However, *aP2-Cre* can be expressed in cell types other than adipocytes including macrophages (40, 41). Three lines of evidence suggest that our findings are not due to confounding effects of ectopic knockout of *Rictor* in macrophages. First, *Rictor* expression was unchanged in macrophages isolated from the HFD-fed AdRiKO mice compared with those from control mice (Supplemental Figure 4, A and B). Second, adipose-specific deletion of *Rictor* via expression of *Cre* from the *Adipoq* promoter (i-AdRiKO: *Adipoq-CreER*^{T2}, *Rictor*$^{fl/fl}$) (40, 42) also showed an increase in M1 macrophages in eWAT upon obesity, as observed in *aP2-Cre* AdRiKO mice (Figure 2, J–M, and Supplemental Figure 4, C and D). Third, macrophage-specific knockout of *Rictor*, due to expression of *Cre* from the *LysM* promoter (*LysM-Cre Rictor*$^{fl/fl}$), had no effect on macrophages in WAT of mice fed a HFD (43).

HFD-induced insulin resistance precedes the accumulation of adipose tissue M1 macrophages. Our findings indicate that genetically induced local insulin resistance causes the accumulation of M1 macrophages and thus inflammation in WAT upon obesity. This predicts that HFD-induced insulin resistance precedes inflammation in WT mice. To test this prediction, we performed a longitudinal study with HFD-fed WT mice (Supplemental Figure 5A). WT mice developed eWAT and systemic insulin resistance by week 4 of HFD feeding, as measured by insulin-stimulated glucose uptake and an insulin tolerance test (ITT) (Figure 3, A and B, and Supplemental Figure 5B), respectively. Mice fed a HFD for 10 weeks remained insulin resistant compared with mice on a ND (Figure 3C and Supplemental Figure 5C). The M1 macrophage population in eWAT mildly increased in mice by week 10 of a HFD, but not by 4 or 8 weeks (Figure 3D). *Tnfa* expression did not increase in mice at 4 or 10 weeks of a HFD (Supplemental Figure 5D). These findings are consistent with previous reports showing that mice develop adipose and systemic insulin resistance within several days to 4 weeks of a HFD (44, 45), whereas the number of M1 macrophages in WAT increases only within 8 to 10 weeks of a HFD (10, 15, 45, 46). The finding that HFD-induced insulin resistance precedes the accumulation of M1 macrophages is consistent with our above conclusion that insulin resistance leads to inflammation.

Insulin resistance–induced inflammation is specific to visceral WAT. Adipose-specific loss of mTORC2 signaling directly causes insulin resistance in all WAT depots and indirectly leads to systemic insulin resistance (32–34). To test whether AdRiKO causes inflammation in liver or in fat depots other than eWAT (see above), we examined macrophage numbers in peri-renal WAT (prWAT), subcutaneous WAT (sWAT), and liver of HFD-fed AdRiKO and control mice. AdRiKO prWAT, but not sWAT or liver, had increased numbers of M1 macrophages, (Supplemental Figure 6, A–C). Thus, AdRiKO promotes inflammation specifically in visceral WAT (eWAT and prWAT).

To test whether local insulin resistance causes inflammation in the liver, we examined hepatic macrophages in liver-specific *Rictor*-knockout mice (LiRiKO: *Alb-Cre*, *Rictor*$^{fl/fl}$), which have hepatic insulin resistance due to loss of insulin/mTORC2 signaling in liver (35–37). HFD-fed LiRiKO mice had a moderate but nonsignificant increase in the number of hepatic macrophages compared with HFD-fed control mice (Supplemental Figure 6D). Furthermore, the numbers of M1 and M2 macrophages in eWAT were identical in LiRiKO and control mice (Supplemental Figure 6E). Thus, the ability of local insulin resistance to promote inflammation is specific to visceral WAT.

Rictor knockout in adipocytes increases expression of the chemokine MCP1. How does insulin resistance in visceral WAT cause local accumulation of M1 macrophages and inflammation? Amano et al. have suggested that a HFD induces local proliferation of macrophages (23). Alternatively, others have proposed that WAT recruits circulating monocytes, which then differentiate into M1 macrophages (7, 22). To distinguish between these 2 models, we used flow cytometry to measure the proliferation marker Ki-67 in macrophages in eWAT of HFD-fed mice. The percentage of $Ki\text{-}67^+$ M1 macrophages in AdRiKO mice was similar to that in control mice (Supplemental Figure 7A), suggesting that the increase in M1 macrophages in AdRiKO eWAT is not due to local proliferation. To investigate the possibility that WAT recruits monocytes, we examined the expression of WAT-derived chemokines in eWAT from HFD-fed AdRiKO and control mice. A chemokine array and ELISA revealed increased expression of monocyte chemoattractant protein 1 (MCP1, also known as C-C motif ligand 2 [CCL2]) in AdRiKO eWAT (Figure 4, A and B). Increased levels of MCP1 were also detected in the plasma of HFD-fed AdRiKO mice (Figure 4C). Furthermore, in SVCs isolated from AdRiKO eWAT, we observed

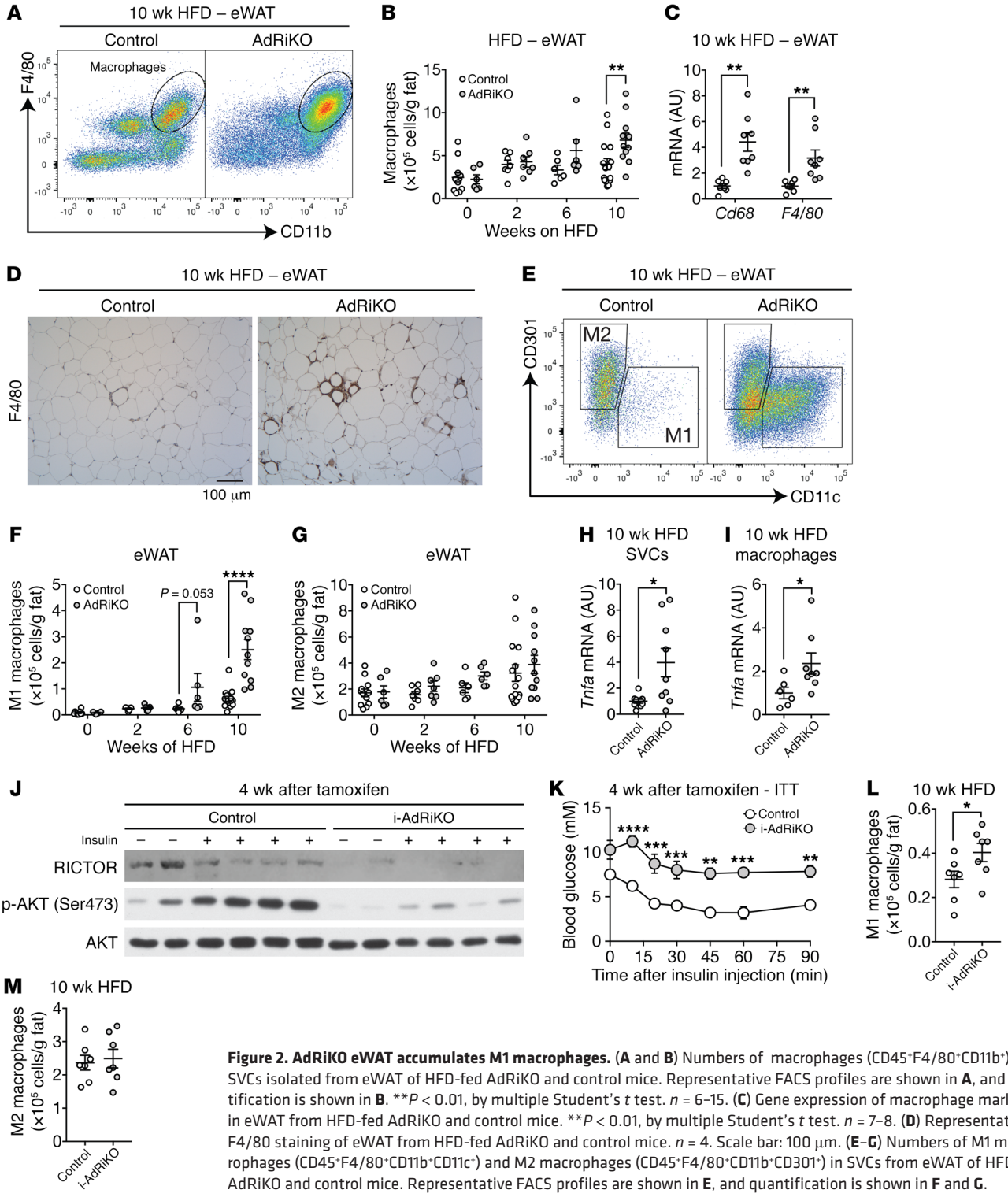

Figure 2. AdRiKO eWAT accumulates M1 macrophages. (**A** and **B**) Numbers of macrophages ($CD45^+F4/80^+CD11b^+$) in SVCs isolated from eWAT of HFD-fed AdRiKO and control mice. Representative FACS profiles are shown in **A**, and quantification is shown in **B**. $^{**}P < 0.01$, by multiple Student's *t* test. $n = 6–15$. (**C**) Gene expression of macrophage markers in eWAT from HFD-fed AdRiKO and control mice. $^{**}P < 0.01$, by multiple Student's *t* test. $n = 7–8$. (**D**) Representative F4/80 staining of eWAT from HFD-fed AdRiKO and control mice. $n = 4$. Scale bar: 100 μm. (**E**–**G**) Numbers of M1 macrophages ($CD45^+F4/80^+CD11b^+CD11c^+$) and M2 macrophages ($CD45^+F4/80^+CD11b^+CD301^+$) in SVCs from eWAT of HFD-fed AdRiKO and control mice. Representative FACS profiles are shown in **E**, and quantification is shown in **F** and **G**. $^{****}P < 0.0001$ and $P = 0.053$, by multiple Student's *t* test. $n = 6–15$. (**H** and **I**) *Tnfa* gene expression in SVCs (**H**) ($n = 9$) and isolated macrophages (**I**) ($n = 6–8$) from eWAT of HFD-fed AdRiKO and control mice. $^{*}P < 0.05$, by unpaired Student's *t* test. (**J**) Immunoblots of eWAT from i-AdRiKO and control mice. Mice were treated with tamoxifen for 5 days. After 4 weeks, mice were fasted for 5 hours and then treated with PBS or insulin. (**K**) ITT for i-AdRiKO and control mice 4 weeks after induction of *Rictor* knockout. Mice were fasted for 5 hours prior to the ITT. $^{**}P < 0.01$, $^{***}P < 0.001$, and $^{****}P < 0.0001$, by 2-way ANOVA. $n = 5$ (control) and $n = 6$ (i-AdRiKO). (**L** and **M**) Numbers of M1 macrophages ($CD45^+F4/80^+CD11b^+CD11c^+$) (**L**) and M2 macrophages ($CD45^+F4/80^+CD11b^+CD301^+$) (**M**) in SVCs from eWAT of HFD-fed i-AdRiKO and control mice. $^{*}P < 0.05$, by unpaired Student's *t* test. $n = 7$. Data are presented as the mean ± SEM.

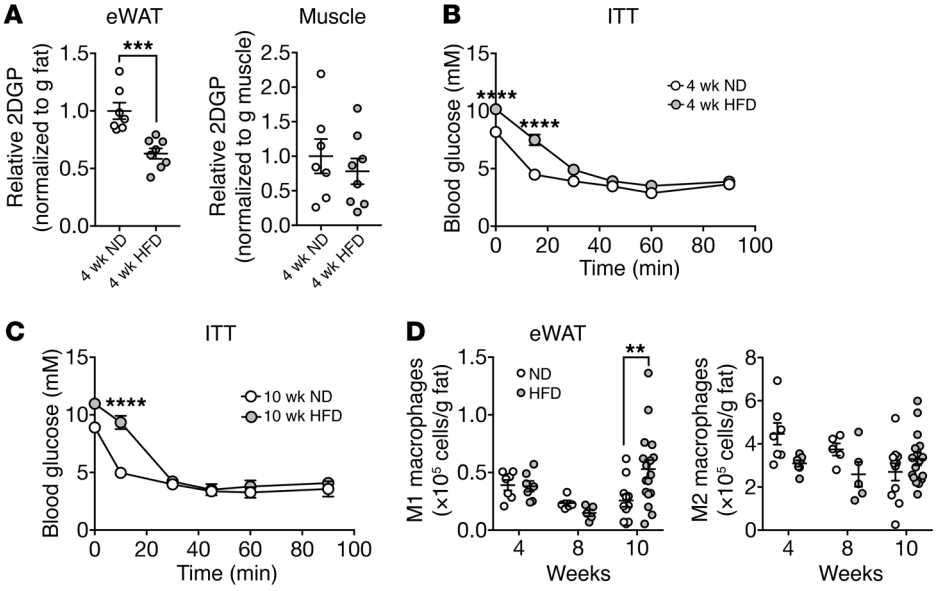

Figure 3. HFD-induced insulin resistance precedes the accumulation of M1 macrophages. (**A**) Insulin-stimulated 2DGP accumulation in eWAT and muscle from WT mice fed a ND or HFD for 4 weeks. Mice were fasted for 5 hours, injected with insulin at 0 minutes and 2DG at 10 minutes, and sacrificed at 30 minutes. ***$P < 0.001$, by unpaired Student's *t* test. $n = 7–8$. (**B** and **C**) ITT for WT mice fed a ND or HFD for 4 weeks (**B**) or 10 weeks (**C**). Mice were fasted for 5 hours prior to the ITT. ****$P < 0.0001$, by 2-way ANOVA. $n = 15$ (4 wk ND), $n = 17$ (4 wk HFD), $n = 3$ (10 wk ND), and $n = 4$ (10 wk HFD). (**D**) Numbers of M1 macrophages ($CD45^+F4/80^+CD11b^+CD11c^+$) and M2 macrophages ($CD45^+F4/80^+CD11b^+CD301^+$) in eWAT of WT mice fed a HFD for 4, 8, or 10 weeks. **$P < 0.01$, by multiple Student's *t* test. $n = 5–17$. $Rictor^{fl/fl}$ mice were used as WT controls. Data are presented as the mean ± SEM.

significantly increased expression of C-C chemokine receptor type 2 (*Ccr2*), encoding an MCP1 receptor, as a result of increased numbers of *Ccr2*-expressing cells such as monocytes and macrophages (Figure 4D). These findings suggest that insulin-resistant visceral WAT, via MCP1 expression, recruits monocytes, which then differentiate into M1 macrophages.

We next tested whether the increase in MCP1 is responsible for M1 macrophage accumulation in AdRiKO eWAT. Mice were fed a HFD for 8 weeks and then treated with an MCP1-neutralizing or control antibody for 2 weeks along with ongoing HFD feeding. The antibody treatments had no impact on body weight (Supplemental Figure 7B). The MCP1-neutralizing antibody inhibited the accumulation of M1 macrophages in AdRiKO eWAT by 50%, with no impact on M2 macrophages (Figure 4E). The MCP1-neutralizing antibody also caused a 2-fold increase in monocytes ($Ly\text{-}6C^{hi}CD11b^+$) in the blood of AdRiKO mice (Figure 4F). Thus, MCP1 appears to mediate the increase in M1 macrophages in AdRiKO eWAT. Altogether, our data suggest that mTORC2 inhibition in WAT results in *Mcp1* expression, followed by infiltration of monocytes in an MCP1-CCR2–dependent manner.

Insulin/mTORC2 signaling inhibits Mcp1 transcription in adipocytes. Expression of the *Mcp1* gene was increased in the eWAT of HFD-fed AdRiKO and i-AdRiKO mice compared with expression levels in control eWAT (Figure 5, A and B), suggesting that MCP1 is upregulated in AdRiKO WAT at the transcriptional level. Furthermore, we note that the increase in *Mcp1* expression (Figure 5A) coincided with an increase in the number of M1 macrophages in AdRiKO eWAT (Figure 2F). The number of macrophages and expression levels of *Mcp1* were unchanged in AdRiKO and control eWAT in ND-fed mice (Supplemental Figure 3 and Supplemental Figure 8A). To identify the cells in which *Mcp1* expression was induced, we measured *Mcp1* mRNA levels in adipocytes and SVCs isolated from eWAT of HFD-fed AdRiKO and control mice (Supplemental Figure 2B). AdRiKO adipocytes, but not SVCs, showed increased *Mcp1* expression (Figure 5, C and D). To determine whether the regulation of *Mcp1* transcription by mTORC2 is cell autonomous, we first treated 3T3-L1 adipocytes with the mTOR inhibitor torin 1 (47). 3T3-L1 adipocytes treated with torin 1 had increased *Mcp1* expression (Figure 5E). Next, we generated 2 *Rictor*-knockout 3T3-L1 adipocyte cell lines (Figure 5F and Supplemental Figure 8B) using the genome-editing CRISPR-Cas9 system (48). *Rictor*-knockout 3T3-L1 adipocytes were able to differentiate, albeit at a slower rate compared with control cells (Supplemental Figure 8C). Consistent with our in vivo data, *Mcp1* expression was increased in the *Rictor*-knockout 3T3-L1 adipocytes (Figure 5G and Supplemental Figure 8B). Serum and insulin treatment suppressed *Mcp1* expression in control but not *Rictor*-knockout 3T3-L1 adipocytes (Figure 5H and Supplemental Figure 8D). In WT mice, *Mcp1* expression increased by 10 weeks, but not 4 weeks, of HFD feeding (Supplemental Figure 8E). These data support the notion that insulin resistance precedes and promotes *Mcp1* transcription in adipocytes. We note that *Rictor* knockout in liver (LiRiKO) did not result in hepatic *Mcp1* expression (Supplemental Figure 8F), consistent with our above finding that LiRiKO failed to stimulate inflammation in liver.

How does mTORC2 loss lead to *Mcp1* transcription? It has been suggested that JNK is required for MCP1 expression and secretion in cultured 3T3-L1 adipocytes (49). Consistent with that report, treatment with the JNK inhibitor SP600125 reduced *Mcp1* expression in *Rictor*-knockout 3T3-L1 cells (Figure 5I). Inhibition of JNK was confirmed by loss of cJUN (Ser73) phosphorylation (Figure 5J). SP600125 did not restore AKT (Ser 473) phosphorylation (Figure 5J) or insulin-stimulated glucose uptake (Figure 5F) in the *Rictor*-knockout 3T3-L1 cells, indicating that the effect of the drug was independent of mTORC2 and insulin resistance. Furthermore, JNK activity was unaffected by *Rictor* knockout (Figure 5, J and K). Thus, mTORC2 and JNK control *Mcp1* expression independently.

Impaired insulin/mTORC2 signaling and increased MCP1 expression in omental WAT of obese patients. *MCP1* mRNA levels in omental WAT (oWAT) correlate with BMI in obese human subjects (9, 50). However, how *MCP1* transcription is regulated in human adipose tissue is unknown. Our finding that insulin/mTORC2 sig-

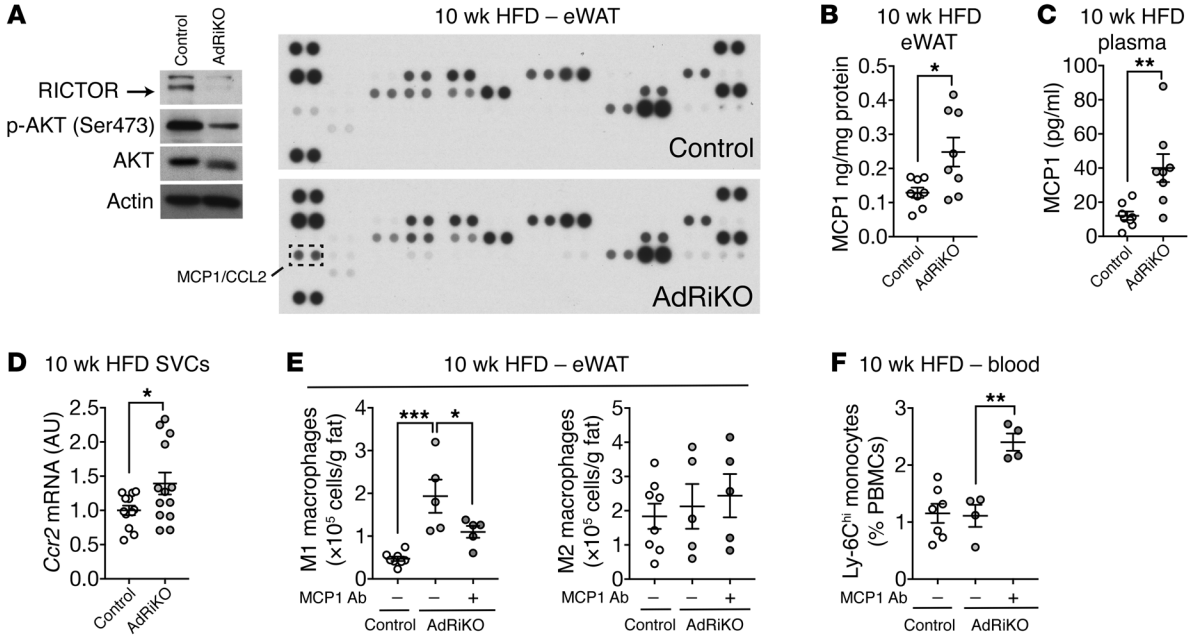

Figure 4. Insulin/mTORC2 signaling inhibits *Mcp1* transcription and M1 macrophage accumulation in vivo. (**A**) Adipokine array of eWAT from HFD-fed AdRiKO and control mice. Immunoblots show the reduction of RICTOR expression and mTORC2 signaling. $n = 8$ (data from 8 mice were pooled). (**B**) MCP1 protein levels in eWAT from HFD-fed AdRiKO and control mice. $^*P < 0.05$, by unpaired Student's t test. $n = 8$. (**C**) MCP1 protein levels in plasma from HFD-fed AdRiKO and control mice. $^{**}P < 0.01$, by unpaired Student's t test. $n = 8$. (**D**) *Ccr2* mRNA levels in SVCs isolated from eWAT of HFD-fed AdRiKO and control mice. $^*P < 0.05$, by unpaired Student's t test. $n = 12$. (**E**) Numbers of M1 macrophages ($CD45^+F4/80^+CD11b^+CD11c^+$) and M2 macrophages ($CD45^+F4/80^+CD11b^+CD301^+$) in eWAT. Mice were fed a HFD for 8 weeks and treated with a control or MCP1-neutralizing antibody for 2 weeks with ongoing HFD feeding. $^*P < 0.05$ and $^{***}P < 0.001$, by 1-way ANOVA. $n = 5–8$. (**F**) Percentage of inflammatory monocytes in peripheral blood mononuclear cells (PBMCs). Mice were treated as in **E**. $^{**}P < 0.01$, by 1-way ANOVA. $n = 4–7$. Data are presented as the mean ± SEM.

naling negatively controls *Mcp1* transcription and adipose tissue inflammation in mice prompted us to examine insulin/mTORC2 signaling, *MCP1* expression, and macrophage accumulation in human visceral WAT, i.e., oWAT. To this end, oWAT samples were collected from 20 lean and 30 obese human patients who were under general anesthesia (Figure 6A and Supplemental Table 2). The obese patients were insulin resistant as determined by high homeostatic model assessment of insulin resistance (HOMA-IR) (Figure 6B and Supplemental Figure 9A). We note that oWAT was collected from patients who, because of standard procedure before undergoing general anesthesia, had fasted overnight, a condition that might not be optimal for the evaluation of insulin/mTORC2 signaling. Nevertheless, in oWAT, AKT2 (Ser474) phosphorylation, a readout for mTORC2 signaling, was lower in obese patients than in lean patients (Figure 6, C and D). AKT2 (Ser474) phosphorylation negatively correlated with BMI (Figure 6E). These data suggest that insulin/mTORC2 signaling is impaired in oWAT of obese and insulin-resistant patients and validate AdRiKO mice as a model for human insulin resistance. *MCP1* expression was higher in obese subjects and positively correlated with BMI (Figure 6, F and G, and Supplemental Figure 9B). *CD68* expression was also higher in the obese subjects and positively correlated with BMI (Figure 6, H and I, and Supplemental Figure 9C). *MCP1* and *CD68* expression levels also correlated (Figure 6J). AKT2 (Ser474) phosphorylation did not correlate with *MCP1* and *CD68* expression (Supplemental Figure 9, D and E) when comparing the entire cohort of 50 patients, consistent with our above observation in mice that inhibition of insulin/mTORC2 signaling alone was not sufficient to promote adipose tissue inflammation (Supplemental Figure 3). However, approximately one-third of the obese patients (9 of 30) had low AKT (Ser474) phosphorylation and high HOMA-IR, *MCP1*, and *CD68* (Figure 6K), suggesting that AdRiKO mice may phenocopy this subgroup of patients. Finally, torin 1 treatment led to an increase in *MCP1* expression in human primary adipocytes, suggesting that insulin/mTOR signaling inhibits *MCP1* expression also in humans (Figure 6, L and M).

Discussion

We provide 2 lines of evidence that insulin resistance promotes the accumulation of M1 macrophages and thereby fosters inflammation (Figure 7). First, we show that knockout of mTORC2, i.e., genetically induced insulin resistance, in mouse adipocytes derepressed *Mcp1* expression. As a consequence, monocytes were recruited to visceral WAT, where they differentiated into M1 macrophages and caused inflammation. Second, HFD-induced insulin resistance in WT mice preceded the accumulation of proinflammatory M1 macrophages. We also show that oWAT from obese, insulin-resistant patients had low mTORC2 signaling, high *MCP1* expression, and high macrophage content, suggesting that our findings in mice have human relevance (Figure 6).

Our findings are consistent with observations made in mice genetically modified in other components of the insulin signaling pathway. Two studies demonstrated that deletion of PTEN or PIK3R1, negative regulators of insulin signaling, causes enhanced insulin sensitivity and a reduced number of macrophages in adipose tissue (51, 52). More recently, Shearin et al. (53) showed that

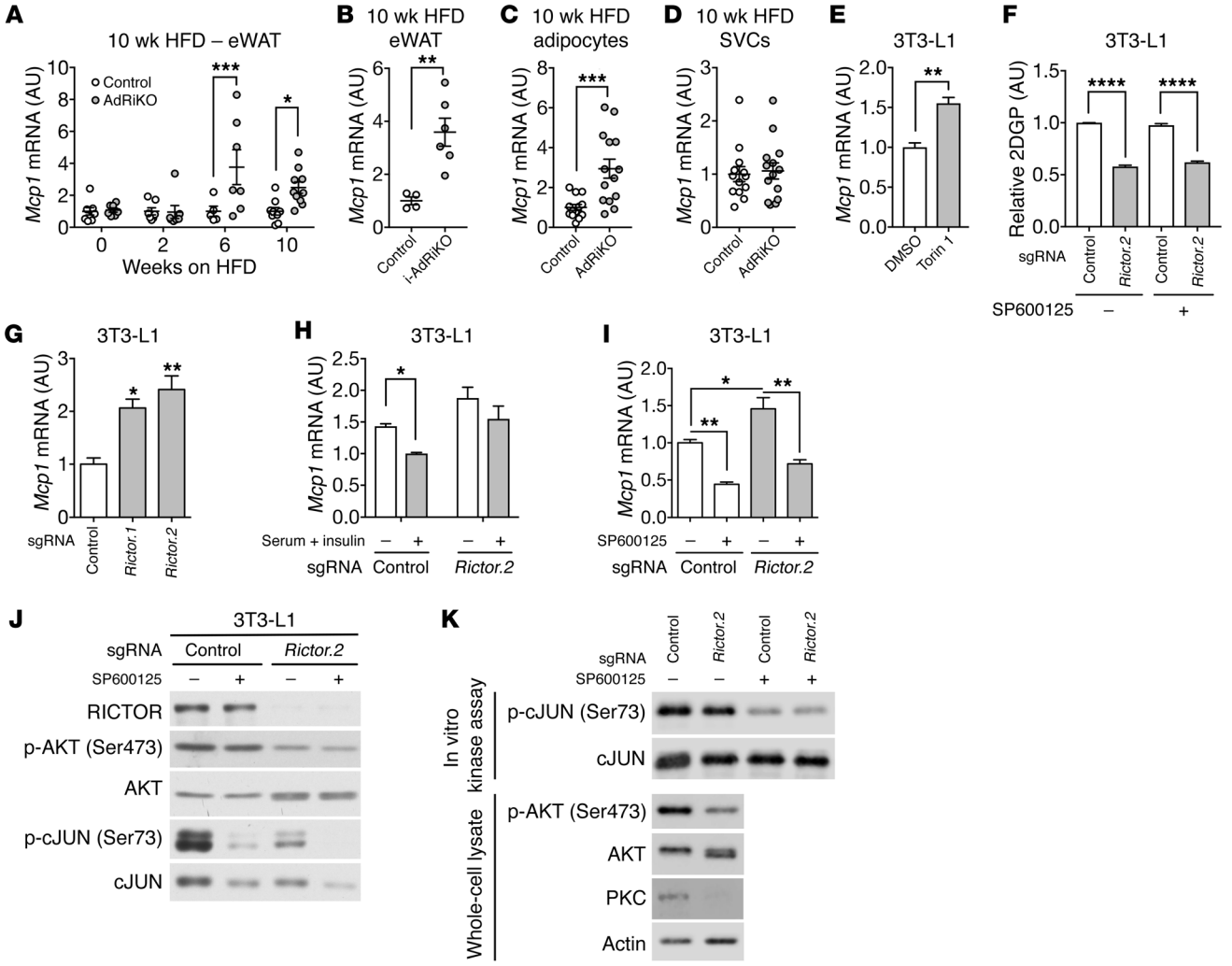

Figure 5. Insulin/mTORC2 signaling inhibits *Mcp1* transcription in adipocytes. (**A**) *Mcp1* mRNA levels in eWAT from AdRiKO and control mice during the HFD time course. **P* < 0.05 and ****P* < 0.001, by multiple Student's *t* test. *n* = 5–10. (**B**) *Mcp1* mRNA levels in eWAT from HFD-fed i-AdRiKO and control mice. ***P* < 0.01, by unpaired Student's *t* test. *n* = 4–6. (**C** and **D**) *Mcp1* mRNA levels in adipocytes (**C**) and SVCs (**D**) isolated from eWAT of HFD-fed AdRiKO and control mice. ****P* < 0.001, by unpaired Student's *t* test. *n* = 13–14. (**E**) *Mcp1* mRNA levels in 3T3-L1 adipocytes treated with DMSO or 250 nM torin 1 for 6 hours. ***P* < 0.01, by unpaired Student's *t* test. *N* >3. (**F**) 2DGP accumulation in insulin-stimulated *Rictor*-knockout or control 3T3-L1 adipocytes treated with DMSO or the JNK inhibitor SP600125 (20 μM). *N* = 3. (**G**) *Mcp1* mRNA levels in *Rictor*-knockout and control 3T3-L1 adipocytes. **P* < 0.05 and ***P* < 0.01, by unpaired Student's *t* test. *N* = 3. (**H**) *Mcp1* mRNA levels in *Rictor*-knockout and control 3T3-L1 adipocytes treated with or without serum and insulin. **P* < 0.05, by unpaired Student's *t* test. *N* = 3. (**I**) *Mcp1* mRNA levels in *Rictor*-knockout and control 3T3-L1 cells treated with DMSO or the JNK inhibitor SP600125 (20 μM) for 6 hours. **P* < 0.05 and ***P* < 0.01, by 1-way ANOVA. *N* = 3. (**J**) Immunoblots of *Rictor*-knockout and control 3T3-L1 adipocytes treated with DMSO or the JNK inhibitor SP600125 (20 μM) for 6 hours. *N* = 3. (**K**) In vitro JNK kinase assay. Active JNK was immunoprecipitated from *Rictor*-knockout or control 3T3-L1 adipocytes, and JNK activity was assessed toward its substrate cJUN. SP600125 treatment served as a negative control. *N* = 3. Data are presented as the mean ± SEM.

adipose-specific *Akt1*- and *Akt2*-knockout mice exhibit insulin resistance and increased macrophage infiltration in adipose tissue.

The above studies altogether may disentangle the "chicken-and-egg" relationship (see Introduction) of insulin resistance and inflammation, at least in adipose tissue. Obesity induces insulin resistance, via a yet-to-be defined mechanism, which in turn promotes inflammation. As suggested previously (16), this inflammation may contribute to adipose tissue remodeling and expansion to maintain glucose hemostasis. It has been suggested that activated M1 macrophages undergo metabolic reprogramming from oxidative phosphorylation to glycolysis (54, 55). Thus, a physiological role of M1 macrophages could be to clear excess local glucose. Our finding that insulin resistance precedes inflammation may account for the observation that inhibition of TNF-α is ineffective in the treatment of obesity-induced insulin resistance (18–21).

HFD-fed AdRiKO mice showed reduced AKT (Ser473) phosphorylation (Figure 1B), decreased glucose uptake (Figure 1A), and extensive inflammation (Figure 2) in eWAT. HFD-fed WT mice also displayed decreased glucose uptake (Figure 3, A–C), which was followed by mild inflammation (Figure 3D). Unexpectedly, AKT (Ser473) phosphorylation was not reduced in WT mice fed a HFD for 4 or 10 weeks (Supplemental Figure 5, E and F) (56), although we still observed mild inflammation in eWAT by week 10 of HFD feeding. We note that the number of M1 macrophages

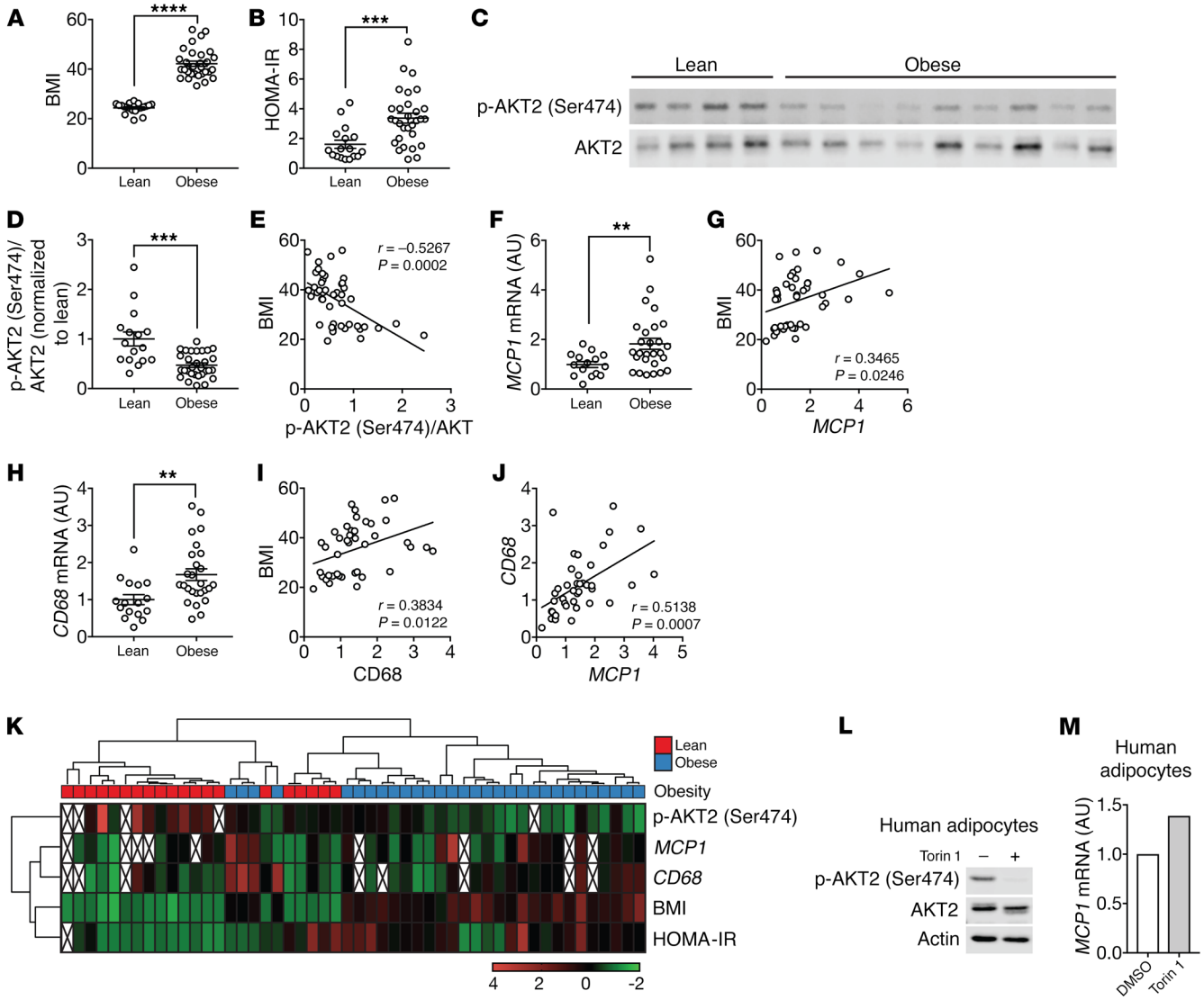

Figure 6. Impaired insulin/mTORC2 signaling and increased *MCP1* expression in oWAT of insulin-resistant obese patients. (**A** and **B**) BMI and HOMA-IR of lean and obese patients. ***$P < 0.001$ and ****$P < 0.0001$, by Mann-Whitney *U* test. See also Supplemental Table 2. (**C**) Representative immunoblots for p-AKT2 (Ser474) and AKT2 in human oWAT. (**D**) Quantification of p-AKT2 (Ser474) normalized to total AKT2. ***$P < 0.001$, by Mann-Whitney *U* test. (**E**) p-AKT2 (Ser474)/AKT2 negatively correlated with BMI. Significance was determined by Pearson's correlation analysis. (**F**) *MCP1* mRNA levels in human oWAT. **$P < 0.01$, by Mann-Whitney *U* test. (**G**) *MCP1* positively correlated with BMI. Significance was determined by Pearson's correlation analysis. (**H**) *CD68* mRNA levels in human oWAT. **$P < 0.01$, by Mann-Whitney *U* test. (**I** and **J**) *CD68* positively correlated with BMI (**I**) and *MCP1* levels (**J**). Significance in **I** and **J** was determined by Pearson's correlation analysis. (**K**) Cluster analysis of BMI, HOMA-IR, p-AKT2 (Ser474)/AKT2, *MCP1*, and *CD68* levels. (**L** and **M**) Effect of torin 1 on insulin/mTORC2 signaling (**L**) and *MCP1* mRNA levels (**M**) in human primary adipocytes. Differentiated human primary adipocytes were treated with DMSO or 250 nM torin 1 for 6 hours.

in AdRiKO eWAT was much higher than that in control eWAT by week 10 of the HFD (Figure 2F). These findings suggest that obesity-induced insulin resistance promotes mild inflammation downstream or independently of mTORC2, whereas chronic insulin resistance leads to mTORC2 inhibition and therefore extensive inflammation, as observed in AdRiKO mice and obese patients.

Our experiments reveal that loss of mTORC2 leads to increased *Mcp1* expression in adipocytes (Figure 5). What is the downstream effector through which mTORC2 controls *Mcp1* transcription? One candidate is the phosphatidic acid phosphatase LIPIN1, whose knockdown results in *Mcp1* expression in 3T3-L1 adipocytes (57). LIPIN1, independently of its phosphatase activity, also functions as a transcriptional repressor (58). We found that *Lipin1* expression was reduced in *Rictor*-knockout eWAT and adipocytes (Supplemental Figure 10, A and B), suggesting that mTORC2 may negatively control *Mcp1* transcription via LIPIN1. An adipose-specific transcription factor is another candidate through which mTORC2 may control *Mcp1* expression. *Rictor* knockout increased *Mcp1* expression in adipocytes, but not in liver or fibroblasts (Supplemental Figure 8F and Supplemental Figure 10C), indicating that the regulation of *Mcp1* transcription by mTORC2 is specific to adipocytes.

Why does AdRiKO eWAT accumulate a disproportionately high number of M1 macrophages only in response to obesity? The

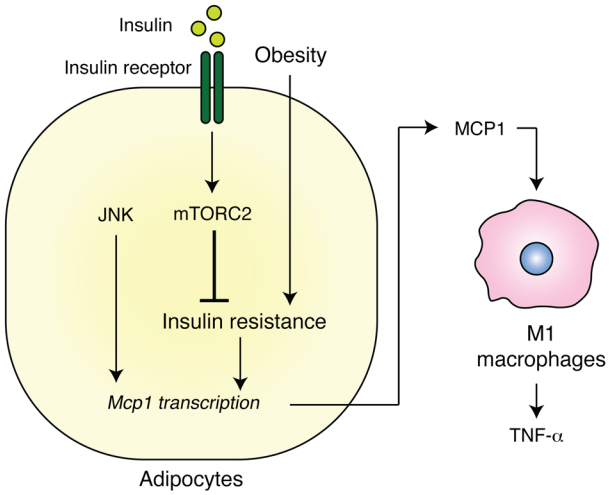

Figure 7. Insulin resistance causes inflammation in adipose tissue. Insulin resistance, due to obesity and loss of insulin/mTORC2 signaling, results in enhanced production of MCP1 in adipocytes. MCP1 in turn recruits monocytes and activates proinflammatory M1 macrophages.

increase in *Mcp1* transcription in mTORC2-knockout adipocytes required JNK activity (Figure 5I), which is high only in WAT from obese mice (59, 60). Thus, obesity might be a prerequisite for JNK activation, which in turn stimulates *Mcp1* expression in conjunction with loss of mTORC2. We note that mTORC2 did not control JNK (Figure 5, J and K).

In summary, we propose that obesity-mediated insulin resistance is a cause of inflammation in visceral WAT. Although our findings do not rule out the possibility that inflammation promotes insulin resistance in other tissues or conditions, they bring into question whether antiinflammation therapy in adipose tissue is an effective strategy in the prevention of type 2 diabetes.

Methods

Mice. Adipose tissue–specific *Rictor*-knockout (AdRiKO) and liver-specific *Rictor*-knockout (LiRiKO) mice were described previously (32, 35, 61). Since AdRiKO mice are infertile, we bred $Rictor^{fl/+}$ *aP2-Cre* mice with $Rictor^{fl/fl}$ mice to generate mice for our experiments. For experiments with AdRiKO mice, age-matched *Cre*-negative males were used as controls. To generate LiRiKO mice for experiments, $Rictor^{fl/fl}$ *Alb-Cre* mice were crossed with $Rictor^{fl/fl}$ mice. To generate an i-AdRiKO mouse line, $Rictor^{fl/fl}$ mice were bred with *adipoq-CreER*^{T2} mice, provided by Stefan Offermanns (Max Planck Institute for Heart and Lung Research [MPI-HLR], Bad Nauheim, Germany) (42). Once the i-AdRiKO mouse line ($Rictor^{fl/fl}$ *adipoq-CreER*^{T2}) was generated, these mice were bred with $Rictor^{fl/fl}$ mice to produce mice for experiments. For experiments with LiRiKO and i-AdRiKO mice, *Cre*-negative littermate male mice were used as controls. All mice used in this study were on a C57BL/6 background. For i-AdRiKO mice, *Rictor* knockout was induced by i.p. injection of 1 mg/mouse tamoxifen (Sigma-Aldrich) resuspended in corn oil daily for 5 days. Mice were housed at 22°C in a conventional facility under a 12-hour light/12-hour dark cycle with unlimited access to water and were fed a ND or a HFD (60% kcal from fat NAFAG 2127, KLIBA). The HFD-feeding experiment was conducted for 10 weeks unless otherwise specified. *Cre*-negative animals were used as a control. For i-AdRiKO mouse experiments, control mice were also treated with tamoxifen. Mice were randomly assigned for each experiment. Only male, 6- to 16-week-old mice were used for experiments.

Cell culture. 3T3-L1 cells were cultured and differentiated as described previously (62). In brief, 3T3-L1 preadipocyte cells were maintained in M1 medium (DMEM supplemented with 4 mM glutamine, 1 mM sodium pyruvate, 1× penicillin and streptomycin, and 10% FBS) at 37°C in an incubator with 5% CO_2. For differentiation, cells were maintained in M1 medium for 2 days after reaching confluence. The medium was replaced with M2 medium (M1 medium supplemented with 1.5 μg/ml insulin, 0.5 mM IBMX, 1 μM dexamethasone, and 2 μM rosiglitazone), defined as day 0 of differentiation. After 2 days, the medium was replaced with M3 medium (M1 with 1.5 μg/ml insulin). The medium was replaced with M2 on day 4 of differentiation. From day 6, cells were maintained in M3 with a medium change every 2 days. For all experiments, cells differentiated for 10 to 14 days were used. Torin 1 was purchased from Tocris Bioscience and dissolved in DMSO.

Human oWAT biopsies. oWAT biopsies were obtained from lean subjects with a BMI below 27 kg/m^2 and from obese subjects with a BMI above 35 kg/m^2 (Supplemental Table 2). Patients were fasted overnight and then underwent general anesthesia. All oWAT samples were obtained between 8:30 and 12:00, snap-frozen in liquid nitrogen, and stored at –80°C.

Human primary adipocytes. Human primary visceral preadipocytes (from a 56-year-oldwoman with a BMI of 23) were obtained from Lonza. Cells were cultured and differentiated according to the manufacturer's instructions. After 14 days of differentiation, cells were treated with DMSO or 250 nM torin1 for 6 hours.

Generation of Rictor-knockout cells by CRISPR/Cas9-mediated genome editing. *Rictor*-knockout 3T3-L1 cells (Hall laboratory stock) were generated using the CRISPR/Cas9 system. Oligonucleotides containing single-guide RNAs (sgRNAs) (Rictor.1, forward: CACCGGAAGATACTGATCCCGCTTG, sgRNA Rictor.1, reverse: AAACCAAGCGGGATCAGTATCTTCC; sgRNA Rictor.2, forward: CACCGTGCCTCCTAGGGCTTGGTCG, sgRNA Rictor.1, reverse: AAACCGACCAAGCCCTAGGAGGCAC) were cloned into lenti-CRISPRv2 (Addgene plasmid 52961) (48), a gift of Feng Zhang (MIT, Cambridge Massachusetts, USA). Plasmids were amplified by bacterial transformation and isolated by Miniprep (Zymo Research). Lenti-CRISPRv2 plasmids were cotransfected with psPAX2 (Addgene plasmid 12260; a gift of Didier Trono, EPFL, Lausanne, Switzerland) and pCMV-VSV-G (63) (Addgene plasmid 8454; a gift of Robert Weinberg, MIT, Cambridge, Massachusetts, USA) into HEK293T cells (Hall laboratory stock). Supernatants containing lentiviruses were collected 1 day after transfection and used to transduce undifferentiated 3T3-L1 cells. Transduced cells were selected by puromycin.

2-Deoxyglucose uptake assay. Mice were fed a ND or HFD for 4 weeks, fasted for 5 hours, and given Humalog insulin i.p. (Lilly; 0.75 U/kg body weight). After 10 minutes, 2-deoxyglucose (2DG) (Sigma-Aldrich) was given i.p. (32.8 μg/g body weight), and tissues (eWAT, muscle) were collected 20 minutes later. For in vitro 2DG uptake, differentiated adipocytes were cultured in serum-free M1 medium, washed 3 times with HKRP buffer (1.2 mM KH_2PO_4, 1.2 mM $MgSO_4$, 1.3 mM $CaCl_2$, 118 mM NaCl, 5 mM KCl, and 30 mM HEPES, pH7.5), and cultured in HKRP buffer with 1% BSA for 30 minutes. Cells were stimulated with 100 nM insulin for 20 minutes and subsequently

Table 1. qRT-PCR primers

Species	Target	Forward primer	Reverse primer
Mouse	*Cd68*	TATAGCCCAAGGAACAGAGGAA	CTGTAGGTGTCATCGTGAAGG
	F4/80	TTGCGGGATTCCTACACTATCT	AGGTTTCTCACCATCAGGAAGA
	Tnfa	GGTTCTGTCCCTTTCACTCA	TGCCTCTTCTGCCAGTTCC
	Rictor	ATGGCCAATATCGCAAAGAAG	GTGGCCAAATTGCAAGGAGTA
	Cd11c	GGATGGACTGGTGGATCTGG	GGTGTGAAGTGAACAGTTGGTG
	Mcp1	CTACCTTTTCCACAACCACCTC	ATTAAGGCATCACAGTCCGAGT
	Lep	TCACACACGCAGTCGGTATC	ACTCAGAATGGGGTGAAGCC
	Adipoq	TGACGACACCAAAAGGGCTC	ACGTCATCTTCGGCATGACT
	Cd31	TGCTCTCGAAGCCCAGTATT	ATGGGTGCAGTTCCATTTTC
	Cd45	CCAGTGATGAACTGAGCACAAC	TTGGGGGTGTGGATTCAGTG
	Cd3g	CTTCAAGGCACTGTAGCCCA	GTACAGAACCGTCTCCTCGG
	Polr2a	AATCCGCATCATGAACAGTG	CAGCATGTTGGACTCAATGC
	Tbp	TGCTGTTGGTGATTGT	CTTGTGTGGGAAAGAT
	Rpl7	CGGTCTCTTGGTAAGTTTGGC	TTGAAGCGTTTCCCGACTGT
Human	*MCP1*	CCGAGAGGCTGAGACTAACC	CTTTCATGCTGGAGGCGAGA
	CD68	ACAGGGAATGACTGTCCTCAC	TGCTCTCTGTAACCGTGGGT
	RNA18S5	GTAACCCGTTGAACCCCATT	CCATCCAATCGGTAGTAGCG

cultured with 1 mM 2DG for 20 minutes. Tissues or cells were lysed in 10 mM Tris-HCL, pH 8.0, by boiling for 15 minutes. 2-Deoxyglucose-6-phosphate (2DGP) was measured using a Glucose Uptake-Glo Assay Kit (Promega) following the manufacturer's instructions.

MCP1 ELISA and adipokine array. Mice were fed a HFD for 10 weeks, and MCP1 levels in eWAT and plasma were measured using a commercial ELISA kit (R&D Systems) following the manufacturer's instructions. Adipokine array (R&D Systems) was performed according to the manufacturer's instructions.

MCP1-neutralizing antibody treatment. Mice were fed a HFD for 8 weeks. Mice were given i.p. 1 mg/kg body weight isotype control IgG (BD Biosciences; catalog 553968, lot 4113848) or anti–MCP1 IgG (BD Biosciences; catalog 554440, lot 5203535) every 2 days for 2 weeks.

ITT. Mice were fasted for 5 hours, Humalog insulin (Lilly) was given i.p. (0.75U/kg body weight), and blood glucose levels were measured with an Accu-Chek blood glucose meter.

In vivo insulin stimulation. Mice were fasted for 5 hours, Humalog insulin (Lilly) was administered i.p. (0.75U/kg body weight), and tissues were collected.

Isolation of adipocytes and SVCs and flow cytometric analysis. SVCs were isolated and stained with antibody as previously described (64). In brief, fat pads were excised and minced in $HBSS^{++}$ supplemented with 0.5% BSA and digested with 1 mg/ml type II collagenase (Sigma-Aldrich) at 37°C for 40 minutes with vigorous shaking. After digestion, final 10 mM EDTA was added and incubated for 10 minutes to dissociate SVCs. The resulting suspension was filtered through a 100-μm cell strainer (Corning) and centrifuged at 500 *g* for 10 minutes. After centrifugation, floating adipocytes were collected, and SVC-containing pellets were subjected to red blood cell lysis in 1× Red Blood Cell Lysis Buffer (eBioscience). SVCs were blocked with Fc-block (BD Biosciences) and stained with the following antibodies and reagents: F4/80-PE (eBioscience; catalog 12-4801-80); CD11b-APC eFluor 780 (eBioscience; catalog 47-0112-80); CD11c-PE-Cy7 (eBioscience; catalog 25-0114-81); CD45.2-PerCP (eBioscience; catalog 45-0454-80); CD301–Alexa Fluor 647 (AbD Serotec; catalog MCA2392A647T); CD4-FITC (eBioscience; catalog 11-0041-81); CD8a-PE (eBioscience; catalog 12-0081-81); CD3-APC (eBioscience; catalog 17-0032-80); CD45R (B220) PerCP-Cyanine 5.5 (eBioscience; catalog 45-0452-80); CD25 APC-eFluor 780 (eBioscience; catalog 47-0251-80); and Ki-67–Alexa Fluor 488 (BD Pharmingen; catalog 561165), along with a FOXP3 Flow Kit (BioLegend, catalog 320021) and a Live/Dead Fixable Dead Cell Kit (Thermo Fisher; catalog L34955). Stained SVCs were analyzed using the FACSCanto II (BD Biosciences) or sorted with a FACSAria IIIu (BD Biosciences).

Immunohistochemistry. WATs were fixed overnight in 4% formalin at room temperature, dehydrated, embedded in paraffin, and cut into 5-μm-thick sections. Adipose tissue macrophages were stained with anti-F4/80 antibody (Abcam; catalog ab6640) and a secondary antibody conjugated with HRP (VECTOR Laboratories), followed by incubation in ImmPACT DAB peroxidase substrate solution (VECTOR Laboratories) and subsequent counterstaining with hematoxylin (VECTOR Laboratories). Images were obtained using DM600B (Leica) and analyzed with Fiji software (ImageJ; NIH) (65).

RNA isolation and quantitative real-time PCR. Total RNA was isolated with TRIzol Reagent (Sigma-Aldrich) and an RNeasy Kit (QIAGEN). For RNA isolation from sorted macrophages, an RNeasy Micro Kit (QIAGEN) was used. RNA was reverse transcribed to cDNA using an iScript cDNA Synthesis Kit (Bio-Rad). Semiquantitative real-time PCR analysis was performed using Fast SYBR Green (Applied Biosystems). Relative expression levels were determined by normalizing each Ct value to either *Polr2a*, *Tbp*, or *Rpl7* expression for mice and *RNA18S5* for human samples using the ΔΔCt method. The primer sequences used in this study are shown in Table 1.

Protein isolation and immunoblots. Tissues were homogenized in lysis buffer containing 100 mM Tris-HCl, pH7.5, 2 mM EDTA, 2 mM EGTA, 150 mM NaCl, 1% Triton X-100, cOmplete Inhibitor Cocktail (Roche), and PhosSTOP (Roche). The protein concentration was determined by the Bradford assay, and equal amounts of protein were separated by SDS-PAGE and transferred onto nitrocellulose membranes (GE Healthcare). The following antibodies were used in this study and were purchased from Cell Signaling Technology: AKT (catalog 4685); phosphorylated AKT (p-AKT) (Ser473) (catalog 4060), RICTOR (catalog 2140), PKC (catalog 2056), p-S6K (Thr389) (catalog 9234), S6K (catalog 2708), p-JNK (Thr183/Tyr185) (catalog 4668), JNK (catalog 9252), p-cJUN (Ser73) (catalog 3270), cJUN (catalog 9165). Actin monoclonal antibody was purchased from Sigma-Aldrich (catalog MAB1501).

JNK kinase assay. JNK activity was measured using a SAPK/JNK Kinase Assay Kit (Nonradioactive) (Cell Signaling Technology; catalog 8794).

Proteome analysis. eWAT was homogenized in urea lysis buffer containing 50 mM Tris-HCl, pH 8.2, 8 M urea, 75 mM NaCl, cOmplete inhibitor cocktail (Roche), and PhosSTOP (Roche). The extracts were incubated for 30 minutes at 4°C and centrifuged for 15 minutes at 14,000 *g*. Protein concentration was measured with the Bradford assay. Proteins were reduced with 2.5 mM DTT for 40 minutes at 56°C and alkylated with 7.5 mM iodoacetamide for 40 minutes at room temperature in the dark with gentle shaking. The urea concentration was lowered to 4 M with 25 mM Tris-HCl, pH 8. The lysates were digested with 2 rounds of endoproteinase LysC (Wako) at an enzyme/protein ratio of 1:100 (w/w) at 37°C for 2 hours. After the LysC digestion, the

urea concentration was lowered to 1 M with 25 mM Tris-HCl, pH 8.0. The lysates were digested with 2 rounds of trypsin (Worthington) at an enzyme/protein ratio of 1:100 (w/w) for 2 hours, followed by overnight digestion at 37°C. Digestion was stopped by adding trifluoroacetic acid (TFA) to reach a final concentration of 0.4%. The digests were centrifuged for 5 minutes at 3,000 *g* and desalted on a C18 Sep-Pak cartridge (Waters) that had been equilibrated with 0.1% TFA. The peptides were applied onto the cartridge, washed with 0.1% TFA, and subsequently eluted with 0.5% AcOH/80% AcCN. The peptide concentration was estimated by measuring the UV absorbance at 280 nm (66). The desalted peptides were dried in a SpeedVac (Thermo Fisher Scientific). For strong cation separation, the dried peptides were dissolved in 1.5 ml 7 mM KH_2PO_4, pH 2.65, and 30% AcCN (v/v) (SCX buffer A) and centrifuged at 10,600 × *g*. The peptides were applied onto a HiTrap SP cartridge (GE Healthcare) that had been equilibrated with 3 ml SCX buffer A, and the cartridge was washed with 3 ml SCX buffer A. Bound peptides were stepwise eluted with 1.5 ml each of SCX buffer A containing 50 mM, 100 mM, 150 mM, 250 mM, and 350 mM KCl, and each fraction was collected manually. The peptide concentration was estimated by absorbance at 280 nm. The fractions were dried in a SpeedVac and desalted on either micro or macro spin C18 columns (The Nest Group). The peptides were desalted with 0.1% TFA and subsequently eluted with 0.5% AcOH/80% AcCN. The dried peptides (20 μg) were dissolved in 20 μl of 0.1% formic acid and 0.005% TFA and analyzed on an Orbitrap Elite FT Hybrid Instrument (Thermo Fisher Scientific).

The peptides from the SCX step-off fractions were analyzed by capillary liquid chromatography tandem MS (LC-MS/MS) using a home-packed separating column (0.075 mm × 15 cm) packed with Reprosil C18 reverse-phase material (2.4 m particle size; provided by Albin Maisch, Ammerbuch-Entringen, Germany). The column was connected online to an Orbitrap Elite FT Hybrid Instrument. The solvents used for peptide separation were 0.1% formic acid in water/0.005% TFA (solvent A) and 0.1% formic acid/0.005% TFA and 80% acetonitrile in water (solvent B). Peptide digest (2 μl) was injected with a Proxeon nLC Capillary Pump (Thermo Fisher Scientific) set to 0.3 μl/min. A linear gradient from 0% to 40% of solvent B in solvent A in 95 minutes was delivered with the nano pump at a flow rate of 0.3 μl/min. After 95 minutes, the percentage of solvent B was increased to 75% in 10 minutes. The eluting peptides were ionized at 2.5 kV. The mass spectrometer was operated in data-dependent mode. The precursor scan was done in the Orbitrap, set to 60,000 resolution, while the fragment ions were mass analyzed in the LTQ Orbitrap Instrument. A top-10 method was run so that the 10 most intense precursors were selected for fragmentation. Each biological replicate was measured in 3 technical replicates.

The LC-MS/MS data were searched with Proteome Discoverer 1.4 (Thermo Fisher Scientific), set to Mascot and Sequest HT against a mouse UniProtKB databank (67). The precursor tolerance was set to 10 ppm, while the fragment ion tolerance was set to 0.5 Da. The following variable modifications were used during the search: carbamidomethyl-cystein, oxidized methionine, and N-terminal protein acetylation. The peptide search matches were set at "high confidence" (1% FDR).

All LC-MS/MS runs were aligned with Progenesis software (Waters). For identification of the aligned features, the corresponding Proteome Discoverer 1.4 results files were imported into the aligned Progenesis data file. The data aligned in Progenesis were exported as .txt files to the R-based Perseus program (68). Volcano plots and ANOVA 2-sample *t* tests were performed with a FDR of 5%. Proteins were considered regulated when the ANOVA 2-sample *t* test was below 0.05 in each technical replicate and the Student's *t* test *P* value was below 0.05 in at least 2 of 3 biological replicates. GO process analysis was performed according to the framework provided by the Gene Ontology Consortium (69, 70).

Statistics. Immunoblots for p-AKT2 (Ser474) and AKT2 on human oWAT were quantified in Fiji (65). Samples for which we failed to detect AKT2 were excluded from further analysis. Sample size was chosen according to our previous studies and published reports in which similar experimental procedures were described. The investigators were not blinded to the treatment groups. All data are shown as the mean ± SEM. Sample numbers are indicated in each figure legend. For mouse experiments, *n* represents the number of animals, and for cell culture experiments, *N* indicates the number of independent experiments. To determine the statistical significance between 2 groups, an unpaired 2-tailed Student's *t* test was performed. For more than 3 groups, 1-way ANOVA was performed. For ITT data, 2-way ANOVA was performed. For human samples, statistical outliers were excluded in Figure 6 according to the robust regression and outlier removal test (ROUT) (Q = 1%) but are included in Supplemental Figure 9. In all cases, a Mann-Whitney *U* test was performed to determine statistical significance. All statistical analysis was performed using GraphPad Prism 7 (GraphPad Software). Cluster analysis was performed using ClustVis (71). A *P* value of less than 0.05 was considered statistically significant.

Study approval. All animal experiments were performed in accordance with federal guidelines for animal experimentation and approved by the Kantonales Veterinäramt of the Kanton Basel-Stadt (Basel, Switzerland). For human biopsies, the study protocol was approved by the Ethikkomission Nordwest-und Zentralschweiz (EKNZ) (Basel, Switzerland). All patients provided informed consent to provide adipose tissue samples.

Author contributions

MS and MNH designed and directed the research. MS, VA, RP, ICF, DW, ACMG, NC, SM, MC, JAM, MMS, and PJ performed experiments and analyzed data. MS, RP, BW, and CB designed the protocol for the collection of human adipose tissue biopsies. MS and MNH wrote the manuscript.

Acknowledgments

We thank Didier Trono (EPFL, Switzerland), Robert Weinberg (MIT, USA), and Feng Zhang (MIT, USA), Stefan Offermanns (MPI-HLR, Germany), the Imaging Core Facility (Biozentrum), and the FACS Core Facility (Biozentrum) for reagents, a mouse strain, equipment, or technical support. We acknowledge support from the Swiss National Science Foundation (to MS and MNH), the Louis Jeantet Foundation (to MNH), and the Canton of Basel (to MNH).

Address correspondence to: Mitsugu Shimobayashi or Michael N. Hall, Klingelbergstrasse 50/70, Basel 4056, Switzerland. Phone: 41.61.207.2171; Email: mitsugu.shimobayashi@unibas.ch (MS). Phone: 41.61.207.2150; Email: m.hall@unibas.ch (MNH).

1. Rocha VZ, Libby P. Obesity, inflammation, and atherosclerosis. *Nat Rev Cardiol*. 2009;6(6):399–409.
2. Odegaard JI, Chawla A. Pleiotropic actions of insulin resistance and inflammation in metabolic homeostasis. *Science*. 2013;339(6116):172–177.
3. Park J, Morley TS, Kim M, Clegg DJ, Scherer PE. Obesity and cancer — mechanisms underlying tumour progression and recurrence. *Nat Rev Endocrinol*. 2014;10(8):455–465.
4. Lackey DE, Olefsky JM. Regulation of metabolism by the innate immune system. *Nat Rev Endocrinol*. 2016;12(1):15–28.
5. McLaughlin T, Ackerman SE, Shen L, Engleman E. Role of innate and adaptive immunity in obesity-associated metabolic disease. *J Clin Invest*. 2017;127(1):5–13.
6. Rosen ED, Spiegelman BM. What we talk about when we talk about fat. *Cell*. 2014;156(1–2):20–44.
7. Lumeng CN, Bodzin JL, Saltiel AR. Obesity induces a phenotypic switch in adipose tissue macrophage polarization. *J Clin Invest*. 2007;117(1):175–184.
8. Nguyen MT, et al. A subpopulation of macrophages infiltrates hypertrophic adipose tissue and is activated by free fatty acids via Toll-like receptors 2 and 4 and JNK-dependent pathways. *J Biol Chem*. 2007;282(48):35279–35292.
9. Weisberg SP, et al. Obesity is associated with macrophage accumulation in adipose tissue. *J Clin Invest*. 2003;112(12):1796–1808.
10. Xu H, et al. Chronic inflammation in fat plays a crucial role in the development of obesity-related insulin resistance. *J Clin Invest*. 2003;112(12):1821–1830.
11. Hotamisligil GS, Shargill NS, Spiegelman BM. Adipose expression of tumor necrosis factor-α: direct role in obesity-linked insulin resistance. *Science*. 1993;259(5091):87–91.
12. Kanda H, et al. MCP-1 contributes to macrophage infiltration into adipose tissue, insulin resistance, and hepatic steatosis in obesity. *J Clin Invest*. 2006;116(6):1494–1505.
13. Patsouris D, Li PP, Thapar D, Chapman J, Olefsky JM, Neels JG. Ablation of CD11c-positive cells normalizes insulin sensitivity in obese insulin resistant animals. *Cell Metab*. 2008;8(4):301–309.
14. Lee YS, et al. Inflammation is necessary for long-term but not short-term high-fat diet-induced insulin resistance. *Diabetes*. 2011;60(10):2474–2483.
15. Tian XY, et al. Thermoneutral housing accelerates metabolic inflammation to potentiate atherosclerosis but not insulin resistance. *Cell Metab*. 2016;23(1):165–178.
16. Wernstedt Asterholm I, et al. Adipocyte inflammation is essential for healthy adipose tissue expansion and remodeling. *Cell Metab*. 2014;20(1):103–118.
17. Kern PA, Saghizadeh M, Ong JM, Bosch RJ, Deem R, Simsolo RB. The expression of tumor necrosis factor in human adipose tissue. Regulation by obesity, weight loss, and relationship to lipoprotein lipase. *J Clin Invest*. 1995;95(5):2111–2119.
18. Ofei F, Hurel S, Newkirk J, Sopwith M, Taylor R. Effects of an engineered human anti-TNF-α antibody (CDP571) on insulin sensitivity and glycemic control in patients with NIDDM. *Diabetes*. 1996;45(7):881–885.
19. Paquot N, Castillo MJ, Lefebvre PJ, Scheen AJ. No increased insulin sensitivity after a single intravenous administration of a recombinant human tumor necrosis factor receptor: Fc fusion protein in obese insulin-resistant patients. *J Clin Endocrinol Metab*. 2000;85(3):1316–1319.
20. Stanley TL, et al. TNF-α antagonism with etanercept decreases glucose and increases the proportion of high molecular weight adiponectin in obese subjects with features of the metabolic syndrome. *J Clin Endocrinol Metab*. 2011;96(1):E146–E150.
21. Wascher TC, Lindeman JH, Sourij H, Kooistra T, Pacini G, Roden M. Chronic TNF-alpha neutralization does not improve insulin resistance or endothelial function in "healthy" men with metabolic syndrome. *Mol Med*. 2011;17(3-4):189–193.
22. Nagareddy PR, et al. Adipose tissue macrophages promote myelopoiesis and monocytosis in obesity. *Cell Metab*. 2014;19(5):821–835.
23. Amano SU, et al. Local proliferation of macrophages contributes to obesity-associated adipose tissue inflammation. *Cell Metab*. 2014;19(1):162–171.
24. Kamei N, et al. Overexpression of monocyte chemoattractant protein-1 in adipose tissues causes macrophage recruitment and insulin resistance. *J Biol Chem*. 2006;281(36):26602–26614.
25. Albert V, Hall MN. mTOR signaling in cellular and organismal energetics. *Curr Opin Cell Biol*. 2015;33:55–66.
26. Loewith R, et al. Two TOR complexes, only one of which is rapamycin sensitive, have distinct roles in cell growth control. *Mol Cell*. 2002;10(3):457–468.
27. Jacinto E, et al. Mammalian TOR complex 2 controls the actin cytoskeleton and is rapamycin insensitive. *Nat Cell Biol*. 2004;6(11):1122–1128.
28. Sarbassov DD, et al. Rictor, a novel binding partner of mTOR, defines a rapamycin-insensitive and raptor-independent pathway that regulates the cytoskeleton. *Curr Biol*. 2004;14(14):1296–1302.
29. Frias MA, et al. mSin1 is necessary for Akt/PKB phosphorylation, and its isoforms define three distinct mTORC2s. *Curr Biol*. 2006;16(18):1865–1870.
30. Jacinto E, et al. SIN1/MIP1 maintains rictor-mTOR complex integrity and regulates Akt phosphorylation and substrate specificity. *Cell*. 2006;127(1):125–137.
31. Yang Q, Inoki K, Ikenoue T, Guan KL. Identification of Sin1 as an essential TORC2 component required for complex formation and kinase activity. *Genes Dev*. 2006;20(20):2820–2832.
32. Cybulski N, Polak P, Auwerx J, Ruegg MA, Hall MN. mTOR complex 2 in adipose tissue negatively controls whole-body growth. *Proc Natl Acad Sci U S A*. 2009;106(24):9902–9907.
33. Kumar A, et al. Fat cell-specific ablation of rictor in mice impairs insulin-regulated fat cell and whole-body glucose and lipid metabolism. *Diabetes*. 2010;59(6):1397–1406.
34. Tang Y, et al. Adipose tissue mTORC2 regulates ChREBP-driven de novo lipogenesis and hepatic glucose metabolism. *Nat Commun*. 2016;7:11365.
35. Hagiwara A, et al. Hepatic mTORC2 activates glycolysis and lipogenesis through Akt, glucokinase, and SREBP1c. *Cell Metab*. 2012;15(5):725–738.
36. Lamming DW, et al. Rapamycin-induced insulin resistance is mediated by mTORC2 loss and uncoupled from longevity. *Science*. 2012;335(6076):1638–1643.
37. Yuan M, Pino E, Wu L, Kacergis M, Soukas AA. Identification of Akt-independent regulation of hepatic lipogenesis by mammalian target of rapamycin (mTOR) complex 2. *J Biol Chem*. 2012;287(35):29579–29588.
38. Bentzinger CF, et al. Skeletal muscle-specific ablation of raptor, but not of rictor, causes metabolic changes and results in muscle dystrophy. *Cell Metab*. 2008;8(5):411–424.
39. Kumar A, et al. Muscle-specific deletion of rictor impairs insulin-stimulated glucose transport and enhances Basal glycogen synthase activity. *Mol Cell Biol*. 2008;28(1):61–70.
40. Lee KY, et al. Lessons on conditional gene targeting in mouse adipose tissue. *Diabetes*. 2013;62(3):864–874.
41. Makowski L, et al. Lack of macrophage fatty-acid-binding protein aP2 protects mice deficient in apolipoprotein E against atherosclerosis. *Nat Med*. 2001;7(6):699–705.
42. Sassmann A, Offermanns S, Wettschureck N. Tamoxifen-inducible Cre-mediated recombination in adipocytes. *Genesis*. 2010;48(10):618–625.
43. Festuccia WT, Pouliot P, Bakan I, Sabatini DM, Laplante M. Myeloid-specific Rictor deletion induces M1 macrophage polarization and potentiates in vivo pro-inflammatory response to lipopolysaccharide. *PLoS One*. 2014;9(4):e95432.
44. Park SY, et al. Unraveling the temporal pattern of diet-induced insulin resistance in individual organs and cardiac dysfunction in C57BL/6 mice. *Diabetes*. 2005;54(12):3530–3540.
45. Turner N, et al. Distinct patterns of tissue-specific lipid accumulation during the induction of insulin resistance in mice by high-fat feeding. *Diabetologia*. 2013;56(7):1638–1648.
46. Kawano Y, et al. Colonic Pro-inflammatory macrophages cause insulin resistance in an intestinal Ccl2/Ccr2-dependent manner. *Cell Metab*. 2016;24(2):295–310.
47. Thoreen CC, et al. An ATP-competitive mammalian target of rapamycin inhibitor reveals rapamycin-resistant functions of mTORC1. *J Biol Chem*. 2009;284(12):8023–8032.
48. Sanjana NE, Shalem O, Zhang F. Improved vectors and genome-wide libraries for CRISPR screening. *Nat Methods*. 2014;11(8):783–784.
49. Takahashi K, et al. JNK- and IκB-dependent pathways regulate MCP-1 but not adiponectin release from artificially hypertrophied 3T3-L1 adipocytes preloaded with palmitate in vitro. *Am J Physiol Endocrinol Metab*. 2008;294(5):E898–909.
50. Christiansen T, Richelsen B, Bruun JM. Monocyte chemoattractant protein-1 is produced in isolated adipocytes, associated with adiposity and reduced after weight loss in morbid obese subjects. *Int J Obes (Lond)*. 2005;29(1):146–150.
51. Morley TS, Xia JY, Scherer PE. Selective enhancement of insulin sensitivity in the mature adipocyte is sufficient for systemic metabolic improvements. *Nat Commun*. 2015;6:7906.
52. McCurdy CE, et al. Attenuated Pik3r1 expression prevents insulin resistance and adipose tissue macrophage accumulation in diet-induced obese mice. *Diabetes*. 2012;61(10):2495–2505.
53. Shearin AL, Monks BR, Seale P, Birnbaum MJ. Lack of AKT in adipocytes causes severe lipodys-

trophy. *Mol Metab*. 2016;5(7):472–479.
54. Huang SC, et al. Metabolic reprogramming mediated by the mTORC2-IRF4 signaling axis is essential for macrophage alternative activation. *Immunity*. 2016;45(4):817–830.
55. O'Neill LA, Pearce EJ. Immunometabolism governs dendritic cell and macrophage function. *J Exp Med*. 2016;213(1):15–23.
56. Tan SX, et al. Selective insulin resistance in adipocytes. *J Biol Chem*. 2015;290(18):11337–11348.
57. Takahashi N, et al. Suppression of lipin-1 expression increases monocyte chemoattractant protein-1 expression in 3T3-L1 adipocytes. *Biochem Biophys Res Commun*. 2011;415(1):200–205.
58. Kim HB, et al. Lipin 1 represses NFATc4 transcriptional activity in adipocytes to inhibit secretion of inflammatory factors. *Mol Cell Biol*. 2010;30(12):3126–3139.
59. Hirosumi J, et al. A central role for JNK in obesity and insulin resistance. *Nature*. 2002;420(6913):333–336.
60. Sabio G, et al. A stress signaling pathway in adipose tissue regulates hepatic insulin resistance. *Science*. 2008;322(5907):1539–1543.
61. Albert V, et al. mTORC2 sustains thermogenesis via Akt-induced glucose uptake and glycolysis in brown adipose tissue. *EMBO Mol Med*. 2016;8(3):232–246.
62. Zebisch K, Voigt V, Wabitsch M, Brandsch M. Protocol for effective differentiation of 3T3-L1 cells to adipocytes. *Anal Biochem*. 2012;425(1):88–90.
63. Stewart SA, et al. Lentivirus-delivered stable gene silencing by RNAi in primary cells. *RNA*. 2003;9(4):493–501.
64. Cho KW, Morris DL, Lumeng CN. Flow cytometry analyses of adipose tissue macrophages. *Methods Enzymol*. 2014;537:297–314.
65. Schindelin J, et al. Fiji: an open-source platform for biological-image analysis. *Nat Methods*. 2012;9(7):676–682.
66. Wisniewski JR, Zougman A, Nagaraj N, Mann M. Universal sample preparation method for proteome analysis. *Nat Methods*. 2009;6(5):359–362.
67. The UniProt Consortium. UniProt: the universal protein knowledgebase. *Nucleic Acids Res*. 2017;45(D1):D158–D169.
68. Tyanova S, et al. The Perseus computational platform for comprehensive analysis of (prote)omics data. *Nat Methods*. 2016;13(9):731–740.
69. Ashburner M, et al. Gene ontology: tool for the unification of biology. The Gene Ontology Consortium. *Nat Genet*. 2000;25(1):25–29.
70. Gene Ontology C. Gene Ontology Consortium: going forward. *Nucleic Acids Res*. 2015;43(database issue):D1049–D1056.
71. Metsalu T, Vilo J. ClustVis: a web tool for visualizing clustering of multivariate data using Principal Component Analysis and heatmap. *Nucleic Acids Res*. 2015;43(W1):W566–W570.